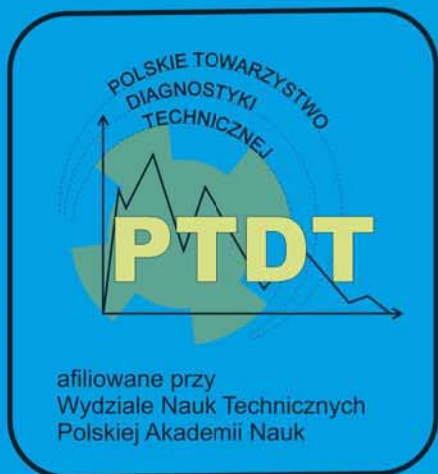


DIAGNOZA - GENEZA - PROGNOZA => PODSTAWA KAŻDEJ DECYZJI

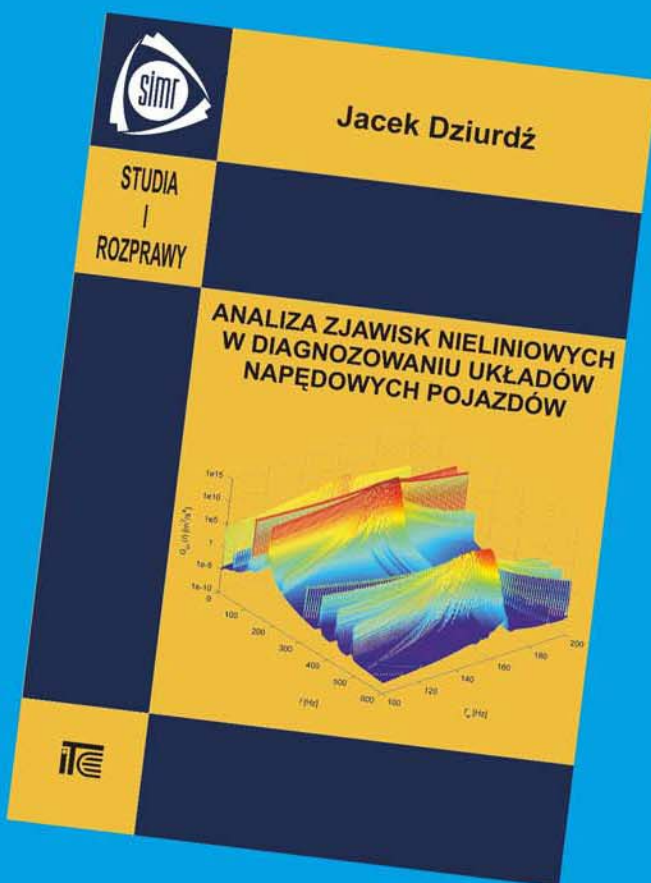


afiliowane przy
Wydziale Nauk Technicznych
Polskiej Akademii Nauk

Diagnostyka

Applied Structural Health,
Usage and Condition Monitoring

ISSN 1641-6414



Vol. 14, No. 4

PTDT, Warszawa, 2013

RADA PROGRAMOWA / PROGRAM COUNCIL

PRZEWODNICZĄCY / CHAIRMAN:

prof. dr hab. dr h.c. mult. **Czesław CEMPEL** Politechnika Poznańska

REDAKTOR NACZELNY / CHIEF EDITOR:

prof. dr hab. inż. **Wiesław STASZEWSKI** AGH w Krakowie

CZŁONKOWIE / MEMBERS:

prof. dr hab. inż. **Jan ADAMCZYK**
AGH w Krakowie

prof. **Francesco AYMERICH**
University of Cagliari – Italy

prof. **Jérôme ANTONI**
University of Technology of Compiègne – France

prof. dr. **Ioannis ANTONIADIS**
National Technical University Of Athens – Greece

dr inż. **Roman BARCZEWSKI**
Politechnika Poznańska

prof. dr hab. inż. **Walter BARTELMUS**
Politechnika Wrocławska

prof. dr hab. inż. **Wojciech BATKO**
AGH w Krakowie

prof. dr hab. inż. **Adam CHARHALIS**
Akademia Morska w Gdyni

prof. **Li CHENG**
The Hong Kong Polytechnic University – China

prof. dr hab. inż. **Wojciech CHOLEWA**
Politechnika Śląska

prof. dr hab. inż. **Zbigniew DĄBROWSKI**
Politechnika Warszawska

prof. **Charles FARRAR**
Los Alamos National Laboratory – USA

prof. **Wiktor FRID**
Royal Institute of Technology in Stockholm – Sweden

dr inż. **Tomasz GAŁKA**
Instytut Energetyki w Warszawie

prof. **Len GELMAN**
Cranfield University – England

prof. **Mohamed HADDAR**
National School of Engineers of Sfax – Tunisia

prof. dr hab. inż. **Jan KICIŃSKI**
IMP w Gdańsku

prof. dr hab. inż. **Daniel KUJAWSKI**
Western Michigan University – USA

prof. **Graeme MANSON**
University of Sheffield – UK

prof. dr hab. **Wojciech MOCZULSKI**
Politechnika Śląska

prof. dr hab. inż. **Stanisław RADKOWSKI**
Politechnika Warszawska

prof. **Bob RANDALL**
University of South Wales – Australia

prof. dr **Raj B. K. N. RAO**
President COMADEM International – England

prof. **Riccardo RUBINI**
University of Modena and Reggio Emilia – Italy

prof. **Massimo RUZZENE**
Georgia Institute of Technology – USA

prof. **Vasily S. SHEVCHENKO**
BSSR Academy of Sciences Mińsk – Belarus

prof. **Menad SIDAHMED**
University of Technology Compiègne – France

Prof. **Tadeusz STEPINSKI**
Uppsala University - Sweden

prof. **Wiesław TRĄMPCZYŃSKI**
Politechnika Świętokrzyska

prof. dr hab. inż. **Tadeusz UHL**
AGH w Krakowie

prof. **Vitalijus VOLKOVAS**
Kaunas University of Technology – Lithuania

prof. **Keith WORDEN**
University of Sheffield – UK

prof. dr hab. inż. **Andrzej WILK**
Politechnika Śląska

dr **Gajraj Singh YADAVA**
Indian Institute of Technology – India

prof. dr hab. inż. **Radosław ZIMOROZ**
Politechnika Wrocławska

prof. dr hab. inż. **Bogdan ŻÓŁTOWSKI**
UTP w Bydgoszczy

WYDAWCA:

Polskie Towarzystwo Diagnostyki Technicznej
ul. Narbutta 84
02-524 Warszawa

REDAKTOR NACZELNY:

prof. dr hab. inż. **Wiesław STASZEWSKI**

SEKRETARZ REDAKCJI:

dr inż. **Slawomir WIERZBICKI**

CZŁONKOWIE KOMITETU REDAKCYJNEGO:

dr inż. **Krzysztof LIGIER**
dr inż. **Paweł MIKOŁAJCZAK**

ADRES REDAKCJI:

Redakcja Diagnostyki
Katedra Budowy, Eksplotacji Pojazdów i Maszyn
UWM w Olsztynie
ul. Oczapowskiego 11, 10-736 Olsztyn, Poland
tel.: 89-523-48-11, fax: 89-523-34-63
www.diagnostyka.net.pl
e-mail: redakcja@diagnostyka.net.pl

KONTO PTDT:

Bank PEKAO SA O/Warszawa
nr konta: 33 1240 5963 1111 0000 4796 8376

NAKŁAD: 500 egzemplarzy

Spis treści / Contents

Dumitru-Cristinel NADABAICĂ, Valentin NEDEFF, Stanisław RADKOWSKI, Jędrzej MĄCZAK	3
The importance of FFT and BCS spectrums analysis for diagnosis and prediction of rolling bearing failure	
Marcello BONFÈ, Paolo CASTALDI, Nicola PREDA, Silvio SIMANI	13
Friction compensation in nonlinear dynamical systems using fault-tolerant control methods	
Tomasz BARSZCZ, Andrzej BIELECKI, Mateusz WÓJCIK, Marzena BIELECKA	21
ART-2 artificial neural networks applications for classification of vibration signals and operational states of wind turbines for intelligent monitoring	
Michele COTOGNO, Marco COCCONCELLI, Riccardo RUBINI.....	27
Effectiveness of the spatial acceleration modulus for rolling elements bearing fault detection	
Francesco CASTELLANI, Alberto GARINEI, Ludovico TERZI, Davide ASTOLFI, Michele MORETTI, Andrea LOMBARDI.....	35
A new data mining approach for power performance verification of an on-shore wind farm	
Przemysław SZULIM, Jędrzej MĄCZAK, Krzysztof ROKICKI, Kamil LUBIKOWSKI.....	43
Application of low-cost magnetic field and acceleration sensors in diagnostics of large-size structures <i>Zastosowanie niskobudżetowych czujników pola magnetycznego i przyspieszeń w diagnostyce konstrukcji wielkogabarytowych</i>	
Piotr BZURA	51
Topological model of aptitude of the measurement circuits of main subassemblies of an internal combustion engine crankshaft-piston assembly <i>Model topologiczny zdatności torów pomiarowych głównych podzespołów układów korbowo-tłokowych silników spalinowych</i>	
Ryszard ARENDT, Ryszard MICHALSKI	55
Structure and algorithms of a diagnostic device in a wheeled tractor <i>Struktura i algorytmy urządzenia diagnostycznego ciągników kołowych</i>	
Ryszard MICHALSKI, Ryszard ARENDT	61
Selection of diagnostic functions in a wheeled tractor <i>Dobór funkcji urządzenia diagnostycznego ciągnika kołowego</i>	
Janusz ZACHWIEJA	69
The impact of rotational speed synchronisation of exciters on the dynamics of a vibrating screen sieve <i>Wpływ synchronizacji prędkości obrotowej wzbudników na dynamikę ситa przesiewacza wibracyjnego</i>	
Henryk KAŽMIERCZAK, Tadeusz PAWŁOWSKI, Łukasz WOJNIAŁOWICZ	77
Quantifiable measures of the structural degradation of construction materials <i>Mierzalne miary procesu degradacji strukturalnej materiałów konstrukcyjnych</i>	
Lista recenzentów artykułów opublikowanych w czasopiśmie Diagnostyka w 2013 roku.....	84

THE IMPORTANCE OF FFT AND BCS SPECTRUMS ANALYSIS FOR DIAGNOSIS AND PREDICTION OF ROLLING BEARING FAILURE

Dumitru-Cristinel NADABAICĂ¹, Valentin NEDEFF¹, Stanisław RADKOWSKI², Jędrzej MĄCZAK²

¹“Vasile Alecsandri” University of Bacău, Department of Environmental Engineering and Mechanical Engineering, Calea Marasesti 156, Bacău, 600115, Romania
 e-mail: nadabaica.dumitru@ub.ro

²Warsaw University of Technology, Institute of Vehicles, Narbutta 84, 02-524 Warsaw, Poland
 e-mail: ras@simr.pw.edu.pl; jma@mechatronika.net.pl

Abstract

Dynamic equipments, in their vast majority, have rolling bearings in their components. Measurement and analysis of the values of rolling bearings vibration, on time, represent a safe and effective measure for identifying the state of wear of bearings, and to predict the evolution of their technical condition and of the entire equipment. This paper presents the detection of causes which lead to the damage of rolling bearing by using FFT (Fast Fourier Transformation) and BCS (Bearing Condition Signature) spectrums, by measuring its housing vibrations (self-aligning ball bearing, ZKL 1205K type) mounted in a test rig. The results presents the analysis mode of FFT and BCS spectrums in order to obtain beneficial information for the detection of that unbalance caused by loading, of the implemented defect on rolling bearing raceway and of bearing damage mode under the action of these causes.

Keywords: FFT spectrum, BCS spectrum, rolling bearings, diagnose, prediction.

1. INTRODUCTION

Rolling bearings are the most common and critical components of dynamic equipment. Many predictive maintenance programs use modern methods for monitoring of rolling bearing during the exploring operation, in order to detect failures and diagnosis of rolling bearing, but also to avoid the disuse of it and of equipment. The most common causes that lead to vibrations in rolling bearings are: improper design, incorrect mounting, misalignment, unbalance, improper choice of rolling bearing type, long duration of use, improper lubrication, use of equipments to other parameters than those for which they were designed and others [1, 6]. Therefore it is important that the rolling bearings to be measured and analyzed and, when necessary, any defects identified by vibration analysis to be corrected in a predictive maintenance program [2].

The diagnosis by using the envelope technique is the processing of vibration signal in order to identify defects of rolling bearings and to extract characteristic defect frequencies. By using this analysis it is possible both to identify the defects within rolling bearings and their location (outer raceway, inner raceway, rolling elements, cage) [3, 4, 6].

When the rolling bearings are damaged the characteristic defect frequencies can be observed in vibration spectrums. The occurrence of these frequencies in vibration spectrums depend the faulty component of rolling bearing [5, 7, 8]. Defects in rolling bearings can be identified by vibration analysis, if the spectral components with

typical defect frequencies (and their harmonics) are detected.

The FFT spectrums are obtained by using envelope technique of the modulating signal. These spectrums give information on the various causes that lead to the deterioration of rolling bearings (unbalance, misalignment, mechanical looseness and others). The BCS spectrums are obtained by using the amplitude demodulation technique from the amplitude modulated signal. These spectrums give us information on the condition of rolling bearing [9]. The characteristic defect frequencies of rolling bearings can be analyzed both in the FFT and BCS spectrums.

There are five defect characteristic frequencies of rolling bearings which can occur in the FFT and BCS spectrums [8]: cage ball-pass frequency (F_c); outer-raceway ball-pass frequency (F_{BPI}); inner-raceway ball-pass frequency (F_{BPO}); rolling-element rotational frequency (F_{RE}); rolling-element ball-pass frequency ($F_{BPRE} = 2x F_{RE}$). These frequencies can be calculated as:

$$F_c = \frac{1}{2} F_s \left(1 - \frac{D_b \cos \theta}{D}\right) \quad (1)$$

$$F_{BPI} = \frac{N_b}{2} F_s \left(1 + \frac{D_b \cos \theta}{D}\right) \quad (2)$$

$$F_{BPO} = \frac{N_b}{2} F_s \left(1 - \frac{D_b \cos \theta}{D}\right) \quad (3)$$

$$F_{RE} = \frac{D}{2 D_b} F_s \left(1 - \frac{D_b^2 \cos^2 \theta}{D^2}\right) \quad (4)$$

where: F_s is the fundamental frequency (rotating speed) of the shaft; D_b – the diameter ball; θ – the

contact angle; D – the pitch diameter of the rolling bearing; N_b – the number of balls.

2. EXPERIMENTAL RESEARCH

2.1. Test rig description

This experimental research has proposed the analysis of FFT and BCS spectrums in order to diagnose and predict failure of rolling bearings. Thus, the test rig consisted of a base on which the electric motor-gearbox-coupling-shaft assembly was mounted, as can be seen in Fig. 1. The electric motor has a power of 0.25 kW and a rotating speed of 2760 rpm. Since the gearbox ratio is 2.8 the shaft speed used is 1000 rpm. The shaft is supported by two rolling bearings, ZKL 1205K type. These are self-aligning ball bearing with tapered bore (taper 1:12) which are mounted on the shaft by means of adapter sleeves. The measurements were performed in the horizontal, vertical and axial directions of the rolling bearing housing from left side of the test rig.

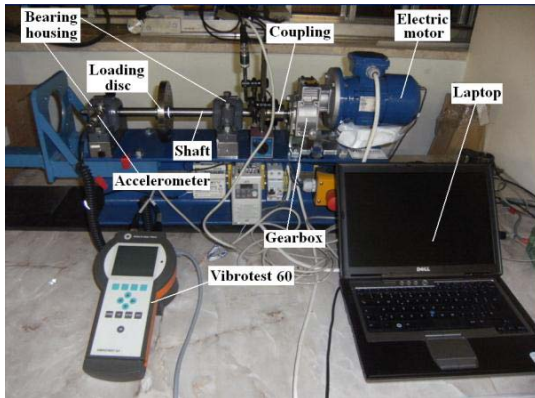


Fig. 1. Test rig

2.2. Vibration measuring devices

The acquisition of vibration measurements was performed by using a piezoelectric accelerometer (Fig. 2a) connected to the VIBROTEST 60 device (Fig. 2b) from Brüel & Kjaer Vibro. Measurements were recorded in the PC-card of VIBROTEST 60 device (Fig. 2c), then transferred for their analysis in the XMS software (extended monitoring software). The frequency range of the sensor is between 4 Hz and 10 kHz, and the resonance frequency is 35 kHz.

For the vibrations' analysis, an artificial defect was implemented on the outer raceway of the rolling bearing (Fig. 3), with its size given in Table 1. The rolling bearing worked under three loadings: 14 N, 24 N and 42 N (three steel discs of 1.4 kg each). The rolling bearing worked for 10 hours under each loading. The first measurement was acquired at the beginning of the experiment then another 5 measurements at intervals of two hours. Before each operation, between the second and

third loading, the bearing was cleaned by using petrol and then it was re-lubricated. The vibration signals were collected in the frequency domain in order to analyze: overall vibration trend, overall BCU (Bearing Condition Unit) trend, FFT and BCS spectrum. The appearance and evolution mode of the characteristic defect frequencies' amplitude, their harmonics and the side bands of these frequencies and harmonics were analyzed in FFT and BCS spectrums.

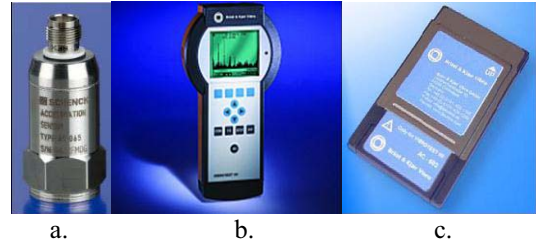


Fig. 2. Acquisition system of vibration from Brüel & Kjaer Vibro: a. – accelerometer, AS-065 type; b. – VIBROTEST 60 device; c. – PC-card

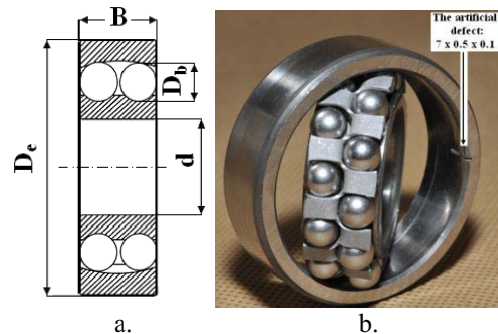


Fig. 3. Self-aligning ball bearing with tapered bore, ZKL 1205K type: a. - technical drawing; b. - photo with location of the artificial defect on rolling bearing outer raceway

The geometrical characteristics of this type of bearing are shown in Table 2.

Table 1. Sizes of the artificial defect on rolling bearing outer raceway

Defect cod	Length [mm]	Width [mm]	Depth [mm]
D1E	7	0.5	0.1

Table 2. Sizes of self-aligning ball bearing with tapered bore, ZKL 1205K type

Sizes	Values
D_e - outer diameter	52 mm
d - inner diameter	25 mm
B - thickness	15 mm
D_b - ball diameter	7.2 mm
N_b - number of balls	24 balls

The FFT spectrum was divided into a number of six bands, each band is specific of some causes leading to dynamic equipment failure. Thus, Band No. 2 is specific for the unbalances of the equipment, Band No. 3 for the misalignments, Band No. 4 for the clearances and looseness, Band No. 5 for the possible defects of rolling bearings, and Band No. 6 confirms the advanced condition of defects in rolling bearings by detecting the so-called "haystacks" [10].

The limits' calculation of these bands is done as follows:

1. Band No. 1: $0 \div 0.8 \times F_s$;
2. Band No. 2: $0.8 \times F_s \div 1.2 \times F_s$;
3. Band No. 3: $1.2 \times F_s \div 2.5 \times F_s$;
4. Band No. 4: $2.5 \times F_s \div 5.5 \times F_s$;
5. Band No. 5: $5.5 \times F_s \div 0.5 \times F_{max}$;
6. Band No. 6: $0.5 \times F_{max} \div F_{max}$.

where: F_{max} is the maximum frequency that is chosen depending on the type of equipment, the rotating speed and the type of used bearing. For this experiment will be $F_{max} = 1000$ Hz.

Thus, the limits' values of these bands calculated in this experiment will be:

1. Band No. 1: $0 \div 13.33$ Hz;
2. Band No. 2: $13.33 \div 19.99$ Hz;
3. Band No. 3: $19.99 \div 41.65$ Hz;
4. Band No. 4: $41.65 \div 91.63$ Hz;
5. Band No. 5: $91.63 \div 500$ Hz;
6. Band No. 6: $500 \div 1000$ Hz.

Based on expressions (1) \div (4) from first Section, the characteristic defect frequencies of this type of bearing have the following values: $F_c = 6.81$ Hz, $F_{BPO} = 81.45$ Hz, $F_{BPI} = 118.55$ Hz, $F_{RE} = 43.39$ Hz, $F_{BPRE} = 86.78$ Hz. Knowing that the rotating speed is 1000 rpm, the fundamental frequency will be: $F_s = 16.67$ Hz.

3. EXPERIMENTAL RESULTS AND INTERPRETATIONS

3.1. FFT and BCS spectrums analysis of the rolling bearing which worked with an artificial defect on the outer raceway under loading of 14 N

In FFT spectrum analysis for all measuring directions (Fig. 3) the harmonics of F_{BPO} frequency were detected. Also, the fundamental frequency (F_s) predominating in Band No. 2 and its harmonics

in Bands No. 3 and 4 were observed. These observations give information regarding the existence of an unbalance which is developed by loading of 14 N. Because on the horizontal FFT spectrum the F_s and its harmonics are predominant, the harmonics amplitudes of F_{BPO} ($4 \times F_{BPO} \div 9 \times F_{BPO}$) are much lower compared to them, which makes it difficult to interpret the existence of a defect on the outer raceway. Better clarity of harmonics' amplitudes of F_{BPO} can be obtained only by using the *Zoom* function of XMS software. During the experiment (Fig. 4a and 4b) in this direction the harmonics' amplitudes of F_{BPO} haven't had significant increases.

In vertical direction the $3 \times F_s$ harmonic that predominates in the first measurement (Fig. 4c) and the F_s that predominates in the 6th measurement (Fig. 4d) were observed. Also, in FFT spectrums the harmonics of F_{BPO} ($3 \times F_{BPO} \div 9 \times F_{BPO}$) were observed, that are much clearer than those in the horizontal direction and also the appearance of the harmonic $3 \times F_{BPO}$. During the experiment in this direction the harmonics' amplitudes of F_{BPO} haven't had significant increases.

In axial direction the $3 \times F_s$ harmonic that predominates in spectrums (Fig. 4e and 4f) were observed as well as the harmonics' amplitudes of F_{BPO} ($3 \times F_{BPO} \div 12 \times F_{BPO}$) that are much clearer. During the experiment in this direction the harmonics' amplitudes of F_{BPO} haven't had significant increases.

In BCS spectrums analysis for all measuring directions, the F_{BPO} frequency and its harmonics, with much clearer amplitudes than the FFT spectrums, were detected. Also, the $1 \times F_s$ (-1 and 1) and $2 \times F_s$ (-2 and 2) sidebands, which confirm the existence an unbalance developed by loading of 14 N, were detected. In horizontal and vertical directions during the experiment the amplitudes of F_{BPO} and its harmonics were more obvious than those in the axial direction (in horizontal and vertical directions the highest values occurring in the 4th measurement and in axial direction in the 6th measurement) as can be observed in Fig. 5.

Although the amplitudes of F_{BPO} and its harmonics increased during the experiment in all directions of the measurement, when the rolling bearing was dismounted (Fig. 6) it didn't have any damage caused by the implementation of the defect on the outer raceway.

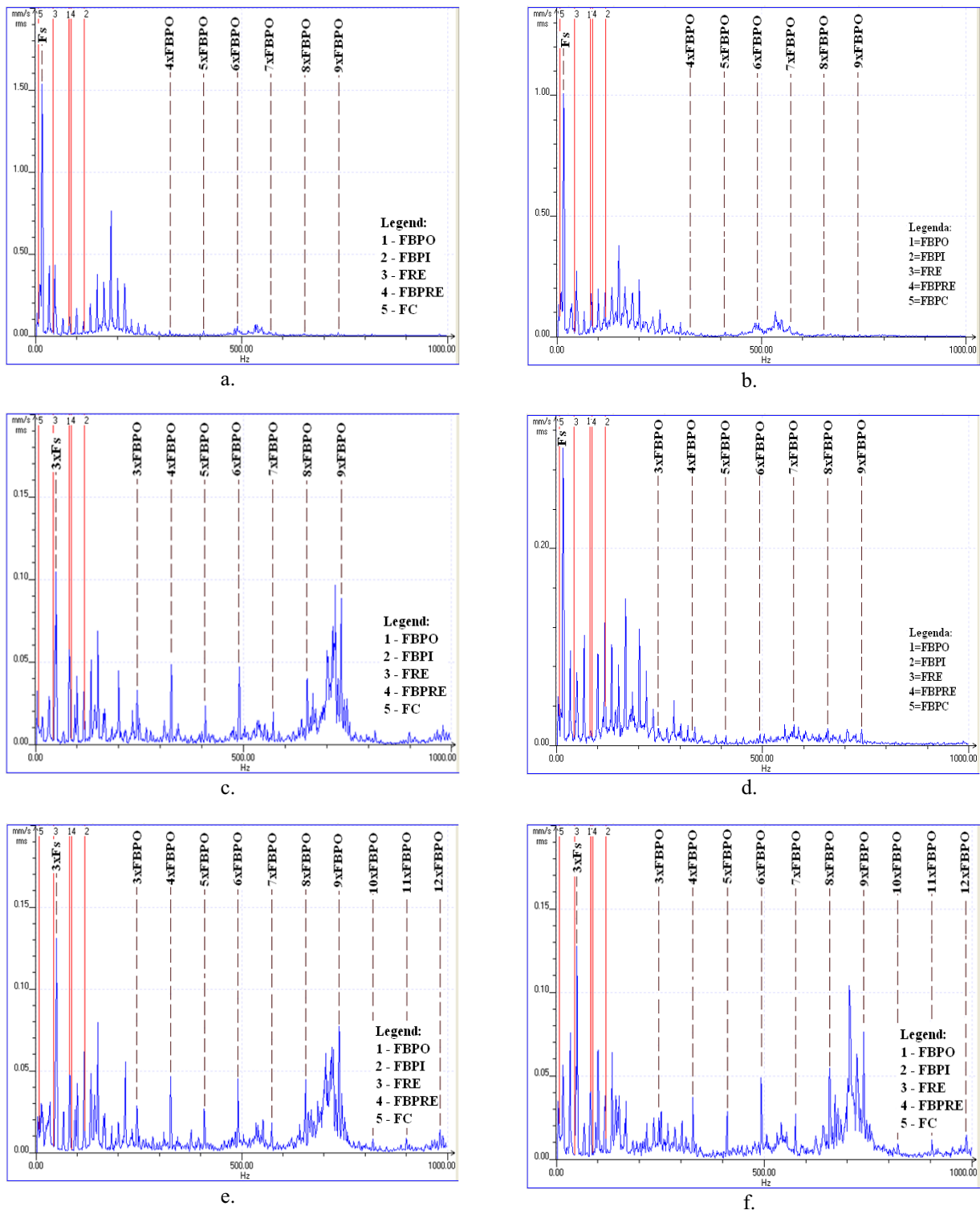


Fig. 4. FFT spectrums of bearing operating under loading of 14 N: a. - in horizontal direction for the 1st measurement; b. - in horizontal direction for the 6th measurement; c. - in vertical direction for the 1st measurement; d. – in vertical direction for the 6th measurement; e. -in axial direction for the 1st measurement; f. - in axial direction for the 6th measurement

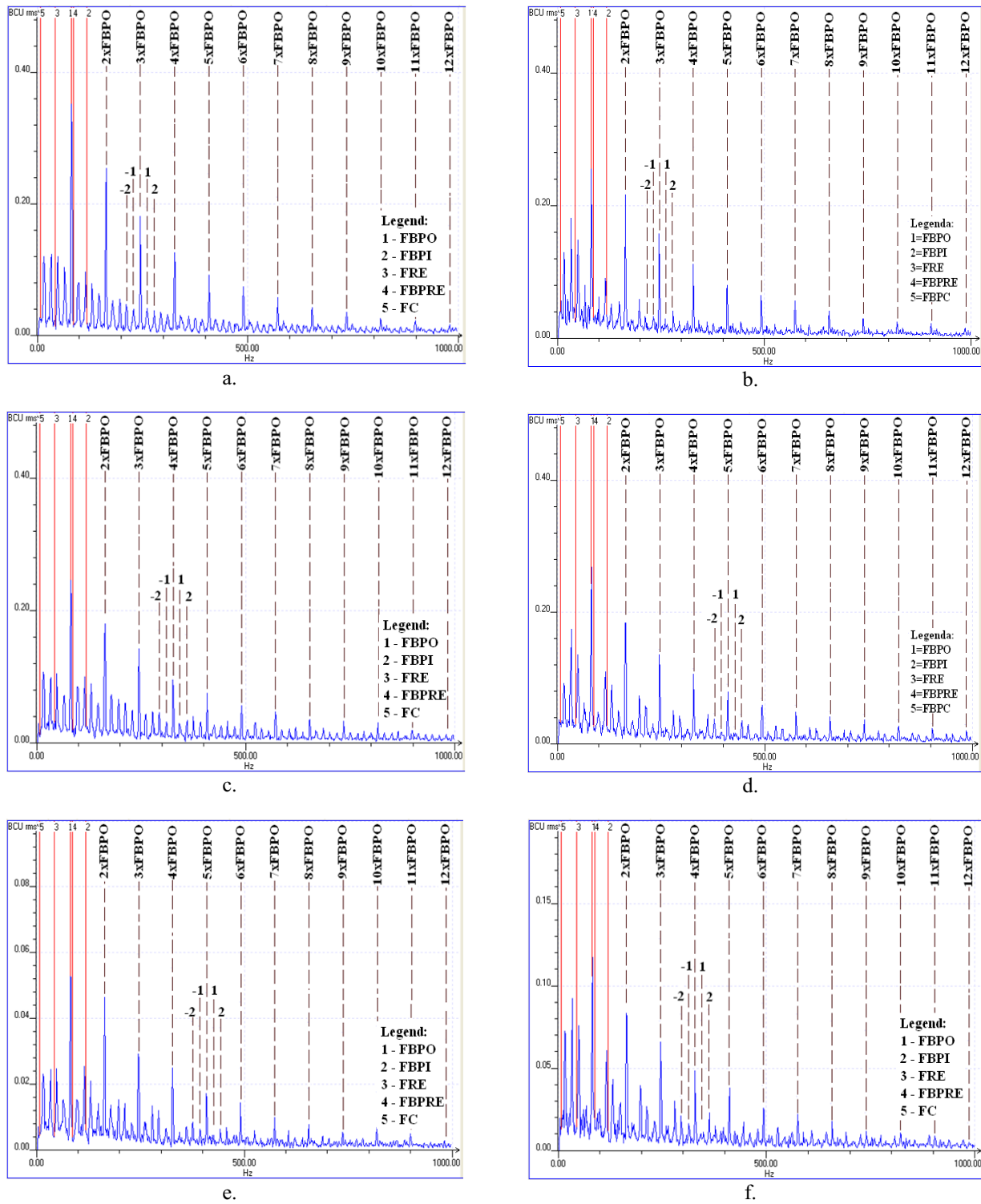


Fig. 5. BCS spectra of bearing operating under loading of 14 N: a. - in horizontal direction for the 1st measurement; b. - in horizontal direction for the 6th measurement; c. - in vertical direction for the 1st measurement; d. - in vertical direction for the 6th measurement; e. - in axial direction for the 1st measurement; f. - in axial direction for the 6th measurement



Fig.6. Evolution of rolling bearing degradation with artificial defect on the outer raceway after its operation under loading of 14 N

3.2. FFT and BCS spectrums analysis of the rolling bearings which worked with an artificial defect on the outer raceway under loading of 28 N

During this experiment in FFT spectrums it was observed that by increasing of loading the harmonics' amplitudes of F_{PBO} increased and the $1x F_c$ (-1' and 1') sidebands appeared. Also, it was observed that the F_s frequency and its harmonics predominate in spectrums. In horizontal direction (Fig. 7), the number of harmonics of F_{PBO} increased from $4x F_{PBO} \div 9x F_{PBO}$ to $3x F_{PBO} \div 12x F_{PBO}$ and their amplitudes are much clearer. In vertical direction (Fig. 8) the number of harmonics of F_{PBO} increased from $3x F_{PBO} \div 9x F_{PBO}$ to $3x F_{PBO} \div 12x F_{PBO}$.

In axial direction (Fig. 9) it was observed that by increasing of loading the $8x F_{PBO}$ and $9x F_{PBO}$ harmonics have high amplitudes (even higher than the F_s frequency and its harmonics). The increases of F_{PBO} amplitudes during the experiment can confirm the existence of rolling bearing damage due to implemented defect on the outer raceway.

During this experiment in BCS spectrums analysis (Fig. 10, 11 and 12) for all measuring directions it was observed that by increasing the loading, the amplitudes of F_{PBO} and of its harmonics increased. Also, the $1x F_s$ (-1 and 1), $2x F_s$ (-2 and 2) and $1x F_c$ (-1' and 1') sidebands were observed.

These amplitudes increases of the harmonics of F_{PBO} from FFT spectrums and of the F_{PBO} frequency and of its harmonics from BCS spectrums, as well as the appearance mode of the sidebands give the evolution mode of the artificial defect on the outer raceway when loading is increased from 14 N to 28 N. At the dismounting of the rolling bearing (Fig. 13) these observations are confirmed by establishing the evolution mode of the artificial defect on the outer raceway (a groove of about 8 mm, along the outer raceway in area of the artificial defect and a thermal wear on the balls from the row that is in contact with the artificial defect were developed). Thermal wear in this bearing is present by a color

changing (a blackening) of the superficial layer of the balls' material.

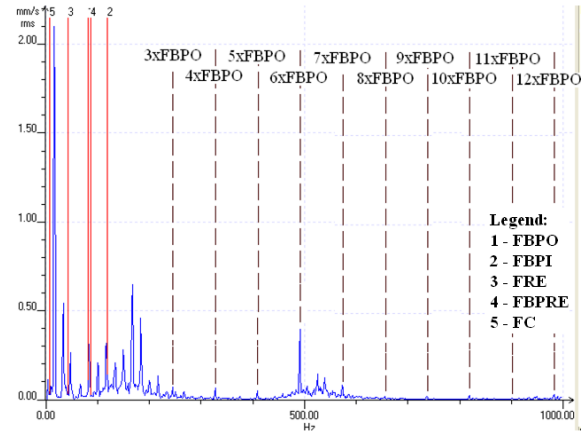


Fig. 7. FFT spectrum of bearing operating under loading of 28 N in the horizontal direction for the 5th measurement

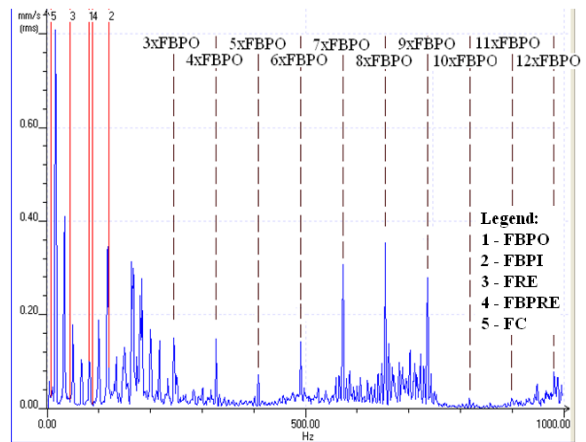


Fig. 8. FFT spectrum of bearing operating under loading of 28 N in the vertical direction for the 3rd measurement

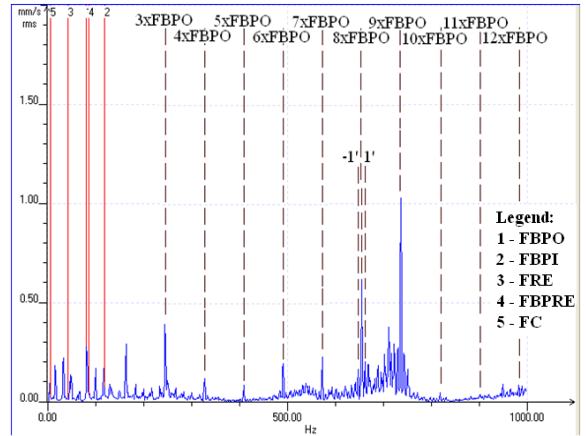


Fig. 9. FFT spectrum of bearing operating under loading of 28 N in the axial direction for the 3rd measurement

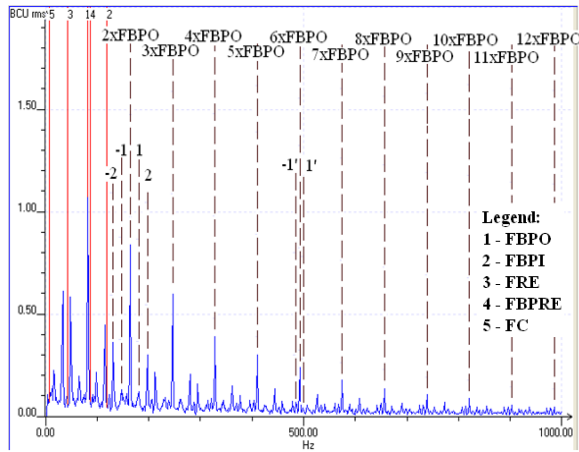


Fig. 10. BCS spectrum of bearing operating under loading of 28 N in the horizontal direction for the 6th measurement

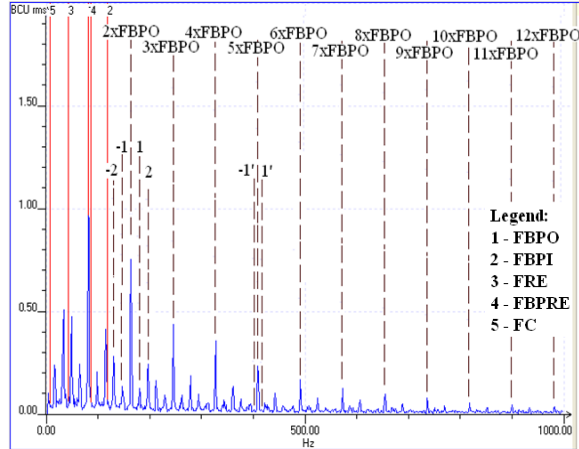


Fig. 11. BCS spectrum of bearing operating under loading of 28 N in the vertical direction for the 5th measurement

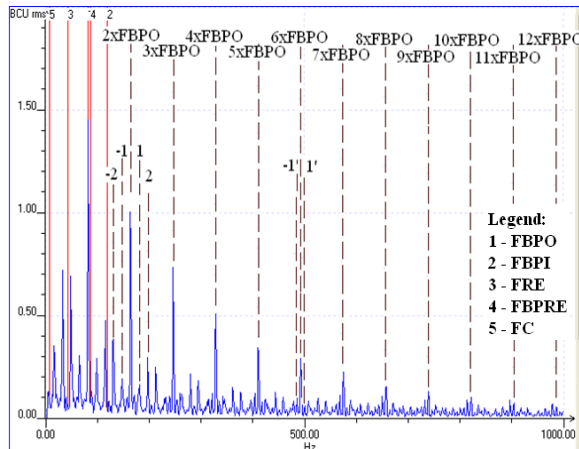


Fig. 12. BCS spectrum of bearing operating under loading of 28 N in the axial direction for the 6th measurement



Fig. 13. Evolution of rolling bearing degradation with artificial defect on the outer raceway after its operation under loading of 28 N

3.3. FFT and BCS spectrums analysis of the rolling bearings which worked with an artificial defect on the outer raceway under loading of 42 N

In FFT spectrums it was observed that by increasing of loading, the harmonics' amplitudes of F_{BPO} and the $1x F_c$ ($-1'$ and $1'$) sidebands are much clearer in all measuring directions. Also, the F_s frequency and its harmonics that predominate in spectrums, were observed. In horizontal direction (Fig.14) at the 6th measurement the harmonics' amplitudes of F_{BPRE} were observed, which confirms the damage of the rolling bearing's ball. In vertical and axial directions this defect characteristic frequency was observed even from the 5th measurement as can be seen in Fig. 15 and 16.

In BCS spectrums for all measuring directions was observed that by increasing of loading, the amplitudes of F_{BPO} and of its harmonics increased.

Thus, in horizontal and vertical directions these amplitudes increased until the 4th measurement, then at the 5th measurement the amplitudes of F_{BPRE} and F_{RE} frequencies were observed. At the 6th measurement, the amplitudes of F_{BPRE} and F_{RE} frequencies and of its harmonics are much higher than F_{BPO} frequency and its harmonics that are more difficult to observe. In axial direction the amplitudes of F_{BPO} and of its harmonics are difficult to observe even from the 5th measurement. These higher amplitudes of F_{BPRE} and F_{RE} frequencies suggest that the balls' damage is more extensive than the outer raceway damage. These observations were confirmed at the dismantling of the rolling bearing (Fig. 20). Thus, along the outer raceway the groove expanded from 8 mm to 41 mm (Fig. 20b), in addition to the thermal wear of the balls there was also a removal of material from the surface layer (Fig. 20a) and inner raceway has a thermal wear with small dimples (small removal of material - fig. 20c).

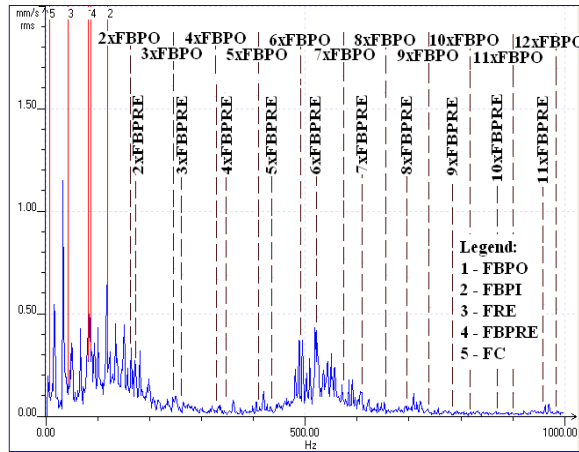


Fig. 14. FFT spectrum of bearing operating under loading of 42 N in the horizontal direction for the 6th measurement

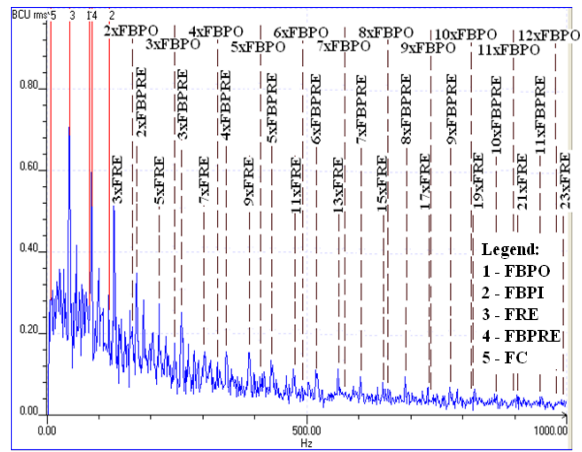


Fig. 17. BCS spectrum of bearing operating under loading of 42 N in the horizontal direction for the 5th measurement

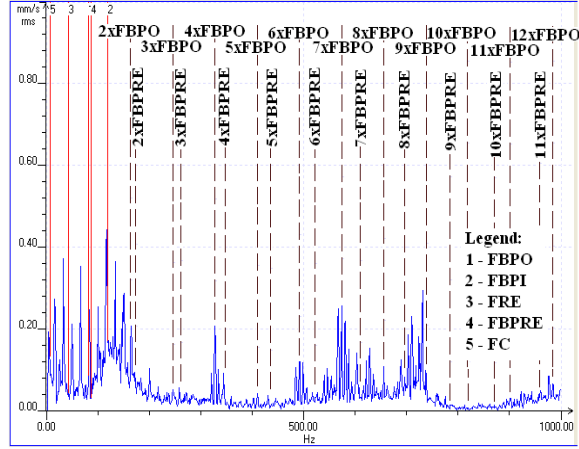


Fig. 15. FFT spectrum of bearing operating under loading of 42 N in the vertical direction for the 5th measurement

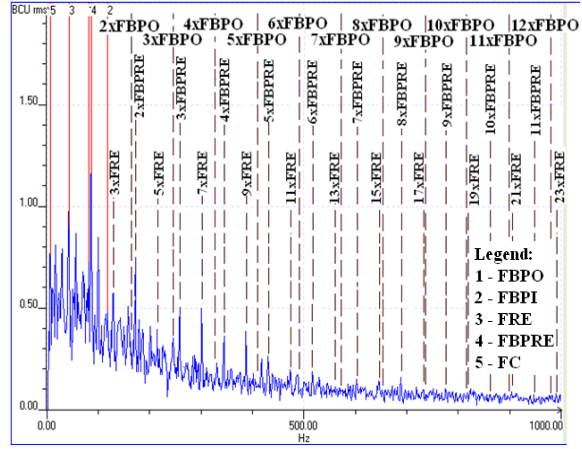


Fig. 18. BCS spectrum of bearing operating under loading of 42 N in the vertical direction for the 5th measurement

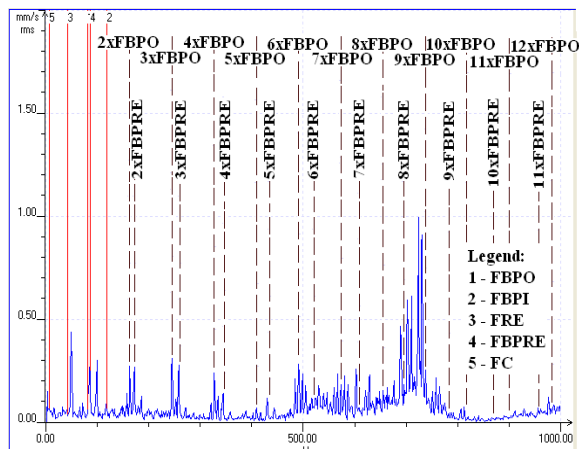


Fig. 16. FFT spectrum of bearing operating under loading of 42 N in the axial direction for the 5th measurement

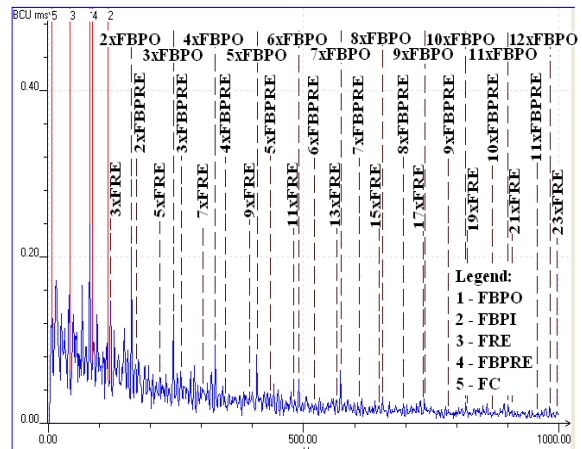


Fig. 19. BCS spectrum of bearing operating under loading of 42 N in the axial direction for the 4th measurement

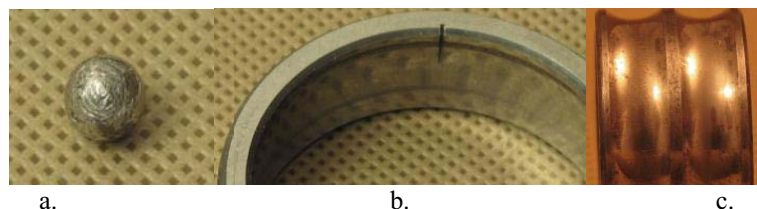


Fig. 20. Evolution of rolling bearing degradation with artificial defect on the outer raceway after its operation under loading of 42 N: a. – on ball; b. – on outer raceway; c. – on inner raceway

4. CONCLUSIONS

Measurement and analysis of vibrations, over time, in different points of dynamic equipments' rolling bearings represent a safe and effective measure for the diagnosis and prediction of their technical state as well as of the entire equipment. The FFT and BCS spectrums analysis give the most effective information on the causes of rolling bearings deterioration during the time passing, but they also give prediction on their remaining lifetime. Thus, the FFT spectrums of this experimental research give information by the appearance of rotation speed amplitudes, F_s , and its harmonics on the existence of an unbalance created by the used loadings, and by the appearance of characteristic defect frequencies' harmonics (F_{BPO} , F_{BPRE} and F_{RE}) on the presence of defects from rolling bearing components. These harmonics of characteristic defect frequencies have random variations in their amplitude both in time and spectrum width. These random variations don't provide sufficient information regarding the evolution mode of rolling bearing deterioration both due to unbalance and when faults occur in their components. On the other hand, in BCS spectrums, amplitudes of characteristic defect frequencies and of its harmonics decrease asymptotically from characteristic defect frequencies to the last harmonic. The BCS spectrums give information regarding the existence of unbalance by the appearance of $1x F_s$ and $2x F_s$ sidebands of characteristic defect frequencies, as well as the existence of different diameters of the rolling elements by $1x F_c$ and $2x F_c$ sidebands. Also, by the appearance and evolution mode of characteristic defect frequencies amplitudes and of its harmonics, BCS spectrums give beneficial information regarding the evolution mode of bearing degradation during the time passing. Thus, in order to have efficiency of the diagnosis and of the prediction of rolling bearings, it is necessary to use FFT and BCS spectrums analysis. For detecting of characteristic defect frequencies, the knowledge of rolling bearing geometrical characteristics is also necessary, but in order to have an effective diagnosis and prediction,

it is required to have an experienced and responsible staff.

REFERENCES

- [1] Orhan S., Akturk N., Celik V.: *Vibration monitoring for defect diagnosis of rolling element bearings as a predictive maintenance tool: Comprehensive case studies*, NDT&E International, 2006, Vol. 39, No. 4, pp. 293 – 298.
- [2] Băjenaru S., Ganga M., Valentin V., Danciu A.: *The study of the diagnosis theory applied for predictive maintenance*, Research Journal of Agricultural Science, 2009, Vol. 41, No. 2, pp. 338-350.
- [3] Balerston H. L.: *The Detection of Incipient Failure in Bearings*, Materials Evaluation, 1996, Vol. 27, pp. 121 – 128.
- [4] Tse P., Peng Y., Yam R.: *Wavelet analysis and envelope detection for rolling element bearing fault diagnosis their effectiveness and flexibilities*, Journal of Vibration and Acoustics, 2001, Vol. 123, pp. 303–310.
- [5] Mobley K. R.: *Root Cause Failure Analysis*, Reed Elsevier, USA, 1999.
- [6] Nadabaica D. C., Bibire L., Andrioai G.: *Study of the advantages of predictive maintenance in the monitoring of rolling bearings*, Environmental Engineering and Management Journal, 2012, Vol. 11, No. 12, pp 2233-2238.
- [7] Ragulskis K., Yurkauskas A.: *Vibration of Bearing*, Hemisphere Publishing Corporation, Bristol, 1989.
- [8] Rieger N. F., Crofoot J. F.: *Vibration of Rotational Machinery*, Rochester Institute of Technology, 1977, pp.69-77.
- [9] Al-Hazmi M.W.: *The Effect Of The Manufacturing Errors On The Dynamic Performance Of Gears*, Journal of Engineering & Architecture, 2011, Vol. 4, No. 2, pp. 37-53.
- [10] Dennis H. S.: *Signal Processing For Effective Vibration Analysis*, IRD Mechanalysis, Inc. Columbus, Ohio, 1995.

**Dumitru - Cristinel**

NADABAICA is PhD student and associate assistant in Environmental Engineering and Mechanical Engineering Department, Engineering Faculty, "Vasile Alecsandri" University of Bacau. In his works he explores issues of the diagnostic of process equipments failure and the prognosis of their remaining lifetime.



Prof. Valentin NEDEFF, PhD is Rector of "Vasile Alecsandri" University of Bacau and professor in Environmental Engineering and Mechanical Engineering Department, Engineering Faculty. In his scientific work he deals with research in mechanical and environmental field.



Prof. Stanisław RADKOWSKI, professor in the Institute of Vehicles of the Warsaw University of Technology. In his scientific work he deals with vibroacoustic diagnosis, technical risk analysis and energy harvesting.



Dr inż. Jędrzej MĄCZAK, PhD, is an assistant professor at the Institute of Vehicles of the Warsaw University of Technology. His scientific interests are distributed diagnostic systems, machine diagnostics and analysis of the vibroacoustic signals.

FRICTION COMPENSATION IN NONLINEAR DYNAMICAL SYSTEMS USING FAULT-TOLERANT CONTROL METHODS

Marcello BONFÈ*, Paolo CASTALDI**, Nicola PREDA*, Silvio SIMANI*

* University of Ferrara, Department of Engineering
Via Saragat 1, 44122 Ferrara, Italy, e-mail: (name.surname)@unife.it
**University of Bologna, Aerospace Engineering Campus
Via Fontanelle 40, 47100 Forlì, Italy, e-mail: paolo.castaldi@unibo.it

Summary

This paper describes the application of differential geometry and nonlinear systems analysis to the estimation of friction effects in a class of mechanical systems. The proposed methodology relies on adaptive filters, designed with a nonlinear geometric approach to obtain the disturbance de-coupling property, for the estimation of the friction force. Thanks to accurate estimation, friction effects are compensated by injecting the on-line estimate of friction force to the control action calculated by a standard linear state feedback. The inverted pendulum on a cart is considered as an application example and the proposed approach is compared with a commonly used friction compensation strategy, based on an explicit model of the friction force.

Key words: Fault-Tolerant Control, Friction Compensation, Nonlinear Systems, Differential Geometry

INTRODUCTION

Feedback control systems for engineering applications are often affected by friction in mechanical components. Detailed modeling of friction effects has been the subject of many research activities [1] and the inverted pendulum system is commonly adopted as a benchmark for control design including friction compensation [2]. The most challenging problem for on-line estimation of friction is the identification of modelling parameters, which are mostly not directly measurable and possibly varying in time. Therefore, there is a growing demand for robust and adaptive algorithms for friction estimation and compensation.

This problem has been addressed in literature also as a fault-tolerant control problem [3]. A fault-tolerant control system can include a Fault Detection and Diagnosis (FDD) module [4], which is mainly used to fulfil the requirement of fault estimation and allow the controller to react to the system component failures actively, by reconfiguring its actions so that the stability and acceptable performance of the entire system can be maintained. This kind of structure is classified as an Active Fault-Tolerant Control Scheme (AFTCS).

This paper is focused on the application of an AFTCS to address the problem of friction compensation. The proposed AFCTS integrates a reliable and robust friction estimation module, implemented according to an FDD procedure relying on adaptive filters. The controller reconfiguration exploits a second control loop depending on the on-line estimate of the friction force. The advantages of this strategy are that a structure of logic-based switching controller is not

required and, instead, an existing controller can be preserved and enhanced.

The FDD method is based on the Nonlinear Geometric Approach (NLGA) developed in [5]. By means of this framework, a disturbance de-coupled adaptive nonlinear filter providing the fault identification is designed. It is worth observing that the original NLGA FDD scheme of [5], based on residual signals, cannot provide fault size estimation.

Both the NLGA Adaptive Filters (NLGA-AF) and the AFTCS strategy are applied to an inverted pendulum on a cart (also called cart-pole system), an underactuated mechanical structure that is commonly used as a benchmark system for control design and mechatronics prototyping. A simulation model for the complete AFTCS loop has been implemented in the Matlab/Simulink® environment, and tested in the presence of nonlinear friction, disturbances, measurement noise and modelling errors.

The work proceeds with Section 1, providing the description of the cart-pole nonlinear benchmark system, Section 2, describing the implementation of the FDD scheme and the structure of the AFTCS strategy, and Section 3, in which stability, robustness and advantages of the AFTCS method over simpler friction compensators are investigated with simulations. Section 5 summarises contributions and achievements of the paper.

1. THE CART-POLE NONLINEAR MODEL

The dynamic model of a pendulum (or pole) on a cart shown in Fig. 1 is a classical benchmark in Systems and Control Theory.

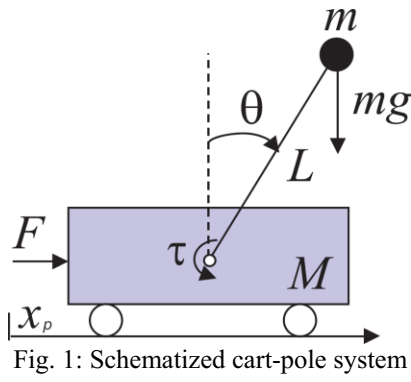


Fig. 1: Schematized cart-pole system

The interest in this mechanical system is motivated by the similarity between its dynamic properties and those of several real-world engineering applications like, for example, aerospace vehicles during vertical take-off, cranes, and many others. Assuming that the cart has mass M and the pendulum mass m is concentrated at the tip of a pole, with neglectable inertia, of length L , the dynamic model obtained using Hamilton's principle is the following:

$$\begin{cases} (M+m)\ddot{x}_p + mL\ddot{\theta}\cos\theta - mL\dot{\theta}^2\sin\theta = F_a - F_{fric} \\ m\ddot{x}_p\cos\theta + mL\ddot{\theta} - mgsin\theta = \tau \end{cases} \quad (1)$$

in which g is the gravity constant, F_a is the controllable actuator force, F_{fric} is the friction involved by the contact between cart and ground, and τ is a torque acting directly at the base of the pole. The state variables are $x=[x_1 \ x_2 \ x_3 \ x_4]^T = [x_p \ \dot{x}_p \ \theta \ \dot{\theta}]^T$ and the control input is $u=F_a$, while $d=\tau$ is considered as a disturbance, so that the model can be rewritten in the following state-space input affine form:

$$\begin{cases} \dot{x}_1 = x_2 \\ \dot{x}_2 = \frac{mLx_4^2\sin x_3 - mgsin x_3 \cos x_3}{M+m\sin^2 x_3} + \\ \quad + \frac{u-F_{fric}}{M+m\sin^2 x_3} - \frac{d}{(M+m\sin^2 x_3)L} \\ \dot{x}_3 = x_4 \\ \dot{x}_4 = \frac{(M+m)gsin x_3 - mLx_4^2\sin x_3 \cos x_3}{(M+m\sin^2 x_3)L} + \\ \quad - \frac{(u-F_{fric})\cos x_3}{(M+m\sin^2 x_3)L} + \frac{(M+m)d}{m(M+m\sin^2 x_3)L^2} \end{cases} \quad (2)$$

It is worth noting that considering τ (i.e. the torque acting at the base on the pole) as a disturbance terms represents a realistic situation, since it may be related to the effect of an impact between the pole and some kind of obstacle.

3. FDD AND AFTCS DESIGN

The presented FDD scheme belongs to the NLGA framework, that allows to de-couple disturbances by means of a nonlinear coordinate transformation. Such a transformation is then the starting point to design a set of adaptive filters that

are able to both detect additive fault acting on a single actuator and estimate the magnitude of the fault. It is worth observing that in this paper, we can consider the effect of friction as a fault affecting the actuator, so that thanks to the NLGA approach the friction estimate is de-coupled from disturbance d .

The proposed approach can be applied to nonlinear systems in the form:

$$\begin{cases} \dot{x} = n(x) + g(x)u + l(x)f + p_d(x)d \\ y = h(x) \end{cases} \quad (3)$$

where the state vector $x \in X$ (an open subset of R^n), $u \in R^{l_c}$ is the control input vector, $f \in R$ is the fault, $d \in R^{l_d}$ the disturbance vector and $y \in R^{l_m}$ the output vector, whilst $n(x)$, $l(x)$, the columns of $g(x)$, and $p_d(x)$ are smooth vector fields and $h(x)$ is a smooth map. The model of Eq. 2 can be related to the form of Eq. 3 setting:

$$n(x) = \begin{bmatrix} x_2 \\ \frac{mLx_4^2\sin x_3 - mgsin x_3 \cos x_3}{M+m\sin^2 x_3} \\ x_4 \\ \frac{(M+m)gsin x_3 - mLx_4^2\sin x_3 \cos x_3}{(M+m\sin^2 x_3)L} \end{bmatrix}$$

$$g(x) \equiv l(x) = \begin{bmatrix} 0 \\ 1 \\ \frac{M+m\sin^2 x_3}{\cos x_3} \\ -\frac{\cos x_3}{(M+m\sin^2 x_3)L} \end{bmatrix}$$

$$p_d(x) = \begin{bmatrix} 0 \\ \frac{\cos x_3}{(M+m\sin^2 x_3)L} \\ 0 \\ \frac{M+m}{m(M+m\sin^2 x_3)L^2} \end{bmatrix}$$

Assuming in addition that the full state vector is measurable (i.e. $h(x)=I_4x$), the design of the strategy for the diagnosis of the fault f with disturbance de-coupling is organised as follows:

- computation of \sum_*^P , i.e. the minimal conditioned invariant distribution containing P (where P is the distribution spanned by the columns of $p_d(x)$);
- computation of Ω^* , i.e. the maximal observability codistribution contained in $(\sum_*^P)^\perp$;
- if $l(x) \notin (\Omega^*)^\perp$, the fault is detectable and a suitable change of coordinate can be determined.

The computation of \sum_*^P can be obtained by means of the following recursive algorithm:

$$\begin{cases} S_0 &= \bar{P} \\ S_{k+1} &= \bar{S} + \sum_{i=0}^m [g_i, \bar{S}_k \cap \ker\{dh\}] \end{cases} \quad (4)$$

where m is the number of inputs, \bar{S} is the involutive closure of S , $[g, \Delta]$ is the distribution spanned by all vector fields $[g, \tau]$ in which $\tau \in \Delta$, and $[g, \tau]$ is the Lie Bracket of g and τ . It can be shown that if there exists a $k \geq 0$ such that $S_{k+1} = S_k$, the algorithm of Eq.4 stops and $\sum_*^P = S_k$.

Once \sum_*^P is determined, Ω^* can be obtained with the following algorithm:

$$\begin{cases} Q_0 &= (\Sigma_*^P)^\perp \cap \text{span}\{dh\} \\ Q_{k+1} &= (\Sigma_*^P)^\perp \cap \sum_{i=0}^m [L_{g_i} Q_k + \text{span}\{dh\}] \end{cases} \quad (5)$$

where $L_g \Gamma$ denotes the codistribution spanned by all covector fields $L_g \omega$, with $\omega \in \Gamma$, and $L_g \omega$ is the derivative of ω along g . If there exists an integer k^* , such that $Q_{k^*+1} = Q_{k^*}$, then Q_{k^*} is indicated as o.c.a. ($(\Sigma_*^P)^\perp$), where o.c.a. stands for *observability codistribution algorithm*.

It can be shown that $Q_{k^*} = \text{o.c.a. } ((\Sigma_*^P)^\perp)$ represents the maximal observability codistribution contained in P^\perp , i.e. Ω^* (see [5]). Therefore, when $l(x) \notin (\Omega^*)^\perp$ the disturbance d can be de-coupled and the fault f is detectable.

As mentioned above, the considered NLGA to the fault diagnosis problem, described in [5], is based on a coordinate change in the state space and in the output space, respectively denoted as $\Phi(x)$ and $\Psi(y(x))$, which are local diffeomorphisms structured as follows:

$$\begin{cases} \Phi(x) &= \begin{pmatrix} \bar{x}_1 \\ \bar{x}_2 \\ \bar{x}_3 \end{pmatrix} = \begin{pmatrix} \Phi_1(x) \\ H_2 h(x) \\ \Phi_3(x) \end{pmatrix} \\ \Psi(y) &= \begin{pmatrix} \bar{y}_1 \\ \bar{y}_2 \end{pmatrix} = \begin{pmatrix} \Psi_1(y) \\ H_2 y \end{pmatrix} \end{cases} \quad (6)$$

such that $\Omega^* \cap \text{span}\{dh\} = \text{span}\{d(\Psi_1 \circ h)\}$, $\Omega^* = \text{span}\{d\Phi_1\}$ and the rows of H_2 are a subset of the rows of the identity matrix. By using the new local coordinates (\bar{x}, \bar{y}) , the system 4 is transformed so that it exhibits an observable subsystem that is affected by the fault and not affected by the disturbance, as described in [5]:

$$\begin{cases} \dot{\bar{x}}_1 &= n_1(\bar{x}_1, \bar{x}_2) + g_1(\bar{x}_1, \bar{x}_2)c + \\ &\quad + l_1(\bar{x}_1, \bar{x}_2, \bar{x}_3)f \\ \bar{y}_1 &= h(\bar{x}_1) \end{cases} \quad (7)$$

In the case of the cart-pole system, the following result is obtained:

$$\begin{aligned} S_0 &= \bar{P} = \text{cl}(p_d(x)) = \\ &= \text{cl} \left(\begin{bmatrix} 0 \\ -\frac{\cos x_3}{(M+m \sin^2 \bar{x}_3)L} \\ 0 \\ \frac{M+m}{m(M+\sin^2 \bar{x}_3)L^2} \end{bmatrix} \right) \equiv p_d(x) \end{aligned} \quad (8)$$

Assuming that the full cart-pole state is measurable, $\ker\{dh\} = \emptyset$, so that it follows $\sum_*^P = \bar{P}$ as $S_0 \cap \ker\{dh\} = \emptyset$. Thus, the algorithm of Eq.3 stops with immediately ($k=0$).

Proceeding with the algorithm of Eq. 4, it can be observed that:

$$\begin{aligned} (\bar{P})^\perp &= \left(\begin{bmatrix} 0 \\ -\frac{\cos x_3}{(M+m \sin^2 \bar{x}_3)L} \\ 0 \\ \frac{M+m}{m(M+\sin^2 \bar{x}_3)L^2} \end{bmatrix} \right)^\perp = \\ &= \begin{bmatrix} 1 & 0 & 0 & 0 \\ 0 & 0 & 1 & 0 \\ 0 & 1 & -\frac{mLx_4 \sin \bar{x}_3}{M+m} & \frac{mL \cos \bar{x}_3}{M+m} \end{bmatrix} \end{aligned} \quad (9)$$

and $\text{span}\{dh\} = I_4$. From the first step of the algorithm it follows that $\Omega^* = (\Sigma_*^P)^\perp = (\bar{P})^\perp$ and that $(\Omega^*)^\perp = \Sigma_*^P = \bar{P}$. Therefore, the fault (i.e. the friction force) is detectable, since $l(x) \notin (\Omega^*)^\perp$.

Since the dimension of Ω^* and of $\Omega^* \cap \text{span}\{dh\} = \text{span}\{d(\Psi_1 \circ h)\}$ is 3, it follows that $\Phi_1(y): \mathbb{R}^4 \rightarrow \mathbb{R}^3$ and that $H_2 y: \mathbb{R}^4 \rightarrow \mathbb{R}^1$ (the component $\Phi_3(x)$ is not present in this case). Thus, as $h(x) = I_4 x$ the surjection $\Psi(y(x))$ can be defined as follows:

$$\Psi(y(x)) = \begin{pmatrix} \Psi_1(x) \\ H_2 x \end{pmatrix} = \begin{pmatrix} x_2 + \frac{mLx_4 \cos \bar{x}_3}{M+m} \\ x_1 \\ x_3 \\ x_4 \end{pmatrix}$$

where $H_2 = [0 \ 0 \ 0 \ 1]$. Moreover, $\bar{x}_1 = \Phi_1(x) = \Psi_1(x)$ is the state variable of the observable subsystems that is decoupled from the disturbance.

Given this result, the NLGA-AF can be designed introducing the following additional constraint [6]: there exists a proper scalar component \bar{x}_{1s} of the

state vector $\bar{\mathbf{x}}_1$ such that the corresponding scalar component of the output vector $\bar{y}_{1s} = \bar{\mathbf{x}}_{1s}$ and the following relation holds:

$$\dot{\bar{y}}_{1s}(t) = M_1(t) \cdot f + M_2(t) \quad (10)$$

which means that the effect of the fault signal can be properly isolated. The functions M_1 and M_2 are generally computed from both inputs and outputs measurements of the system under diagnosis. The fault estimation is then obtained thanks to the following adaptive filter based on the least-squares algorithm with forgetting factor described in [7]:

$$\begin{cases} \dot{P} = \beta P - \frac{1}{N^2} P^2 \tilde{M}_1^2, & P(0) = P_0 > 0 \\ \dot{\hat{f}} = P \epsilon \tilde{M}_1, & \hat{f}(0) = 0 \end{cases} \quad (11)$$

with the following equations describing the output estimation and the corresponding normalized estimation error:

$$\begin{cases} \hat{y}_{1s} = \tilde{M}_1 \hat{f} + \tilde{M}_2 + \lambda \bar{y}_{1s} \\ \epsilon = \frac{1}{N^2} (\bar{y}_{1s} - \hat{y}_{1s}) \end{cases} \quad (12)$$

Finally, the signals $\tilde{M}_1, \tilde{M}_2, \bar{y}_{1s}$ are obtained by means of low-pass filtering of the signals M_1, M_2, \bar{y}_{1s} . The design parameters that must be properly tuned for the desired application are:

- $\lambda > 0$ is the bandwidth of the low-pass filters required by the computation of $\tilde{M}_1, \tilde{M}_2, \bar{y}_{1s}$
- $\beta > 0$ is the forgetting factor of the adaptation algorithm
- $N^2 = 1 + \tilde{M}_1^2$ is the normalisation factor of the least-squares algorithm.

In order to de-couple the effect of the disturbance d from the fault (i.e. friction) estimator, it is necessary to select from the observable subsystem the following state:

$$\bar{x}_{1s} = \bar{x}_{11} = x_2 + \frac{mLx_4 \cos \bar{x}_3}{M+m} \quad (13)$$

whose differentiation allows to compute the full expression of M_1 and M_2 , namely:

$$M_1 = \frac{1-m \cos^2 x_3 / (m+M)}{M+m \sin^2 \bar{x}_3} \quad (14)$$

$$\begin{aligned} M_2 = & \frac{(1-m \cos^2 x_3) m L x_4^2 \sin x_3}{M+m \sin^2 \bar{x}_3} - \frac{m L x_4^2 \sin x_3}{m+M} + \\ & - \frac{1-m \cos^2 x_3 / (m+M)}{M+m \sin^2 \bar{x}_3} u \end{aligned} \quad (15)$$

4. SIMULATION RESULTS

To compute with Matlab/Simulink® the simulations results described in this section, the AFTCS design has been completed by means of an optimal state feedback control law, on the basis of the linear approximation of a frictionless version of Eq. 2, in a neighborhood of $x_0 = [x_{1d} \ 0 \ 0 \ 0]^T$, in which x_{1d} can be any value. In fact, the linear approximation is independent from x_1 , so that the input vector of the optimal controller can be calculated as $x_e = [(x_1 - x_{1d}) \ x_2 \ x_3 \ x_4]$ and the cart-pole system will be stabilised in the upright position at any linear position reference. The full control loop is therefore the one shown in Fig. 2.

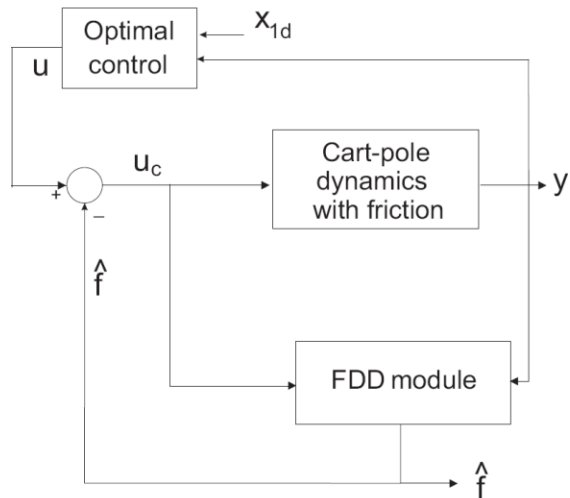


Fig. 2: Control loop with proposed AFTCS

The following values of the system parameters have been assumed: $M = 1$ kg; $m = 0.1$ kg; $L = 0.3$ m; $g = 9.81$ m/s². The optimal controller has been designed using the LQR approach in order to minimize the standard quadratic cost function of state and input, with $Q = 10 I_4$ and $R = 1$.

The simulation of the mechanical system has been completed by a nonlinear model of friction affecting the linear motion of the cart, including viscous friction and Stribeck friction, with Coulomb and static part, using the following mathematical description:

$$F_{fric} = [F_c + (F_s - F_c) e^{-\left(\frac{|\dot{x}_p|}{v_s}\right)^2}] \text{sign}(\dot{x}_p) + F_x \dot{x}_p \quad (16)$$

in which $F_x = 0.6$ N/m/s is the viscous coefficient, $F_c = 0.25$ N is the Coulomb coefficient, $F_s = 0.4$ N is the static part coefficient and $v_s = 0.02$ m/s is the Stribeck velocity. This friction model is commonly accepted as compatible with experimental observations (see [1] and [2]). However, many industrial motion control systems adopts simpler models for direct compensation of the friction force. In particular, the most used approximation of the model in Eq. 16, as implemented in industrial controllers, disregard the Stribeck effect and include

only viscous and Coulomb friction, obtaining the following model:

$$F_{fric} = F_c \operatorname{sign}(x_p) + F_x \dot{x}_p \quad (17)$$

The plot in Fig. 3 shows the different shapes of the two nonlinear friction models of Eq. 16 and Eq. 17.

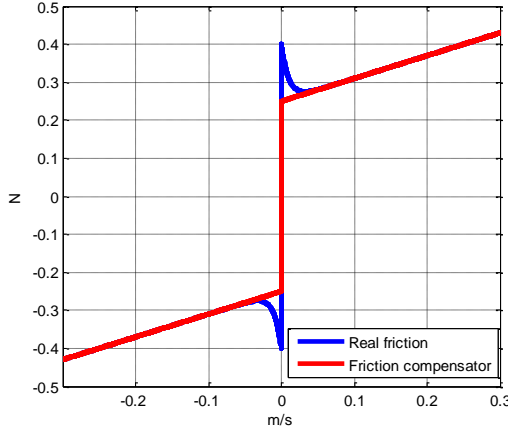


Fig. 3: Friction model with Stribeck effect and model used by standard compensation algorithms of industrial controllers

As can be seen, the simplified model matches the more detailed one if the velocity is sufficiently large, while it deviates significantly at low velocities. Moreover, the friction compensation based on a direct model of the friction effect requires necessarily a long and accurate tuning procedure, based on experimental data. The design of experiments themselves is also quite critical for an effective identification of friction parameters, as described in [1] and [2].

With approach based on the proposed AFTCS, instead, the friction force is adaptively estimated online. In the particular case of the cart-pole system, only mechanical parameters that can be quite easily measured (i.e. the masses m and M and the pole length L) are required.

The effectiveness of the methodology has been evaluated as follows. The NLGA-AF used as a friction estimator has been designed assuming the nominal model of the cart-pole, but the simulated mechanical system included a mismatch of 10% in the values of M and m , a random disturbance torque d (which is nevertheless de-coupled by design) and measurement noise on the state feedback signals. As can be seen from Fig. 4, the proposed NLGA-based estimator provides an accurate and robust measure of the actual friction force, even if the mathematical model of friction effects is not explicitly included in the design of the estimator. Such effective performance is achieved by means of a proper tuning of the adaptation mechanism of the filter, in particular $\beta = 12$ and $\lambda = 8:8$ have been fixed for the simulated case.

The same Fig. 4 shows also the friction force estimated by the model of Eq. 17, assuming instead that a perfect tuning of the parameters F_x and F_c can be achieved. As can be seen, since the simulated experiment is performed at relatively low velocities (which is a common operating mode for the considered mechanical system, since higher velocities would make more challenging the stabilization of the inverted pendulum), the estimation is not capable of tracking accurately the real friction force. Moreover, since the velocity measurement is assumed to be noisy, a low-pass filter (with the same bandwidth λ used for the AFTCS) is applied before the calculation of the friction model. Otherwise, at low velocities the noise could even reverse inconsistently the sign of the measurement and, therefore, change the sign of the estimated force, which would have a great impact on the performance of the control system if such an estimate is used for compensation.

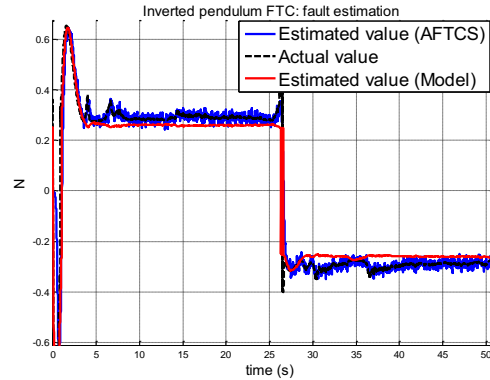


Fig. 4: Friction force estimation obtained with the proposed AFTCS (blue) and with the model used by standard compensation algorithms of industrial controllers (red)

Thanks to its reconstruction, friction can in fact be compensated by simply adding its estimated value to the output of the optimal controller. As a result, the tracking of a time-varying linear cart position reference is dramatically improved, as shown in Fig. 5. The figure shows that in the first half of the plot the optimal controller by itself is not robust with respect to the nonlinear friction disturbing action, while in the second part of the simulation, friction compensation on the basis of either the NLGA-AF estimation or the simplified model of Eq. 17 is introduced and tracking error is reduced.

The performance of the two kind of compensators is not significantly different in this case, though a magnified plot shown in Fig. 6 reveals a small advantage of the AFTCS. However, it should be noted that the latter is adaptive by design, so that components aging and absence of lubrication or maintenance would never affect its performance in a practical application, as is instead

commonly the case when a model-based friction compensator is used.

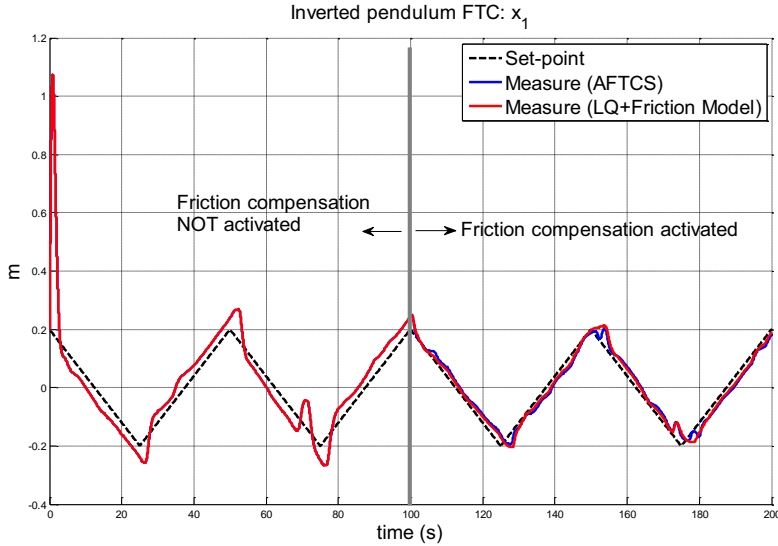


Fig. 5: Tracking of a sawtooth reference for the linear position of the cart, without (right) and with (left) friction compensation. In the latter case, friction is compensated using either the NLGA-AF system (blue) or the simplified direct model (red)

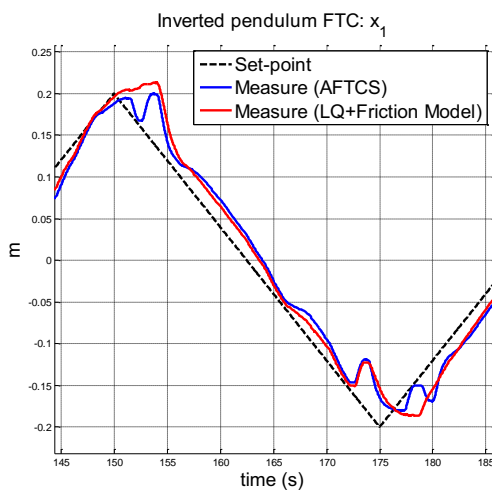


Fig. 6: Detail of the tracking plot for the linear position of the cart, with friction compensated by the NLGA-AF (blue) or the simple model (red)

5. CONCLUSION

This paper described the development of an active fault tolerant control scheme for the purpose of friction compensation in mechanical systems, which integrates a robust fault diagnosis method providing accurate estimation of friction effects. The methodology relies on disturbance de-coupled adaptive filters designed via the nonlinear geometric approach. The fault tolerant strategy has been applied to a classical control design benchmark, namely the inverted pendulum on a cart, which was simulated in presence of nonlinear friction,

disturbing torque acting on the pole pivot, measurement noise and modelling errors.

It is worth observing that the suggested active fault tolerant control was already developed in works by the same authors, but applied to aerospace examples. Thus, the contribution of this paper consists of the application of the active fault tolerant control scheme to the well-known benchmark, in order to highlight the computational and mathematical aspects of the nonlinear disturbance de-coupling design, and hence it can be considered also as a tutorial for researchers working in mechanical systems monitoring and fault diagnosis, as well as fault tolerant control and friction compensation.

The proposed fault tolerant scheme allows to maintain the existing controller, since a further loop is added to the original scheme, thus providing the feedback of the adaptive friction estimate provided by the nonlinear geometric approach diagnosis module. The final performances of the developed fault tolerant control strategy are mainly due to the fact that the estimate is unbiased, thanks to disturbance de-coupling method. Moreover, when compared with other commonly used friction compensation methods, based on explicit models of the friction force, the proposed methodology has the advantage of being insensitive to parameter variation in the friction effect. The application of the proposed AFTCS is currently under evaluation on real case studies represented by didactical laboratory systems and industrial robotic manipulators.

REFERENCES

- [1] Olsson, H., Astrom, K., de Wit, C., Gafvert, M., Lischinsky, P., *Friction models and friction compensation*. European Journal of Control Vol. 4, N. 3, pp. 176–195 (1998).
- [2] Campbell S, Crawford S, Morris K. *Friction and the Inverted Pendulum Stabilization Problem*. Journal of Dynamic Systems, Measurement and Control, Vol. 130, N. 5, 2008.
- [3] Patton, R., Putra, D., Klinkhieo, S., *Friction compensation as a fault-tolerant control problem*. International Journal of Systems Science, Vol. 41, N. 8, 2010.
- [4] Isermann, R.: *Fault-Diagnosis Systems: An Introduction from Fault Detection to Fault Tolerance*, Springer-Verlag, 2005.
- [5] De Persis, C., Isidori, A., *A geometric approach to non-linear fault detection and isolation*. IEEE Transactions on Automatic Control, Vol. 45, N 6, pp. 853–865, 2001.
- [6] Castaldi, P., Geri, W., Bonfè, M., Simani, S., Benini, M., *Design of residual generators and adaptive filters for the FDI of aircraft model sensors*. Control Engineering Practice, Vol. 18, N. 5, pp. 449–459, 2010.
- [7] Ioannou, P., Sun, J., *Robust Adaptive Control*. Prentice-Hall, 1996.



Marcello BONFÈ received his M.Sc. degree in Electronic Engineering in 1998, and the Ph.D. degree in Information Engineering in 2003. Currently, he is an assistant professor of Automatic Control at the Department of Engineering of the University of Ferrara, Italy. He has published about 70 refereed journal and conference papers on fault detection and isolation, modelling and control of mechatronic systems, and formal verification methods for discrete event systems.



Paolo CASTALDI received the Laurea degree (cum laude) in Electronic Engineering in 1990 and the Ph.D degree in System Engineering in 1994. Since 1995 he has been an Assistant Professor at the Department of Electronics, Computer Science and Systems of the University of Bologna. Since 2009 he has been a member of the IFAC Technical Committee on Aerospace. His research interests include fault diagnosis and fault tolerant control, adaptive filtering, system identification, and their applications to aerospace and mechanical systems.



Nicola PREDA received the Bachelor degree in 2007 and the Master degree in 2011, both in Automation Engineering at the University of Ferrara. Since 2012 he is a PhD student in Engineering Science

at the University of Ferrara and he is working on an FP7 EU project for the development of intelligent surgical robots.



Silvio SIMANI received in 1996 the Laurea degree (cum laude) in Electronic Engineering, and in 2000 the Ph.D. in Information Science (Automatic Control). Since 2006 he has been an IEEE Senior Member, and from 2000 a member of the SAFEPROCESS Technical Committee. Since 2002 he has been an Assistant Professor at the Department of Engineering of the University of Ferrara. His research interests include fault diagnosis, fault tolerant control, and system identification, on which he published about 100 refereed journal and conference papers, as well as two books.

ART-2 ARTIFICIAL NEURAL NETWORKS APPLICATIONS FOR CLASSIFICATION OF VIBRATION SIGNALS AND OPERATIONAL STATES OF WIND TURBINES FOR INTELLIGENT MONITORING

Tomasz BARSZCZ¹, Andrzej BIELECKI², Mateusz WÓJCIK³, Marzena BIELECKA⁴

¹ AGH University of Science and Technology, Faculty of Mechanical Engineering and Robotics,
al.Mickiewicza 30, 30-059 Cracow, Poland, tbarscz@agh.edu.pl

² AGH University of Science and Technology, Faculty of Electrotechnics, Automation, Computer Science and
Biomedical Engineering, al. Mickiewicza 30, 30-059 Cracow, Poland azbielecki@gmail.com

³ Jagiellonian University, Faculty of Physics, Astronomy and Applied Computer Science,
ul. Reymonta 4, 30-059 Cracow, Poland, mateusz.wojciech@uj.edu.pl

⁴ AGH University of Science and Technology, Faculty of Geology, Geophysics and Environmental
Protection, Mickiewicza 30, 30-059 Cracow, Poland, bielecka@agh.edu.pl

Summary

In recent years wind energy is the fastest growing branch of the power generation industry. The largest cost for the wind turbine is its maintenance. A common technique to decrease this cost is a remote monitoring based on vibration analysis. Growing number of monitored turbines requires an automated way of support for diagnostic experts. As full fault detection and identification is still a very challenging task, it is necessary to prepare an “early warning” tool, which would focus the attention on cases which are potentially dangerous. There were several attempts to develop such tools, in most cases based on various classification methods. As the ART neural networks are capable to perform efficient classification and to recognize new states when necessary, they seem to be a proper tool for classification of vibration signals of bearing in gears in wind turbines. The verification of ART-2 networks efficiency in this task is the topic of this paper.

Keywords: wind turbines, monitoring, ART neural network

1. INTRODUCTION

In recent years wind energy is the fastest growing branch of the power generation industry. The average yearly growth in the years 1997-2003 achieved 32% in the United States and 22% in the European Union [4] and these figures will hold for at least the next decade. The distribution of costs during the life cycle of the unit for wind energy is significantly different from that of traditional, fossil fired units [4]. First of all, initial investment costs are relatively higher, whereas in traditional units cost of fuel plays important role (usually it is the second largest cost). After commissioning, the largest cost for the wind turbine (WT for abbreviation) is maintenance. With proper maintenance policies, wind turbines can achieve the highest level of availability in the power generation sector - even up to 98%.

Therefore, condition monitoring of wind turbines, including fault diagnostics, in particular at the early stage of a fault occurrence or even participatory actions, is an essential problem in wind turbines engineering in particular [7, 9, 12] and in rotating machinery engineering in general [1]. There were several attempts to develop various monitoring tools, in most cases based on various classification methods. Some of them are based on artificial neural networks (ANNs for abbreviation). In most types of ANNs the learning process is unsuitable for cases of continuous machinery intelligence monitoring. This means, among others, that adding new patterns as inputs requires repetition of the learning process. In ART networks, introduced by Car-

penter and Grossberg [5, 6], the learning process is not separated from its operation. Furthermore, ART neural networks are capable to add new states when necessary [11, 13, 16]. Therefore, this sort of ANNs was tested as a tool for classification of states in continuous monitoring.

2. THE MACHINE DESCRIPTION

The faults which are sought in wind turbines are primarily of mechanical origin. The wind turbine with the gearbox, which is the most popular type, can be described in the following way. The main rotor with three blades is supported by the main bearing and transmits the torque to the planetary gear. The main rotor is connected to the plate which is the gear input. The planetary gear has three planets, with their shafts attached to the plate. The planets roll over the stationary ring and transmit the torque to the sun. The sun shaft is the output of the planetary gear. The sun drives the two-stage parallel gear which has three shafts: the slow shaft connected to the sun shaft, the intermediate shaft and the fast shaft, which drives the generator. The overall gear ratio is in the range of 1:100. The generator produces alternating current of slightly varying frequency. This current is converted first into direct current power and then into alternating current power of frequency equal to the grid frequency. Electric transformations are performed by the controller at the base of the tower - see Fig. 1.

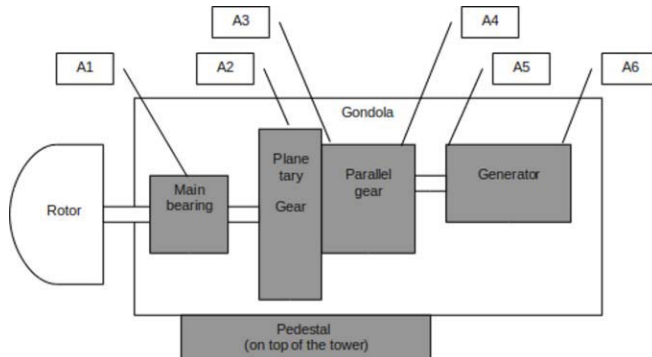


Fig. 1. The mechanical structure of the wind turbine. Location of vibration measurement sensors is shown by An symbols

In the field of vibrodiagnostics, a machine operational state is understood as an accepted range of machines operational points enabling referential analysis. In practice, machine operating point is defined by values of available measurements of physical quantities such as speed, load, pressure, temperature, etc., usually called machine process parameters [8]. Typically, from each vibration record, a set of diagnostic indicators is calculated known as trends. Each trend point is a combination of representation of true machine technical condition and behaviour, machines current operating point, measurement error and random factor. In a typical condition monitoring set up, each trend is tracked against a precalculated threshold value. In this case, operational states (shortly called states) are used for data classification during the data acquisition process. On the basis of these states, data is combined into sets, which are assumed to represent a particular machine. Consequently, the overall number of defined diagnostic indicators and estimators is equal to the number of indicators and estimators multiplied by the number of states. Therefore, from operator point of view, it is desirable to have as little states as possible. On the other hand, from reliable-diagnostics point of view, in order to minimize the fluctuation of machines operating points, it is desirable to define ranges of states as low as possible. In this case, the state configuration would result either in (i) single operational state with low permissible fluctuation of operational parameters, (ii) a large number of operational states with low permissible fluctuations of operational parameters.

3. CLASSIFICATION PROBLEM OF WIND TURBINE VIBRATION SIGNALS AND OPERATIONAL STATES

In recent years large development of monitoring and diagnostic technologies for WTs has taken place. The growing number of installed systems created the need for analysis of gigabytes of data created every day by these systems. Apart from the development of several advanced diagnostic methods for this type of machinery there is a need for a group of methods, which will act as an "early warning". The idea of this approach could be based on a data driven algorithm, which would decide on a similarity of current data to the data, which are already known. In other words, the data from

the turbine should be accounted for one of known states. If this is a state describing a failure, the human expert should be alarmed. If this is an unknown state, the expert should be informed about the situation and asked for a definition of such a new state.

This approach could be called "the blunt expert", which maybe sounds strange, but gives the most important feature of the proposed method. This approach may break the biggest barrier of application of artificial neural networks (ANNs) in diagnostics, which is availability of significant amount of training data. As in real cases it is not possible to acquire it, it is only possible to train ANNs for a few cases covered by available data.

The problem of classification was investigated by several authors. One of the first works was research by Shuhui et al. [15], who compared classification techniques for the wind curve estimation. This work was often referenced by others, but from the ANN point of view it only multilayered feed-forward types of networks. Another important contribution was given by Kim [10], who compared performance of several classification methods. His experiments showed that unless the number of independent variables in the system is low, ANNs perform better than other methods. Again, the investigated network was the multi-layer feed-forward network trained by the back-propagation algorithm.

There are no works, known to us, which would consider application of ART networks for the classification of WT states. There were also works applying wind turbines for wind and power generation prediction, but this issue is outside the scope of this paper.

As the ART networks are capable to perform efficient classification and to recognize new states when necessary [5, 6], we performed research of initial classification task. The goal of the experiment was verification of ART classification capabilities with comparison to the human expert. This type of data is acquired in the majority of cases and the successful classifier should create a reasonable number of classes, similar to these by a human expert. This task is the main goal of the following paper.

As such a classification was shown, it is thus possible to filter out states, which are known to be correct.

The expert can then focus only on “suspicious” states returned by the algorithm.

4. CHARACTERISTICS OF THE ART-2 NEURAL NETWORKS

Let us briefly recall ART-2 neural network properties [3, 6, 14]. The ART-2 is an unsupervised neural network based on adaptive resonance theory (ART). A typical ART-2 architecture, introduced by Carpenter and Grossberg [5, 6], is presented in Fig.2 (only one unit of each type is shown here). In the attentional sub-system, an input pattern s is first presented to the F_1 layer, which consists of six kinds of units - the W, X, U, V, P and Q cells. It then undergoes a process of activation, including normalization, noise suppression and updating. This results in an output pattern p from the F_1 layer. Responding to this output pattern, an activation is produced across F_2 layer through bottom-up weights b_{ij} . As the F_2 layer is a competitive layer with a winner-takes-all mode, only one stored pattern is a winner. It also represents the best matching pattern for the input pattern at the F_1 layer. Furthermore, the pattern of activation on the F_2 layer brings about an output pattern that is sent back to the F_1 layer via top-down weights t_{ji} . For the orienting sub-system, it contains a reset mechanism R and a vigilance parameter q to check for the similarity between the output pattern from the F_2 layer and the original input pattern from the F_1 layer. If both patterns are concordant, the neural network enters a resonant state where the adaptation of the stored pattern is conducted. Otherwise, the neural network will assign an uncommitted (inhibitory) node on the F_2 layer for this input pattern, and thereafter, learn and transform it into a new stored pattern.

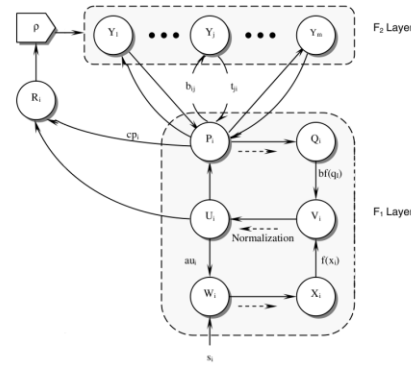


Fig. 2 ART-2 architecture

5. RESULTS

A simulation of a wind turbine work using historical data has been done. Changes of operational states and vibration signals were investigated. Historical data contain 27000 measuring points in time (sampling frequency is 1 per 15 minutes). Each point has three operational states values and one vibration signal value. Simulation step was taken every 1000 measuring points. ART-2 network (described in section 4) was used in the simulation in a following way.

1. ART-2 network is initialized.
2. Time t as a pointer of measuring point is set to 1000.
3. All measuring points' values are scaled to $[0, 1]$.
4. While t is not greater than 27000
 - a. ART-2 learning process is performed for each measuring point in $[1, t]$. The order of points is randomized. Each point is taken once. The vigilance parameter is set to 0.982.
 - b. Figures of classification states are plotted. Each network pattern determines some state of machine.

Figure 3 presents how the ART-2 network has classified states for first 5000 measuring points. There were 3 dominate states. After 15000 measuring points 4-th dominate state has joined. That situation is presented on figure 4. At the end classification states look like in the figure 5.

Table 1 describes how numbers of classified states were changing during simulation process.

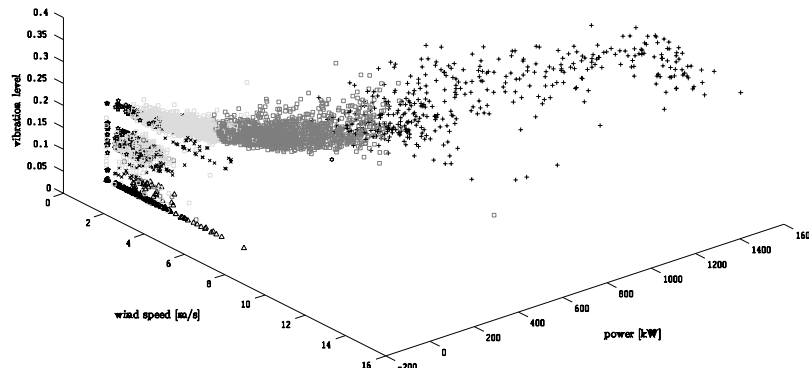


Fig. 3 The operational states (wind, power) and vibration signal classified using ART-2 network using 5000 measuring points.

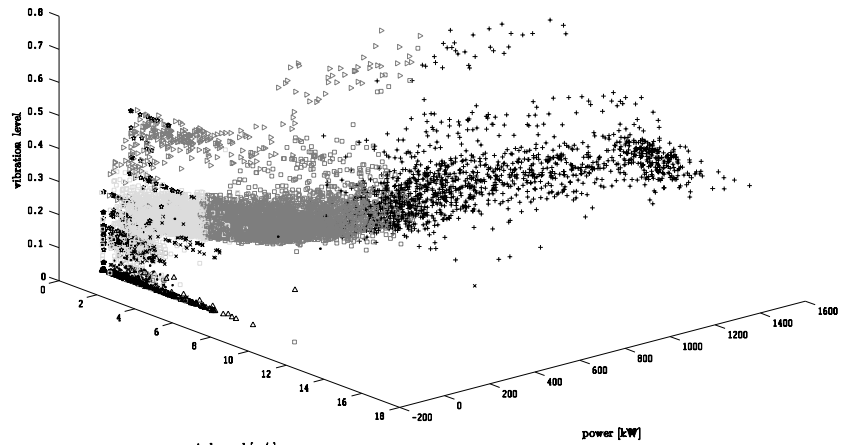


Fig. 4 The operational states (wind, power) and vibration signal classified using ART-2 network using 15000 measuring points.

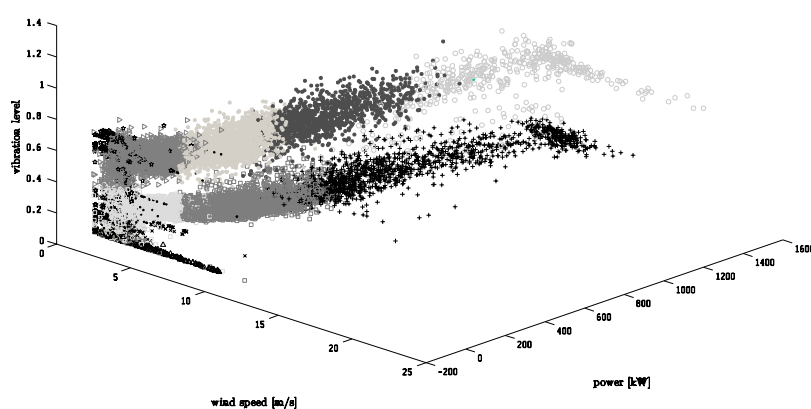


Fig. 5 The operational states (wind, power) and vibration signal classified using ART-2 network using 27000 measuring points.

Table 1 Details of simulation steps. Column 1 (Details) - number of processed measuring points. Column 2 - number of detected states. Values in column 3-17 represent numbers of measuring point which were classified as a specified state. Last column - number of states with value greater than 10.

Distance	States	#1	#2	#3	#4	#5	#6	#7	#8	#9	#10	#11	#12	#13	#14	#15	#>10
1000	5	677	91	185	18	29											5
2000	6	1354	131	380	33	98	4										5
3000	6	2033	144	602	70	147	4										5
4000	7	2560	184	751	119	366	9	11									6
5000	7	2170	210	1656	208	447	10	299									6
6000	8	2269	238	2348	217	505	7	412	4								6
7000	8	2590	257	2776	234	595	7	535	6								6
8000	8	3106	252	3018	233	620	9	755	7								6
9000	8	3531	281	3250	264	725	12	922	15								8
10000	9	4008	256	3702	256	666	113	977	20	2							8
11000	10	4362	240	4099	248	486	473	1053	24	14	1						9
12000	11	4594	247	4551	292	537	593	1137	32	14	1	2					9
13000	11	4938	256	4964	292	619	624	1249	39	14	2	3					9
14000	11	5116	273	5369	293	801	776	1303	44	14	4	7					9
15000	11	5418	277	5283	314	1129	858	1345	59	14	7	296					10
16000	11	5425	280	5296	384	1211	972	1358	129	14	10	921					10
17000	12	5515	260	5276	339	1217	1336	1317	269	12	23	1433	3				11
18000	12	5574	261	5287	344	1237	1346	1350	274	12	28	2283	4				11
19000	12	5635	279	5244	354	1328	1475	1353	273	12	35	3006	6				11
20000	12	5633	292	5268	386	1440	1573	1350	291	12	46	3700	9				11
21000	13	5520	298	5282	399	1443	1610	1349	288	13	91	3895	801	11			13
22000	14	5299	291	5412	408	1432	1561	1336	291	12	174	29772306	497	4			13
23000	14	5151	302	5515	484	1499	1643	1385	315	12	182	34162546	545	5			13
24000	14	5228	314	5471	481	1499	1681	1365	331	12	200	37812979	653	5			13
25000	14	5233	323	5499	511	1547	1717	1350	337	12	217	42833262	700	9			13
25000	14	5226	343	5512	578	1638	1782	1349	340	12	223	47183554	710	15			14
27000	15	5177	346	5524	572	1636	1791	1394	341	13	229	52313737	882	30	97		15

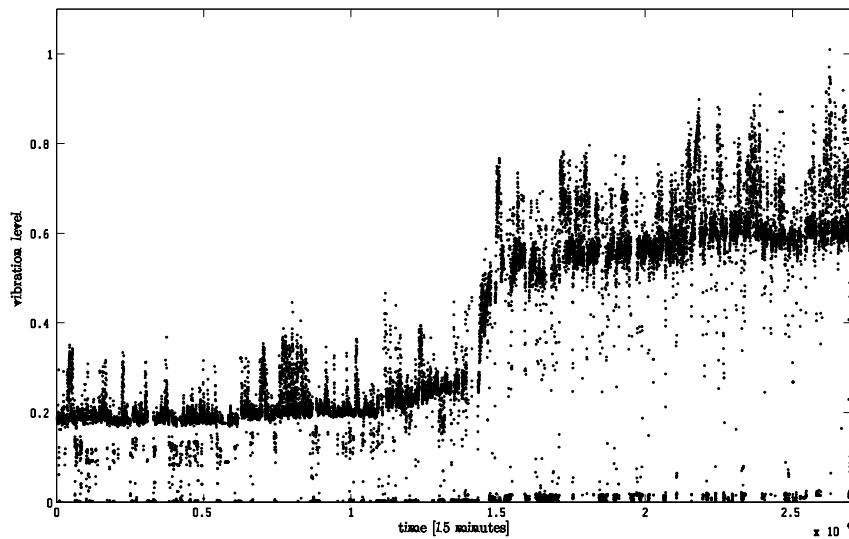


Fig. 4 Vibration signals for all measuring points.

Looking at last the column there can be observed first changes of numbers of states. First change has happened after 8000 measuring points. Next ones after 10000 and after 14000 points. Figure 6 presents the vibration signals for all measuring points (ordered by time). After about 14000 points the biggest damage happened. There must have been some symptoms of that damage. Mentioned two first changes could be candidates of those symptoms.

6. CONCLUDING REMARKS

As it has been mentioned, monitoring is crucial in wind turbines exploitation. On the other hand, there are very few attempts to create system for intelligent monitoring based on artificial intelligence - see [7] and references given there. The experiments described in this paper show that ART ANNs can be effective tool for such task performing - the symptoms of a turbine damage can be detected using ART ANN. It should be stressed however, that the obtained results are preliminary ones - only one vibration channel has been used whereas, usually, a few vibration channels are observed simultaneously - see [2]. The monitoring module based on ANNs is planned to be a module of expert system for intelligent monitoring and fault diagnostics in wind turbines.

7. ACKNOWLEDGEMENTS

The paper was supported by the Polish Ministry of Science and Higher Education under Grant No. N504 147838.

REFERENCES

1. Barszcz T., Bielecki A., Romaniuk T. (2009) *Application of probabilistic neural networks for detection of mechanical faults in electric motors*. Electrical Review 8/2009, 37-41.
2. Barszcz T., Bielecka M., Bielecki A., Wójcik M. (2012) *Wind speed modeling using Weierstrass function fitted by a genetic algorithm*. Journal of Wind Engineering and Industrial Aerodynamics 109, 68-78.
3. Barszcz T., Bielecki A., Wójcik M. (2012) *ART-type artificial neural networks applications for classification of operational states in wind turbines*. Lecture Notes in Artificial Intelligence 6114, 11-18
4. Barszcz T., Randall R. B. (2009) *Application of spectral kurtosis for detection of a tooth crack in the planetary gear of a wind turbine*. Mechanical Systems and Signal Processing 23, 1352-1365.
5. Carpenter G. A., Grossberg S. (1987) *A massively parallel architecture for a self-organizing neural pattern recognition machine*. Computer Vision, Graphics, and Image Processing 37, 54-115.
6. Carpenter G. A., Grossberg S. (1987) *ART2: self-organization of stable category recognition codes for analog input pattern*. Applied Optics 26, 4919-4930.
7. Hameeda Z., Honga Y. S., Choa T. M., Ahnb S. H., Son C. K. (2009) *Condition monitoring and fault detection of wind turbines and related algorithms: A review*, Renewable and Sustainable Energy Reviews, 13, 1-39.
8. Jabłoński A., Barszcz T. (2012) *Procedure for data acquisition for machinery working under non-stationary operational conditions*, The Ninth International Conference on Condition Monitoring and Machinery Failure Prevention Technologies, 12-14 June 2012, London.
9. Jabłoński A., Barszcz T., Bielecka M. (2011) *Automatic validation of vibration signals in wind farm distributed monitoring systems*, Measurement, vol.44, 1954-1967.
10. Kim Y. S., *Performance evaluation for classification methods: A comparative simulation study*.
11. Korbić J., Obuchowicz A., Uciński D. (1994) *Artificial Neural Networks. Foundations and Applications*. Academic Press PLJ, Warsaw (in Polish).

12. Kusiak A., Li W. (2011) *The prediction and diagnosis of wind turbine faults*, Renewable Energy, vol.36, 2011, 16-23.
13. Rutkowski L. (1996) *Neural Networks and Neuro-computers*. Technical University in Cze,stochowa Press, Częstochowa (in Polish).
14. Shieh M. D., Yan W., Chen C. H. (2008) *Soliciting customer requirements for product redesign based on picture sorts and ART2 neural network*. Expert Systems with Applications 34, 194-204.
15. Shuhui L., Wunsch D. C., O'Hair E., Giesselmann M.G. (2001) *Comparative analysis of regression and artificial neural network models for wind turbine power curve estimation*, Journal of Solar Energy Engineering 123, 327-332.
16. Tadeusiewicz R. (1993) *Neural Networks*. Academic Press, Warsaw (in Polish).

EFFECTIVENESS OF THE SPATIAL ACCELERATION MODULUS FOR ROLLING ELEMENTS BEARING FAULT DETECTION

Michele COTOGNO¹, Marco COCCONCELLI², Riccardo RUBINI³

¹University of Modena and Reggio Emilia, Department of Science and Engineering Methods, Via Amendola,
 2 – Morselli Building, 42122 Reggio Emilia, Italy
michele.cotogno@gmail.com

²University of Modena and Reggio Emilia, Department of Science and Engineering Methods, Via Amendola,
 2 – Morselli Building, 42122 Reggio Emilia, Italy
marco.cocconcelli@unimore.it

³University of Modena and Reggio Emilia, Department of Science and Engineering Methods, Via Amendola,
 2 – Morselli Building, 42122 Reggio Emilia, Italy
riccardo.rubini@unimore.it

Summary

Rolling Elements Bearing (REB) condition monitoring is mainly based on the analysis of acceleration (vibration) signal in the load direction. This is one of the three components of the acceleration vector in 3D space: the main idea of this paper is the recovery of additional fault information from the other two acceleration vector components by combining them to obtain the modulus of the spatial acceleration (SAM) vector. The REB diagnostic performances of the SAM are investigated and compared to the load direction of vibration by means a rough estimator of the “Signal-to-Noise” Ratio and the Spectral Kurtosis. The SAM provides a higher SNR than the single load direction. Finally, Spectral Kurtosis driven Envelope analysis is performed for further comparison of the two signals: its results highlight that demodulation of the SAM isn’t strictly necessary to extract the fault features, which are already available in the raw signal spectrum.

Keywords: Rolling Element Bearing, Diagnostic, Spatial Acceleration Modulus, SAM, SNR, Spectral Kurtosis, Envelope Analysis.

1 Introduction

Rolling Elements Bearing (REB) condition monitoring is mostly based on the analysis of the vibration signal [1,2]. This is typically obtained from an accelerometer which measures the intensity of vibration (i.e.: acceleration) along the load direction. Many signal processing techniques are available for the REB fault features extraction: they mainly deal with the fact that the measured vibration signal is the sum of different components (mechanical/electrical noise, the effect of vibration path from the REB to the sensor, vibrations coming from other moving parts in the machinery, etc.) which mask the fault signature. Additional fault information may be recovered from all the three acceleration

components by analyzing the modulus of the spatial acceleration vector (SAM, [9]). In particular, it is supposed that one effect of the vibration path could be the spread of the signal of interest along other axes of acceleration rather than preserving it in the load direction only. Indeed, a faulty bearing produces a series of vibration pulses that excite all the vibration modes of the system, including the transversal modes (with respect to the load direction): thus traces of this pulse series could also be embedded in vibration data along the non-load directions. The SAM should embody this extra information, and it’s obtained for every instant t by the following Eq. 1:

$$SAM(t) = \sqrt{(x(t) - \mu_x)^2 + (y(t) - \mu_y)^2 + (z(t) - \mu_z)^2} \quad (1)$$

where $x(t)$, $y(t)$ and $z(t)$ are the acceleration vector projections acquired by the triaxial accelerometer at time t , and μ_x , μ_y and μ_z are the temporal averages of the respective axis. In this paper the SAM is compared with the acceleration signal along the load axis (i.e.: the classically analyzed signal in REB condition monitoring) in case of loaded and unloaded bearing, healthy and faulty bearing. Equation 1 highlights that the SAM will exhibit larger (and non-negative) values than any single axis of acceleration, and this consideration can be extended

also to the respective amplitude spectra. Consequently, a direct quantitative comparison between the SAM and any single acceleration axis (and between their spectra) can’t be completely truthful. In order to overcome this issue, some attempts of estimation of the Signal-to-Noise Ratio (SNR) are performed on real REB data and reported in the next sections.

2 SNR estimation: unloaded bearing

The bearing used in this series of experiments is SKF1205ETN9. The data are recorded at 25 kHz sampling frequency by a PCB356A01 triaxial accelerometer, from healthy and faulty bearing at five different bearing rotation speed ($f_r = 15, 25, 35, 45$ and 60 Hz). The artificial fault is made on the outer race. The only load applied is weight, directed along the y axis of the accelerometer: this axis of

vibration is the classically analyzed in REB condition monitoring and is therefore used for performance comparison with the SAM. The analysis is performed on the raw data in order to evaluate the amount of information spontaneously embodied in the signals. In Fig. 1a (healthy bearing) and Fig. 1b (faulty bearing) extracts of the vibration data along the load axis are reported and compared to the correspondent time sections of the SAM (Fig. 1c – 1d).

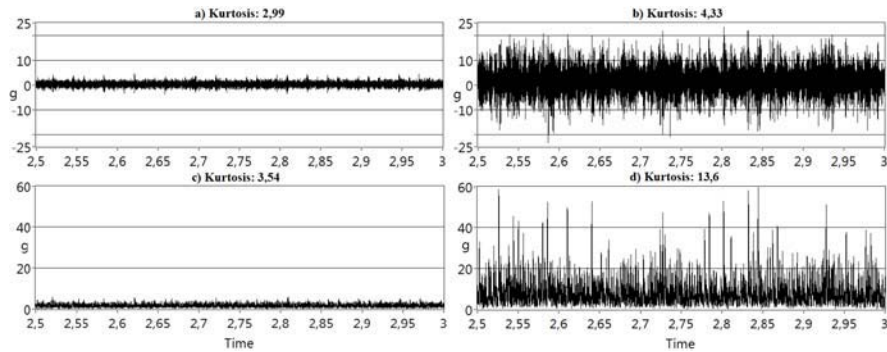


Fig. 1. Time sections of vibration data: a) load axis, healthy bearing; b) load axis, faulty bearing; c) SAM, healthy bearing; d) SAM, faulty bearing

Figure 1 confirms that the amplitude of the signal is larger for the SAM. Moreover, it seems to have a more “spiky” nature than the load axis, particularly in presence of a fault (Fig. 1d): this obser-

vation is acknowledged by the global Kurtosis index (4,33 for the load axis and 13,6 for the SAM in case of faulty bearing); i.e., the SAM is representing the pulses of vibration in a clearer manner.

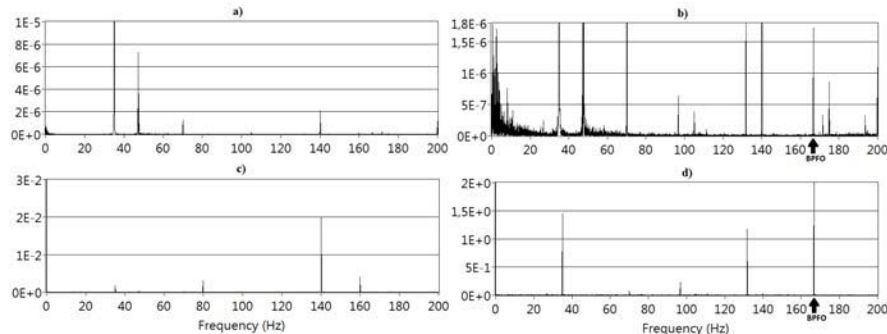


Fig. 2. Autospectra of: a) load axis, healthy bearing; b) load axis, faulty bearing; c) SAM, healthy bearing; d) SAM, faulty bearing. ($f_r = 35\text{Hz}$, BPFO = 167Hz). The Y scales are different in order to highlight the amplitudes of interest more clearly

In Figure 2 the autospectra of the load axis and the SAM are reported in case of healthy bearing (resp. Fig. 2a and 2c) and in case of outer race fault (resp. Fig 2b and 2d): in these cases the bearing ro-

tation speed (f_r) is 35Hz giving a theoretical Ball Pass Frequency on Outer Race (BPFO) of 167Hz. Figure 3 is equivalent to Figure 2 except for f_r of 45Hz (theoretical BPFO of 214,7Hz).

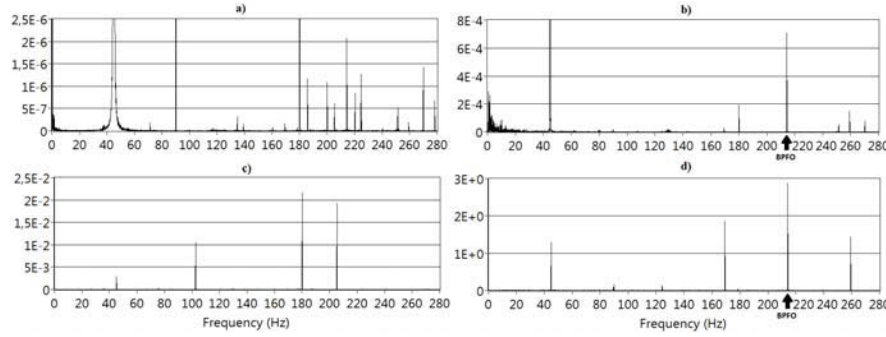


Fig. 3. Autospectra of a) load axis, healthy bearing; b) load axis, faulty bearing; c) SAM, healthy bearing; d) SAM, faulty bearing. ($f_r = 45\text{Hz}$, $\text{BPFO} = 214,7\text{Hz}$). The Y scales are different in order to highlight the amplitudes of interest more clearly

As expected, the SAM spectrum is higher (usually 3 order of magnitude) than the load axis spectrum, thus hindering a direct spectra comparison. There are slight differences in the frequency position of the main spectrum peaks, probably because of the extra information gathered from the additional axes of vibration. In general, for the SAM the authors observe a “cleaner” and more communicative spectrum, in particular in case of a healthy bearing. In case of faulty bearing the SAM spectrum is dominated by the BPFO line, while the same isn’t for the load axis spectrum (e.g.: Fig. 2). In order to perform a more meaningful comparison between the two signals, the “Signal-to-Noise” Ratio (SNR) is approximated by the SNR_A estimator (Eq. 2): SNR_A comes from the pragmatic definition of “signal” as the power in the $\text{BPFO} \pm 1\%$ frequency band and “noise” as the mean spectrum power. The SAM exhibits higher SNR_A than the load axis in all the ex-

periments conducted (Table 1). The SAM SNR_A increases when the fault is introduced except in case of high speeds (45 and 60Hz), where it decreases; this behavior is almost the exact opposite of the load axis SNR_A (which exhibits also larger variations). This could be explained by the larger energetic content of the vibration signals at higher speeds which increases the denominator in Eq. 2, thus lowering the SAM SNR_A indicator; in contrast, the load axis SNR_A increases probably because at higher speeds its BPFO line shows a larger amplitude (Fig. 3b with respect to Fig. 2b) thus increasing the numerator in Eq. 2. The sum of these two effects and the slightly different nature of the two signals could explain the SNR_A trends highlighted in Table 1. SNR_A values are interpreted by the authors as a symptom of the SAM actually embodying more information or making it more readable than the load axis.

$$SNR_A = \frac{\text{power in the } \text{BPFO} \pm 1\% \text{ frequency band}}{\text{mean spectrum power}} \quad (2)$$

Table 1. Estimates of the Signal-to-Noise Ratio.

f_r (Hz)	Signal	SNR_A (dB)	
		Healthy bearing	Faulty bearing
15	Load axis	8,9	0,4
	SAM	49,7	51,4
25	Load axis	-9,7	-12,2
	SAM	38,2	43,9
35	Load axis	-9,8	-18,5
	SAM	40,8	41,7
45	Load axis	1,4	-13,5
	SAM	43,9	40,8
60	Load axis	0,8	2,5
	SAM	43,7	34,1

A more refined way to estimate the SNR is represented by the Spectral Kurtosis (SK) [3,4], a useful tool in condition monitoring [5] that can be used in REB diagnostics to find the optimum frequency

$$W(f) = \frac{1}{1 + \rho(f)} \quad (3)$$

where $\rho(f)$ is the “Noise-to-Signal” Ratio, i.e. the inverse of the SNR. “Signal” here is interpreted as

band for the signal filtering prior to the Envelope analysis [2,6,7]. In [4] it is revealed that the SK is proportional to the square of the Wiener filter $W(f)$, which is defined by the following Eq. 3:

“randomly occurring pulses of random amplitude” [4] which is a model that has proven its effective-

ness in describing the vibration signal of a faulty REB. Thus, larger SK values are related to larger SNR of the data. In this paper, the SK is obtained

$$SK(f) = \frac{M}{M-1} \left[\frac{(M+1) \sum_{i=1}^M |X_i(f)|^4}{\left(\sum_{i=1}^M |X_i(f)|^2 \right)^2} - 2 \right] \quad (4)$$

where M is the number of non-overlapping blocks of the STFT and $X_i(f)$ is the DFT of the i^{th} block of data. As highlighted in [4], the STFT block length (i.e.: the STFT window length, N_w in the rest of this paper) must be set to have a temporal duration lower than the expected mean time between impacts

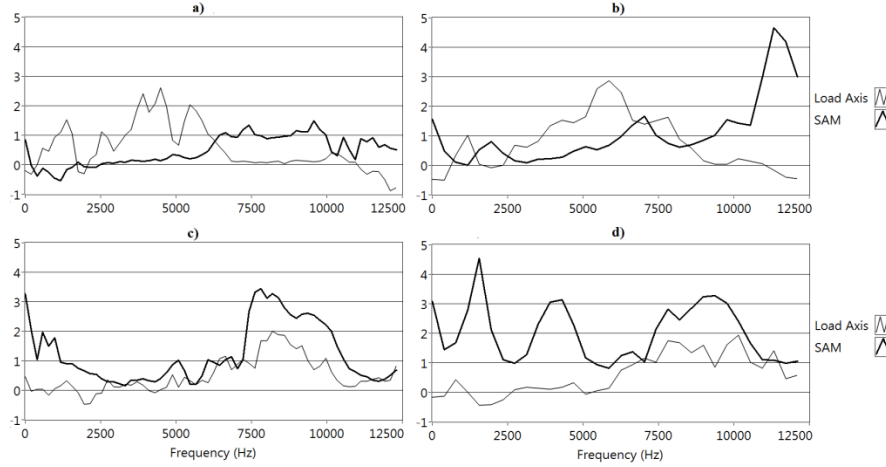


Fig. 4. Spectral Kurtosis of load axis and SAM; a) healthy bearing, $f_r = 35\text{Hz}$; b) healthy bearing, $f_r = 45\text{Hz}$; c) faulty bearing, $f_r = 35\text{Hz}$; d) faulty bearing, $f_r = 45\text{Hz}$

Fig. 4 shows that in case of healthy bearing (Fig. 4a and 4b) the SK of the SAM is lower (and closer to zero) than the SK of the load axis, and it increases more decisively when a fault is present (Fig. 4c and 4d, where the SAM SK graph is always over the load axis SK). In absence of the fault, the SAM SK overcomes the load axis SK in the $6,5 \div 12,5\text{kHz}$ (when $f_r = 35\text{Hz}$, Fig. 4a) and in the $8 \div 12,5\text{kHz}$ (when $f_r = 45\text{Hz}$, Fig. 4b) frequency bands. Zero-valued SK indicates that the signal is more similar to Gaussian noise rather than a series of transients, while the presence of the latter is highlighted by higher SK values: thus, the SAM SK is communicating more explicitly the existence of a fault. The frequency bands with higher Kurtosis indicated by the two SK are similar when the fault is present, and correspond to a system resonance band (approximately $7,5 \div 9,5\text{kHz}$). It's notable that in the majority of the experiments the SAM SK exhibits the highest values also in the low frequency zone (i.e.: near the DC component), thus communicating that demodulation isn't strictly necessary to extract the fault signature from the SAM. This is in accord with the raw signals spectra comparison (Fig. 2, Fig. 3 and Table 1). These considerations about the SAM SK seem to confirm the higher SNR of the SAM than the load axis in case of unloaded bear-

by the following formula (Eq. 4), which is an unbiased STFT-based SK estimator proposed in [8]:

(i.e.: BPFO) in order to get consistent results: this yields $N_w = 128$ samples in case BPFO = 167Hz and $N_w = 64$ samples in case BPFO = $214,7\text{Hz}$. In Figure 4 the SK for these two experiments are reported.

ing: in the next section the same study is performed and reported in case of loaded bearings.

3 SNR estimation: loaded bearing

In this series of experiments two damaged bearings had been used, these being a very worn SKF1205ETN9 and a KBC6205Z, both with an artificial outer race fault: the goal of this test was to investigate if the SAM performances are caused by the absence of a load applied to the REB. Indeed, the acquisition chain remained the same of the previous series of experiments (including the sampling frequency of 25kHz) but in this case two different radial loads of 589 N and 1178 N had been applied to the bearings; the REB speeds in this series of tests were $15, 25, 35, 45$, and 53Hz . In Fig. 5 (SKF running at $f_r = 35\text{Hz}$ – load 589 N) and Fig. 6 (KBC running at $f_r = 25\text{Hz}$ – load 1178 N) the raw spectra of the load axis and the SAM are reported: also in case of loaded bearing, it can be observed that the SAM spectrum is much more “clean” and it's dominated by the BPFO, in contrast with the load axis spectrum where the BPFO is almost hidden. Generally, the features of the two spectra are those already observed in the previous section, thus indicating that the SAM appears very significant and communicative from the diagnostic point of view.

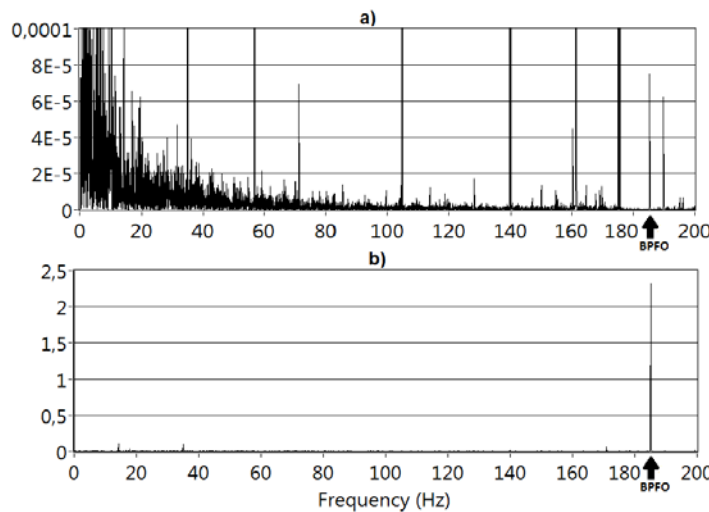


Fig. 5. Autospectra of a) load axis and b) SAM of the faulty SKF bearing running at $f_r = 35\text{Hz}$ ($\text{BPFO} = 183,9 \text{ Hz}$) with 589 N of load applied.

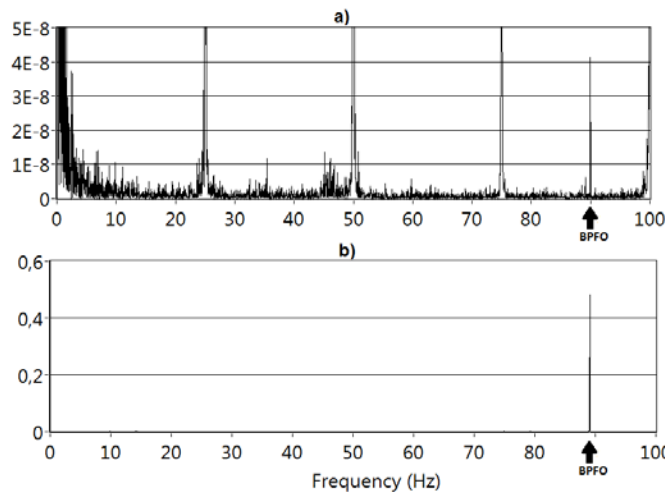


Fig. 6. Autospectra of a) load axis and b) SAM of the faulty KBC bearing running at $f_r = 25\text{Hz}$ ($\text{BPFO} = 89,6 \text{ Hz}$) with 1178 N of load applied

The values of SNR_A and SNR_{CF} are reported in Table 2 and Table 3 (respectively: SKF and KBC bearing): these are calculated again from the raw vibration signals in order to evaluate their native information content.

Table 2. Values of SNR_A for radial loaded SKF1205ETN9 bearing.

f_r (Hz)	Signal	SNR_A (dB)	
		load 589 N	load 1178 N
15	Load axis	-14,98	3,77
	SAM	40,29	37,13
25	Load axis	1,26	-8,49
	SAM	37,62	35,59
35	Load axis	-6,94	-9,30
	SAM	36,64	34,48
45	Load axis	5,98	-4,80
	SAM	34,89	33,60
53	Load axis	17,81	10,56
	SAM	33,77	33,30

Table 3. Values of SNR_A for radial loaded KBC6205Z bearing.

f_r (Hz)	Signal	SNR_A (dB)	
		load 589 N	load 1178 N
15	Load axis	-1,28	-11,88
	SAM	41,72	44,48
25	Load axis	-6,72	-11,66
	SAM	43,17	46,90
35	Load axis	7,85	-0,81
	SAM	24,32	44,40
45	Load axis	10,72	15,39
	SAM	20,10	19,93
53	Load axis	5,98	-1,68
	SAM	23,52	31,88

From Tables 2 and 3 it can be seen that the SAM exhibit higher SNR also in case of loaded bearings in all the trials. These SNR approximations confirm the observations made on the direct comparison of the spectra: the SAM represent the frequencies of

interest more clearly than the load axis also in case of loaded bearing. The Spectral Kurtosis of the two signals is reported in Fig. 7 in case of KBC bearing running at $f_r = 25\text{Hz}$ under 1178 N of radial load. The SK of the SAM reaches its maximum at frequencies lower than the load axis SK, and the maximum value is greater for the SAM. Thus the SK indicates a better SNR for the SAM, but the differ-

ence between the SK of the two signals is less evident than in case of unloaded bearing (Fig. 4). This behavior of the SK is shared by the majority of the trials concerning loaded bearings, thus it suggests that it isn't necessary to demodulate the SAM to obtain diagnostic information of the bearing – an observation concordant with the direct spectra comparison and the SNR_A values.

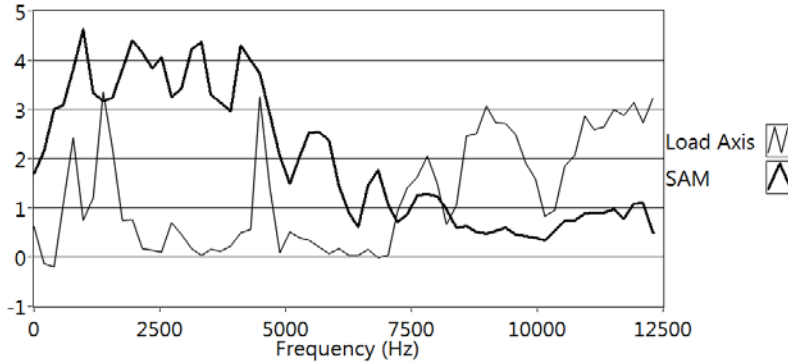


Fig. 7. Spectral Kurtosis of load axis and SAM; KBC bearing, $f_r = 25\text{Hz}$, load is 1178 N

4 Envelope Analysis

Envelope Analysis [1,2,7] is the benchmark signal processing tool for REB diagnostics. It performs a demodulation of the bandpass filtered signal. In this paper the filtering band is selected as the band in which the Spectral Kurtosis is maximized. The selected bands for the unloaded SKF bearing in

case of $f_r = 35\text{Hz}$ are $7,7 \div 8,8\text{kHz}$ for the load axis and $7,5 \div 8,5\text{kHz}$ for the SAM; in case of $f_r = 45\text{Hz}$ they are $9,5 \div 10,5\text{kHz}$ for the load axis and $900 \div 1900\text{Hz}$ for the SAM. In Fig. 8 the Envelope spectra of the load axis and SAM are reported for the case of faulty unloaded SKF bearing rotating at $f_r = 35\text{Hz}$.

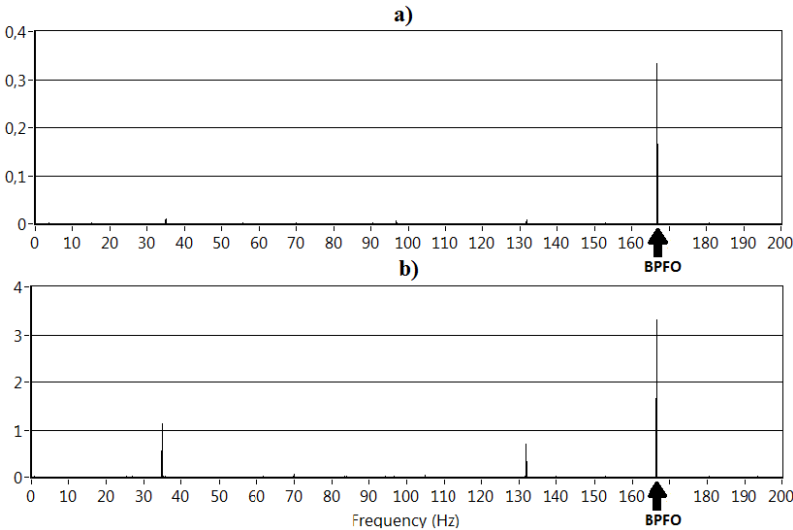


Fig. 8. Envelope Spectra of a) load axis and b) SAM for the unloaded SKF1205ETN9 bearing ($f_r = 35\text{Hz}$, BPFO = 167Hz)

It can be seen that the Envelope spectra of the SAM exhibit larger values, highlighting almost the same frequencies of the load axis. The dominating frequencies is the BPFO (167Hz) for both signals, but other notable frequencies (e.g.: the $f_r = 35\text{Hz}$ frequency) exhibit higher magnitude in the SAM Envelope spectrum. This is about one order of magnitude higher than the load axis at those frequencies, while the average difference between the autospectra of the two signals is about 3 orders of

magnitude (these considerations are valid for all the experiments). The BPFO magnitude in the SAM Envelope spectrum is about two times the correspondent magnitude in the raw SAM spectrum (respectively, 3,1 and 1,7); in contrast, the BPFO magnitude of the load axis Envelope spectra is about one million times the correspondent magnitude in the raw spectra (respectively, 0,3 and $1,75 \cdot 10^{-6}$).

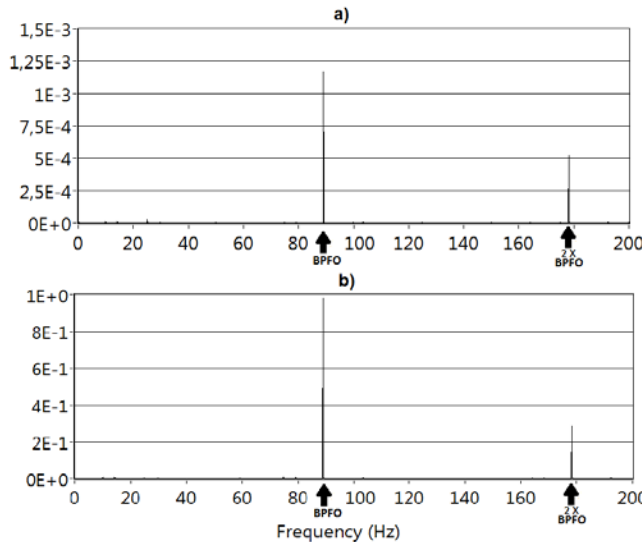


Fig. 9. Envelope Spectra of a) load axis and b) SAM for the KBC6205Z bearing (radial load of 1178 N, $f_r = 25\text{Hz}$, BPFO = 89.6 Hz)

In Fig. 9 the Envelope spectra of the SAM and load axis are reported in case of loaded KBC bearing running at $f_r = 25\text{Hz}$: the filtering band used for demodulation are $8.6 \div 9.6\text{ kHz}$ for the load axis and $0.6 \div 1.3\text{ kHz}$ for the SAM (i.e.: those with the maximum SK). The features of the Envelope spectra in case of loaded bearing are the same highlighted for the unloaded bearing: both spectra are dominated by the BPFO line but its amplitude is greater for the SAM. The demodulation permits to extract the information of interest from the load axis signal (its BPFO amplitude passes from $4.3 \cdot 10^{-8}$ to $1.16 \cdot 10^{-3}$, resp. Fig. 6a and Fig. 9a) while its action isn't so dramatic for the SAM (its BPFO amplitude passes from 0.5 to 1, resp. Fig. 6b and Fig. 9b), thus practically repeating the behavior highlighted in case of unloaded bearing. This observation confirms the indication of the Spectral Kurtosis of presence of high SNR in the low frequency zone of the SAM spectrum, signifying that demodulation isn't necessary for the SAM for the fault signature extraction.

5 Conclusions

In this paper the modulus of the spatial acceleration vector (SAM) is presented as a starting signal for rolling element bearings (REB) condition monitoring. Concerning the diagnostic capability, the SAM is compared to the acceleration component directed along the load axis, which is the classical analyzed signal in REB diagnostics. The comparison is performed on real raw REB data to evaluate the information spontaneously embedded in the signals: the data comes from two different bearings, encompassing the healthy and faulty, loaded and unloaded bearing conditions. Given the native amplitude difference between the two signals and their spectra (i.e., about three orders of magnitude), a rough approximation of the Signal-to-Noise Ratio

is used to compare them - SNR_A - which indicates always a higher SNR for the SAM. This is confirmed also by the Spectral Kurtosis (SK) analysis: higher SK is related to higher SNR and the SAM exhibit greater SK values in case of faulty bearing. Finally, Envelope analysis is performed and it also indicates a superior diagnostic capability of the SAM: its Envelope spectrum is generally one order of magnitude higher than the load axis Envelope spectrum. A comparison between the BPFO magnitude in the SAM Envelope spectrum and its correspondent in the raw SAM spectrum confirms that demodulation isn't necessary to extract the fault features, as indicated previously by the SK and the SNR_A estimator. The SAM thus appears as a valid starting signal for REB diagnostics: its spectrum is generally "cleaner" and more readable and the diagnostic information is already available without any signal processing.

6 Acknowledgments

The authors wish to thank the Inter Departmental Research Center INTERMECH MoRE of the University of Modena and Reggio Emilia for the financial support.

7 References

- [1] Randall RB, Antoni J (2011) *Rolling Element Bearing Diagnostics—A Tutorial*. Mechanical Systems and Signal Processing 25: 485–520
- [2] Randall RB (2011) *Vibration-based Condition Monitoring: Industrial, Automotive and Aerospace Applications*. John Wiley and Sons, West Sussex.
- [3] Antoni J (2006) *The spectral Kurtosis: a useful tool for characterizing non-stationary signals*. Mechanical Systems and Signal Processing 20: 282–307

- [4] Antoni J, Randall RB (2006) *The spectral Kurtosis: application to the vibratory surveillance and diagnostics of rotating machines.* Mechanical Systems and Signal Processing 20: 308–331
- [5] Barszcz T, Randall RB (2009) *Application of spectral Kurtosis for detection of a tooth crack in the planetary gear of a wind turbine.* Mechanical Systems and Signal Processing 23(4): 1352–1365
- [6] Cocconcelli M, Zimroz R, Rubini R, Bartelmus W (2012) *Kurtosis over Energy Distribution Approach for STFT Enhancement in Ball Bearing Diagnostics.* Proceedings of the Second International Conference "Condition Monitoring of Machinery in Non-Stationary Operations" CMMNO'2012 51-59
- [7] McFadden PD, Smith JD (1984) *Vibration monitoring of rolling element bearings by the high-frequency resonance technique - a review.* Tribology International 17(1): 3-10
- [8] Vrabie VD, Granjon P, Serviere C (2003) *Spectral Kurtosis: from definition to application.* IEEE-EURASIP Workshop on Nonlinear Signal and Image Processing, Grado, Italy, 2003, June 8–11.
- [9] Cotogno M, Cocconcelli M, Rubini R (2013) *Spatial acceleration modulus for rolling elements bearing.* Proceedings of the Third International Conference "Condition Monitoring of Machinery in Non-Stationary Operations" CMMNO'2013.

A NEW DATA MINING APPROACH FOR POWER PERFORMANCE VERIFICATION OF AN ON-SHORE WIND FARM

Francesco CASTELLANI*, Alberto GARINEI**, Ludovico TERZI***, Davide ASTOLFI*, Michele MORETTI*,
Andrea LOMBARDI***

* University of Perugia, Department of Industrial Engineering, Perugia, Italy

** DMII, Università degli Studi Guglielmo Marconi, Roma, 00193, Italy

*** Sorgenia Green srl, Via Viviani 12, Milano, 20124, Italy

Abstract

Monitoring wind energy production is fundamental to improve the performances of a wind farm during the operational phase. In order to perform reliable operational analysis, data mining of all available information spreading out from turbine control systems is required. In this work a SCADA (Supervisory Control And Data Acquisition) data analysis was performed on a small wind farm and new post-processing methods are proposed for condition monitoring of the aerogenerators. Indicators are defined to detect the malfunctioning of a wind turbine and to select meaningful data to investigate the causes of the anomalous behaviour of a turbine. The operating state database is used to collect information about the proper power production of a wind turbine and a number map has been codified for converting the performance analysis problem into a purely numerical one. Statistical analysis on the number map clearly helps in detecting operational anomalies, providing diagnosis for their reasons. The most operationally stressed turbines are systematically detected through the proposal of two Malfunctioning Indices. Results demonstrate that a proper selection of the SCADA data can be very useful to measure the real performances of a wind farm and thus to define optimal repair/replacement and preventive maintenance policies that play a major role in case of energy production.

Key words: wind energy, renewable energy, wind turbine performance, data mining, SCADA database, control systems, fault diagnosis, performance optimization, wind turbine power output

1. INTRODUCTION

The monitoring of wind energy production is fundamental during the operational phase of a wind farm. Usually numerical modelling and experimental campaigns are carried out for wind-resource assessment and power performance prediction of a wind farm prior the installation of the turbines. Even if many techniques were developed for this purpose, disagreement between the predicted and the real production of a wind farm is often remarkable. Thus it is necessary to analyse the operational conditions of a wind farm both to increase the reliability of the assessment techniques and to define optimal repair/replacement and preventive maintenance policies, that play a major role in case of energy production. The SCADA (Supervisory Control And Data Acquisition) system is able to generate and organize a very functional database that can be used to monitor the wind farm and thus to set the optimal configuration for the aerogenerators, in order to maximize the energy production. Starting from the first methods based on the fault detection and analysis, more refined techniques were developed for wind turbines performance assessment [1, 2] and for the prediction and diagnosis of wind turbine faults [3]. In [3] the SCADA data, collected on a 5 minute scale, are classified in four groups (wind parameters, energy conversion parameters, vibration

parameters, temperature parameters) and are crossed against a database of status codes, entering at given times, ranked in four categories of decreasing fault severity. The power curve is studied both from filtering operational anomalies directly from the SCADA measurements, or crosschecking with the status code database, and a model curve is obtained by training neural networks to interpolate the scattered points. Computational models are developed to predict with certain accuracy a single severe fault occurring one hour before the fault itself appears in the status code report.

In order to increase wind farm efficiency, wind farm power performance tests were defined [4] and wind turbine condition assessment has been performed through the analysis of the power curve [5, 6]: in particular in [7] a systematic analysis of three different operational curves (power curve, rotor curve, blade pitch curve) is set up from SCADA measurements. Reference curves are built, from a four year database, for each month independently by removing outliers due to anomalous behaviours: a multivariate outlier detection approach based on Mahanobis distance is used. Therefore skewness and kurtosis of the reference curves are computed and the performance monitoring is based by comparing these moments of the measured operational curves against the reference ones on a 2D-plot.

In [8] the wind control centre performances are analyzed globally and in particular the nature of SCADA analysis is depicted for its increasing role of cross-checking estimated power offer (from forecast) and actual one, measured from historical and meteorological data.

In [9, 10] wind turbine condition monitoring has been developed applying Adaptive Neuro-Fuzzy Interference Systems (ANFIS) to SCADA measurements. A three step strategy has been followed: firstly normal behaviour models are used, by training Neural Networks, in order to monitor and detect anomalies on the relevant SCADA data. Subsequently occurred anomalies are related to reported faults, and relations are obtained to implement a knowledge database used by the Fuzzy Interference System to output diagnosis. In the following Paper [11] the performance of four data mining approaches for the ANFIS methods are compared. The Artificial Neural Network approach is an extremely fertile field [12]: in particular in [13] SCADA data of a given turbine are used for training models for predicting behaviour at nearby turbines.

In [14] SCADA measurements are filtered for decorrelating them and subsequently statistical estimators of outliers related to anomalous behavior are built.

Modern wind turbines are equipped with a complex monitoring system, so SCADA can provide a very large dataset that requires the development of new post-processing methods. In the present work a SCADA dataset of a wind farm installed in southern Italy is analysed and new post-processing methods are proposed for the monitoring of the aerogenerators. The wind farm is composed of nine wind turbines with a rated power of 2 MW installed on an hillside area with quite gentle slopes. The most important turbine parameters are identified on the SCADA dataset and data mining is performed both for the performance analysis and for the understanding of the wind turbines behaviour during operations.

2. THE SCADA DATABASE ANALYSIS: THE STRUCTURE OF THE DATABASE

The SCADA database consists on a series of measurements (e.g. blade pitch, hub, gearbox, inlet temperature, active, reactive and apparent power and so on) performed on a 10 minute basis. For each parameter, minimum, maximum, average and standard deviation are recorded. Thus, for each turbine, around 140 data are recorded every 10 minutes. To understand the real operational conditions of the wind turbines, the analysis was focused on the machine parameters that could be strictly related to the turbine performances. Among the data available from the machine control systems, the following parameters were considered more

significant for the present study: active power output (kW), reactive power (kW), inlet temperature (C), nacelle position (°), blade pitch (°), rotor speed (rpm). Measurements from a met mast (wind speed and direction at hub height and hub minus radius) were also used on post-processing to complete the SCADA dataset analysis. Measured parameters were analysed considering also the control system status code report, that lists the incoming or phasing out of a status. The code report is divided in two groups of data: operating states, which are mutually exclusive, and status codes (error, warning, info and operating state), some of which can coexist at a given time. Thus the complete dataset is composed of the status code database, that is a read only database, and of the SCADA measurement database, that can be cut or modified with respect to appropriate status codes, to obtain a filtered database. The interactions between the databases are shown in Figure 1.

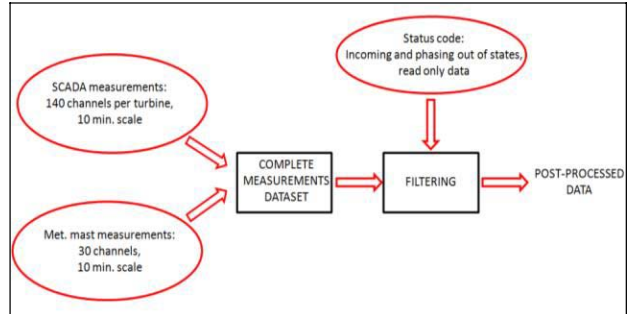


Fig. 1. The available dataset structure

3. THE SCADA DATABASE ANALYSIS: THE CONDITION MONITORING PROCEDURES

The first step of post-processing procedures was done developing routines to crosscheck and perform a series of controls on the acquired data. Because of the high level of IEC standards, the available data exceeds the typical data used for routine monitoring, so solid mathematical and computational tools are required. A first control was done considering the percentage in which each of the 9 turbines was in every operating state. The status code database coherence was checked summing these percentages and verifying that it was 100, being the operating states mutually exclusive. Then operating states statistics were obtained considering the status of each wind turbine. Considering the whole database (4 month of operational conditions), the Grid Operating State percentage is around 70 %, whereas 20 per cent of the time the turbines operating state is the automatic start-up, that follows a brake program. Depending on the brake program, the sequence of the other phases that follows the automatic start up may have a different length, but they are of short duration. The graph of Figure 2 highlights these states and, being a clear indicator of the power

availability of each wind turbine, it can be used to detect the malfunctioning of a wind turbine.

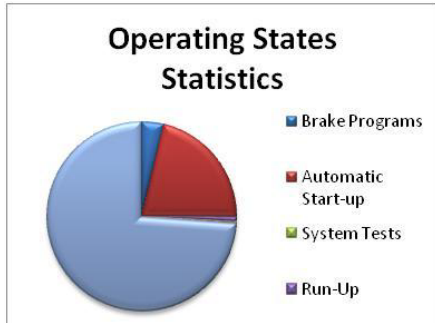


Fig. 2. Operating states statistics for a sample turbine

Then, for each operating state and status code, the average and standard deviation were calculated on a daily, weekly and monthly basis.

By analysing the operating states of the nine turbines, a malfunctioning was detected for wind turbine T53, as shown in Figure 3. This has been obtained by an automatic routine that computes mean and standard deviation on the whole turbine park of the percentages of each operating states: whereas significant deviations are met from the mean values, the statistics are performed on a shorter scale, weekly or even daily rather than monthly, in order to isolate the anomaly and thus cut a temporal window for which significant crosscheck with SCADA data can be done in order to investigate the causes of the anomaly.

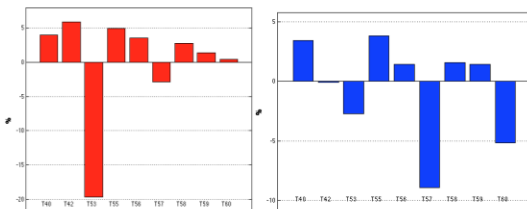


Fig. 3. Operating state 210 (Grid operation) and status code 0 (System OK) statistics: deviation in percentage of occurrence with respect to a reference turbine (T40)

A closer examination can be done by analysing the operating states for each status code. Even if a malfunctioning was detected by the operating states, the percentage of the status code system ok for turbine T53 is comparable with those of the other turbines, as shown in figure 3-b. This crosscheck between status codes, turbine operating states and SCADA data helps in pointing out the reasons of the anomaly, unveiling if the underproduction comes from environmental condition (strong or rapidly variable wind), or if it comes from network or electrical problems: actually Status Code System OK on indicates that the turbine is potentially in condition of producing power, but if the operating state is not power output production, the anomaly

must not come from the machine itself. It might be due, for example, to an electrical problem. Performing also a crosscheck and filtering of the SCADA data helps in verifying diagnosis hypothesis.

The Grid Operating State and thus the turbine availability was then analysed for each wind turbine on a weekly basis, as shown in Figure 4.

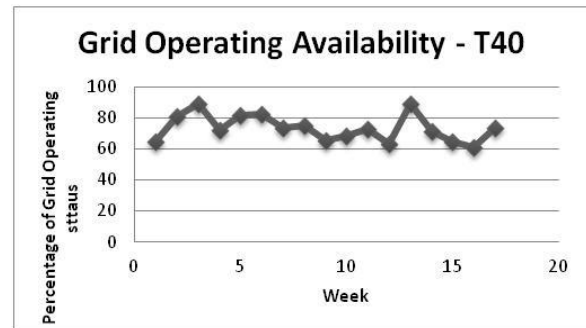


Fig. 4. Grid operating availability for turbine T40

Wind (direction and intensity) and temperature (the wind farm is located in an hot site) are the main parameters related to the operating availability of each wind turbine, so a similar behaviour for all the turbines was attended, but from graph in Figure 4 it is clear that the wind turbine T53 has a remarkable collapse in maximum power performance. This can be highlighted using the operating states statistics and analysing the duration of Run Up operating state, that is a phase between a brake program and the subsequent returning of power availability. From the following graph in Figure 5, the malfunctioning of wind turbine T53 can be easily detected.

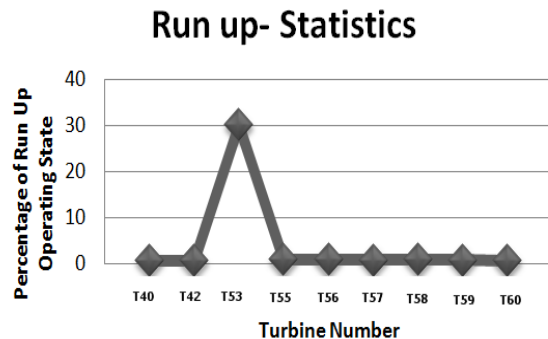


Fig. 5. 5 run-up statistics

Because this malfunctioning may be detected or not depending on the scale of observation (i.e. daily, weekly, monthly, global), this check can be used as an indicator to investigate the causes of the anomalous behaviour of a turbine in a certain period. This can be done by selecting the SCADA measurements corresponding to the Operating State Run Up active and analysing them in detail. This is a clear example of how the Status Code database can be used to select meaningful data from the measurement SCADA database.

The operating state database can also be used to collect information about the proper power production of a wind turbine. The theoretical available power curve (Betz limit) of a wind turbine is:

$$f(v) = \frac{16}{27} \frac{\pi}{8} \rho \cdot d^2 \cdot v^3 \quad (1)$$

Where ρ is the density and d is the rotor diameter. If we simply graph the active power measurements of a wind turbine (e.g. wind turbine T40) against the wind speed at the nacelle we obtain the first graph of the following Figure 6.

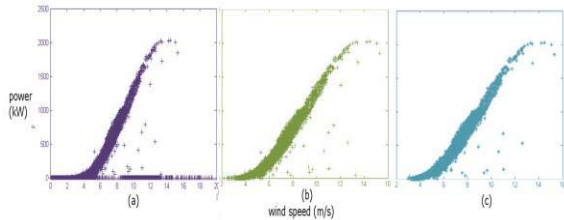


Fig. 6. unfiltered (a). filtered on power-speed product (b) and double filtered (c) power curve

A first operation can be the renormalization of the wind speed with the density factor, which is available from the SCADA data. Then, to filter these data, it is necessary to select the operating state significant for the proper power production. The output power can be curtailed due to rapidly changing winds, with the blade pitch angle being not fast enough to adjust to the wind direction, and might therefore not be due to a degradation of the wind turbine. A first condition to select significant data is that, for accepted data, the power-speed product is greater than 1. The filtered power curve is the (b) shown in Figure 6.

An interesting crosscheck can be done by analysing the data excluded by this filter considering the status code database, to inquire whether the turbine is in any problematic operating state, and considering the SCADA measurements.

Then, as a second step, only data acquired when the operating state of maximum power production was on were accepted (Figure 6-c).

Data are now filtered on the operating state, which gives information about the proper power production, and thus they can be used to compare active power measurements against the wind velocity at the nacelle with the theoretical power curve. This tool can be used to verify if the contractual obligations between the original equipment manufacturer and the wind farm operator are met.

4. THE SCADA DATABASE ANALYSIS: THE STUDY OF THE WIND FARM BEHAVIOUR

An analysis of the behavior of the turbine park has been performed by the point of view of the nacelle response to the wind: discrepancies between the wind direction measured respectively by the anemometer and by the turbine nacelles have been investigated throughout the park and plotted on a three-dimensional graph along all the wind rose. It is intuitively expected such discrepancy being a function of the distance between the turbine and the anemometer: this effect is clearly visible in the subsequent three-dimensional graph, Figure 7.

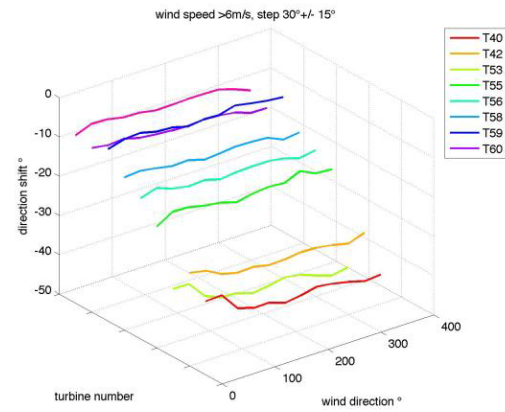


Fig. 7. Anemometer-nacelle wind direction shift calculated referring to the met mast

Yet, such amplitude, increases with the nacelle-anemometer distance, is not homogeneously distributed along the wind rose, as might be expected and as is shown in Figure 8. This should be due to wake effects, which can be further investigated with numerical tools such as CFD (Computational Fluid Dynamics) and the actuator disc model [15].

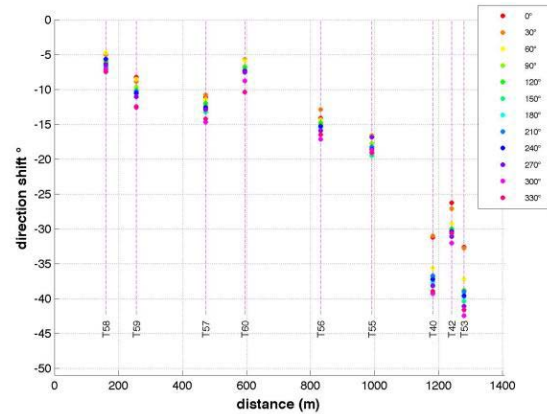


Fig. 8. Anemometer-nacelle wind direction spread vs distance, sector by sector

5. THE NUMBER MAP

The above analysis provides useful indicators for inquiring wind farm performances and malfunctioning on a large time scale. Yet, it might be useful to take trace of granular information: what each turbine does on the same 10 minute time basis as the SCADA database. The idea is therefore to associate to each 10 minute time step an appropriate number codifying smartly the information contained in the control system database. Doing this, one turns the issue of performance monitoring into a numerical and statistical problem, for which hugeness of the sample datasets becomes a power rather than a limitation.

Codifying with a number what each turbine does during a 10 minute time step is quite straightforward: the idea is to associate to each Operating State a digit, which shall turn to 1 if the corresponding Operating State turns on during the time step, or else remains 0. The only exception to this rule shall involve the “Grid Operating” operating state: actually one should consider “productive” a 10 minute time step only if the percentage of power output production time exceeds a fairly high threshold, which for the present work has been established at 75%.

As shall be shown below, the simplest statistical indicators as mode, mean and standard deviation provide powerful and simple explanatory answers from the complexity of the input data.

In the number map of the turbine operating states a meaning has been assigned to the hugeness of the number itself: a hierarchy of digits has been established, the rightmost digit being associated to the state most expected and standard (Grid Operating). Moving from right to left along the digits, one encounters the Automatic Start-Up phase when the turbine is ok but expecting enough wind strength to restart, all the restart and system test phases and finally, leftmost, the most traumatic operational phases: the Brake Programs.

Further time steps have been classified according to another criterion: production (or potential production) or not. It is indeed crucial to distinguish whether a turbine is producing output, or is not producing but not because of its operational malfunctioning (likely because there is not enough wind), or is not producing because of faults. A time step has therefore been considered not productive neither potentially productive if the sum of the percentages of activation time of “Grid Operating” and “Automatic Start-up” operating states does not exceed a threshold, which has been established for the present work at 25%. For each turbine, a first indicator of operational quality is counting productive and not productive time steps and computing the mode of the Operating States throughout these two sets separately. The order of magnitude of the number of productive and not

productive steps for each turbine provides first evidence of possible malfunctioning and the mode of the Operating States on the set of not productive time steps provides first explanations of malfunctioning reasons. The following Table 1 displays such approach for a sample period of five months and highlights a considerable operational anomaly for turbine T55 with respect to the other turbines of the wind farm; further turbine T42 peaks along the farm for its sensibly better performances.

Table 1. Statistics on productive and not productive time steps

Turbine	Number of Productive Steps	Mode of Productive Steps	Number of Not productive Steps	Mode of Not productive Steps
T40	4163	1 Mains Operation	156	14 Brake program 60
T42	4295	1 Mains Operation	24	3 Mains run-up – 4 Run-Up
T53	4133	1 Mains Operation	186	14 Brake program 60
T55	3145	1 Mains Operation	1174	13 Brake program 52
T56	4158	1 Mains Operation	161	14 Brake program 60
T57	4112	1 Mains Operation	207	14 Brake program 60
T58	4187	1 Mains Operation	132	15 Brake program 75
T59	4129	1 Mains Operation	190	14 Brake program 60
T60	4207	1 Mains Operation	111	14 Brake program 60

The above analysis highlights tendencies along the history of each turbine separately. Even more interesting is considering “horizontally” the park as a whole and inquiring step by step turbine operational deviations from the main trend of the farm: an anomalous time step for a given turbine is defined as a 10 minute interval during which such turbine behaves differently from the mode of the farm. Having performed such horizontal separation of time steps, subsequently a vertical analysis along the history of all the anomalous time steps of each turbine can be performed: they can be separated in productive (or potentially productive) and not productive, as defined above, and the number of time steps falling in each set can be analyzed, since this provides useful indicator on the operational behavior. Actually one can inquire whether a turbine a turbine deviates from the main trend of the farm mainly because it performs better or instead for malfunctioning. Further the mode of the states on the anomalous, respectively productive and not productive, steps of each turbine can be computed. In particular, the mode of the states on the anomalous not productive steps is highly relevant for detecting why a given turbine deviates problematically from the dominant farm behavior. This analysis provides useful indications for fault diagnosis and for building a historic database of operational problems of each turbine. Below, Table 2 displays such analysis on the same 5 months period as Table 1 above and highlights the most urgent Brake Programs for each turbine.

Table 2: Statistics on productive and not productive anomalous time steps

Turbine	Number of Anomalous Steps	Mode of Anomalous Steps	Number of Anomalous Productive Steps	Mode of Anomalous Productive Steps	Number of Anomalous Not productive Steps	Mode of Anomalous Not productive Steps
T40	509	14 Brake program 60	358	3 Mains run-up – 4 Run-Up	151	14 Brake program 60
T42	437	3 Mains run-up – 4 Run-Up	414	3 Mains run-up – 4 Run-Up	23	3 Mains run-up – 4 Run-Up
T53	604	14 Brake program 60	423	2 Start-Up	181	14 Brake program 60
T55	1413	13 Brake program 52	249	1 Mains Operation – 3 Mains Run-Up	1164	13 Brake program 52
T56	514	14 Brake program 60	359	3 Mains run-up – 4 Run-Up	155	14 Brake program 60
T57	592	14 Brake program 60	390	2 Start-Up	202	14 Brake program 60
T58	512	15 Brake program 75	392	3 Mains run-up – 4 Run-Up	120	15 Brake program 75
T59	590	14 Brake program 60	405	2 Start-Up	185	14 Brake program 60
T60	527	3 Mains run-up – 4 Run-Up	421	3 Mains run-up – 4 Run-Up	106	14 Brake program 60

The Operating States database basically provides what each turbine has done and the method above is able to encode and follow granularly operational behavior and its evolution. For diagnosis sake, it is useful to combine such analysis with a similar one involving the Status Codes database, which basically encodes, through Error, Warning and Information entries, why each turbine behaves as described by the Operating States. Actually the not productive time steps have been isolated and on this dataset a numerical map of the Status Codes, resembling the one adopted for the Operating States, has been applied, assigning to each Status Code a digit, which turns to 1 if the corresponding Status Code turns on during the 10 minute time interval. The mode of the Status Codes on the not productive dataset has been computed. As displayed in the following Table 3, this data-mining algorithm provides consistent interpretation for malfunctioning diagnosis. The turbine T55 has undergone an extended not productive phase, which is not highlighted by any Status Code: this is consistent with a manual maintenance, which has actually gone on. For the other turbines, the analysis displays malfunctioning causes associated to Frequency Converter Errors and Overload Gear Oil Pump: these information is extremely useful not only for investigating ex-post underperformance but also for diagnosis and future fault prevention, since it points out the main operational stress of each turbine.

Table 3: Status code statistics on not productive time steps

Turbine	Number of not productive steps	Mode of the Status Codes of the not productive steps
T40	156	4 Manual stop – on site 12 Manual yaw 19 Manual brake 20 Overload gear oil pump 0 System OK
T42	24	4 Manual stop – on site 12 Manual yaw 19 Manual brake 20 Overload gear oil pump
T53	186	4 Manual stop – on site 12 Manual yaw 19 Manual brake 20 Overload gear oil pump
T55	1174	4 Manual stop – on site 12 Manual yaw 19 Manual brake 20 Overload gear oil pump
T56	161	4 Manual stop – on site 12 Manual yaw 19 Manual brake 20 Overload gear oil pump
T57	207	4 Manual stop – on site 12 Manual yaw 19 Manual brake 20 Overload gear oil pump
T58	132	5 Frequency converter error
T59	190	4 Manual stop – on site 12 Manual yaw 19 Manual brake 20 Overload gear oil pump 50 Breakdown obstacle light
T60	111	4 Manual stop – on site 12 Manual yaw 19 Manual brake 20 Overload gear oil pump

The analysis above is extremely useful for detailed fault diagnosis. Yet it is interesting also to summarize the amount of operational malfunctioning each turbine has faced, disregarding the details of it but just keeping trace of quantity and severity. For this reason, on the grounds of the above method, two Malfunctioning Indices have been built.

The first Malfunctioning Index is defined as the ratio of the number of not productive neither potentially productive time steps to the number of anomalous time steps, as in the following Equation (2):

$$I_1 = \frac{N_{not\ productive}}{N_{anomalous}} \quad (2)$$

The second Malfunctioning Index is defined as the ratio of the number of anomalous not productive time steps to the number of anomalous productive time steps. This index quantifies if the turbine deviates from the trend of the farm mainly because it performs better or instead because it does not produce power output. Such Index is defined in the following Equation (3):

$$I_2 = \frac{N_{anomalous\ not\ productive}}{N_{anomalous\ productive}} \quad (3)$$

The following Figures 9, 10, 11, 12 display the results for the two Malfunctioning Indices on the same analysis period as above, both on monthly and global 5 months scale: the trend of the two indices along the wind farm is the same, even if the second one better sharpens the peaks, and they indeed brilliantly highlight the turbines most affected by operational faults.

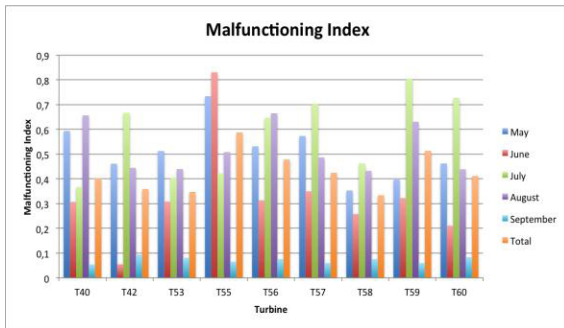


Fig. 9. Malfunctioning Index I1 on a monthly basis

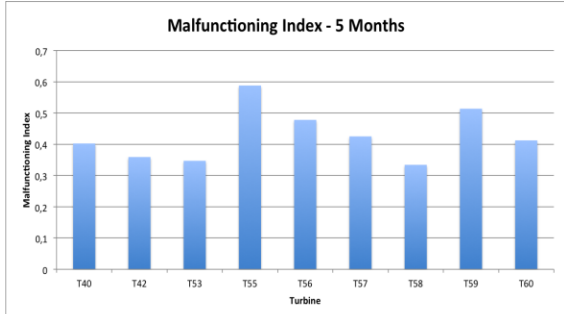


Fig. 10. Malfunctioning Index I1 on a 5 month basis

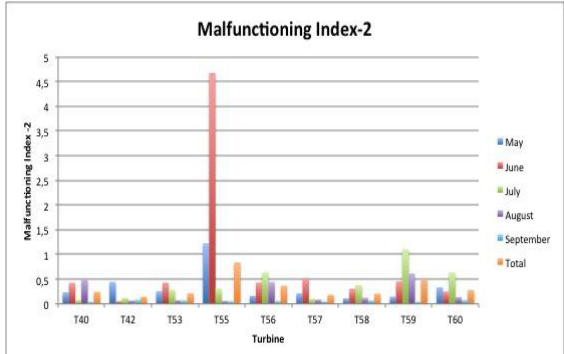


Fig. 11. Malfunctioning Index I2 on a monthly basis

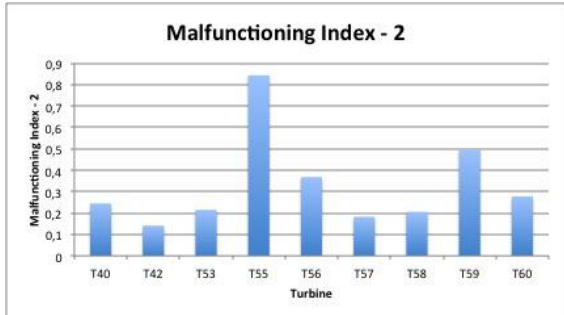


Fig. 12. Malfunctioning Index I2 on a 5 month basis

5. RESULTS AND CONCLUSIONS

In this work a SCADA data analysis was performed on a wind farm composed of nine wind turbines and new post-processing methods are proposed for the monitoring of the aerogenerators. The most important turbine parameters were identified on the SCADA dataset and data mining was performed both for the performance analysis

and for the understanding of the wind turbines behaviour during operations. Then routines were developed to crosscheck and make a series of controls on the acquired data. An automatic routine, providing indicators of the power availability of the wind turbines was defined. Significant deviation from the mean statistics on the whole park, and thus the malfunctioning of wind turbine T53 was detected. The operating states were then used both to confirm the malfunctioning of wind turbine T53 and to select data to be analysed to investigate the causes of its anomalous behaviour. Also the SCADA measured values are fundamental to study critical operating situations such as strong wakes loads due to rotor misalignment. Results demonstrate that a proper selection of the measured parameters, considering the operating and status code dataset, can be very useful to investigate the real performances of a wind farm and to understand the behaviour of each wind turbine. Further the analysis of the operational conditions of the wind farm and of single turbines has been carried on through a number map, which transforms performance monitoring into a numerical problem, assigning a digit to the activation of each operating state during a 10 minute time step. Statistical analysis on the number map is a powerful tool in fault diagnosis and for inquiring reasons of the main operational stress of each turbine and of the whole farm. Further two Malfunctioning Indices have been built, codifying amount and severity of operational downtime of each turbine. It has been shown that such Indices brilliantly capture the trend of the farm behavior. The proposed data mining techniques and analysis methods can be helpful both to increase the reliability of the assessment techniques and to define optimal repair/replacement and preventive maintenance policies that play a major role in case of energy production.

References

- [1] Catmull S.: *Self-Organising Map Based Condition Monitoring of Wind Turbines*. EWEA 2011 - 14-17 March 2011, Brussels, Belgium.
- [2] Lapira E., Brisset D., Davari Ardakani H., Siegel D., Lee J.: *Wind turbine performance assessment using multi-regime modeling approach*. Renewable Energy 45 (2012) 86-95.
- [3] Kusiak A., Li W.: *The prediction and diagnosis of wind turbine faults*. Renewable Energy 36 (2011) 16.
- [4] Carvalho H, Gaião M, Guedes R.: *Wind Farm Power Performance Test, in the scope of the IEC 61400-12.3*. EWEC 2010 European Wind Energy Conference & Exhibition Proceedings - Tuesday 20 - Friday 23 April 2010, Warsaw, Poland.

- [5] Gill S., Stephen B. and Galloway S.: *Wind Turbine Condition Assessment Through Power Curve Copula Modeling.* Ieee Transactions On Sustainable Energy, Vol. 3, No. 1, January 2012.
- [6] Paiva L. T., Veiga Rodrigues C., Palma J.M.L.M.: *Determining wind turbine power curves based on operating conditions.* Wind Energy, August 2013, DOI: 10.1002/we.1651.
- [7] Kusiak A., Verna A.: *Monitoring wind farms with performance curves.* IEEE Transactions On Sustainable Energy Vol. 4, No. 1, January 2012.
- [8] Gallardo-Calles J. M., Colmenar-Santos A., Ontanon-Ruiz J., Castro-Gil M.: *Wind control centres: State of the art.* Renewable Energy Volume 51 March 2013.
- [9] Schlechtingen M., Ferreira Santos I., Achiche S.: *Wind turbine condition monitoring based on SCADA data using normal behavior models.* Part 1: System description. Applied Soft Computing Volume 13 January 2013.
- [10] Elijorde F.I., Moon D., Ahn S., Kim S., Lee J.: *Wind turbine performance monitoring based on hybrid clustering method.* Future Information Communication Technology and Applications, Lecture Notes in Electrical Engineering Volume 235, 2013, pp 317-32.
- [11] Schlechtingen M., Ferreira Santos I., Achiche S.: *Using Data-Mining Approaches for Wind Turbine Power Curve Monitoring: A Comparative Study.* Sustainable Energy, February 2013, Volume PP, Issue 99, pp. 1-9, DOI:10.1109/TSTE.2013.2241797.
- [12] Bangalore P., Bertling L.: *An approach for self evolving neural network based algorithm for fault prognosis in wind turbine-* IEEE Powertech Grenoble 2013 Proceedings.
- [13] Borchersen A.B.: *Predicting faults in wind turbines using SCADA data.* 51st Aiaa Aerospace Sciences Meeting Including The New Horizons Forum And Aerospace Exposition, January 2013. DOI: 10.2514/6.2013-313.
- [14] Yang W.,Court R., Jiang J.: *Wind turbine condition monitoring by the approach of SCADA data analysis.* Renewable Energy, May 2013, Volume 53, pp. 365-376, DOI:10.1016/j.renene.2012.11.030.
- [15] Castellani F. , Vignaroli A.: *An application of the actuator disc model for wind turbine wakes calculations.* Applied Energy – Elsevier – ISSN 0306-2619 – 2012 – 10.1016/j.apenergy.2012.04.039.



Francesco CASTELLANI is an Associate Professor in Machine Engineering at the University of Perugia (ITALY). He is involved in many research activities dealing with modelling and control of mechanical systems. His research on wind energy systems is focused on:

- numerical and experimental wind turbines studies;
- wind resource assessment;
- numerical simulation of wind flow and wakes on complex terrain sites.;
- condition monitoring and fault diagnosis through SCADA data analysis;
- wind tunnel test of small wind turbines.

APPLICATION OF LOW-COST MAGNETIC FIELD AND ACCELERATION SENSORS IN DIAGNOSTICS OF LARGE-SIZE STRUCTURES

Przemysław SZULIM, Jędrzej MĄCZAK, Krzysztof ROKICKI, Kamil LUBIKOWSKI

Warsaw University of Technology, Faculty of Automotive and Construction Machinery Engineering
Narbutta 84, 02-524 Warszawa, Poland, e-mail: p.szulim@mechatronika.net.pl, jma@mechatronika.net.pl,
k.rokicki@mechatronika.net.pl, klubikowski@mechatronika.net.pl

Summary

The paper presents the possibilities of using low-cost magnetic and acceleration sensors in diagnostic systems of large-scale structures made of ferromagnetic materials. It covers typical problems associated with their use as well as the review of commercially available low-cost solutions. A specially designed magnetic sensor equipped with a CAN interface, which allows for connecting a number of transmitters into a measuring network, were tested during the experiment.

Keywords: diagnosis, magnetic sensors, MEMS sensors, diagnostic systems.

ZASTOSOWANIE NISKOBUDŻETOWYCH CZUJNIKÓW POLA MAGNETYCZNEGO I PRZYSPIESZEŃ W DIAGNOSTYCE KONSTRUKCJI WIELKOGABARYTOWYCH

Streszczenie

W pracy przedstawiono możliwość wykorzystania niskobudżetowych czujników pola magnetycznego i przyspieszeń w systemach diagnostyki konstrukcji wielkogabarytowych wykonanych z materiałów ferromagnetycznych. Przedstawiono typowe problemy występujące podczas ich użycia oraz dokonano przeglądu dostępnych na rynku tanich rozwiązań. W przeprowadzonym eksperymencie przetestowano specjalnie opracowane przetworniki pola magnetycznego wyposażone w interfejs CAN pozwalający na łączenie szeregu przetworników w sieć pomiarową.

Słowa kluczowe: diagnostyka, czujniki magnetyczne, czujniki MEMS.

INTRODUCTION

Use of magnetic information for diagnosing the condition of structures is not a new idea. There exist numerous methods and their commercial applications. Majority of them required are the so-called active methods, as they offer easier interpretation of results. Passive methods, which only rely on registration of changes in the magnetic field surrounding a structure, form a separate group. Such a passive method, along with research results, is described in [1] and [2]. Though the work related to this class of methods has not been completed yet, the results which have been obtained so far are often very promising. Some examples were presented in [3] where the passive magnetic methods were used during the experiment for monitoring the behavior of a large-size truss which was subjected to heavy loads. The examined truss corresponds to a structural element of steel warehouses. The truss was subjected to the loads which were similar to the loads occurring in actual facilities. The results of the experiment are presented in more detail in the further part of the article in connection with the description of magnetic field converters.

1. REVIEW OF SENSORS

In this chapter a review of low-budget magnetic field converters as well as the most interesting solutions, characterized by relatively good technical parameters and low price will be presented. The sensor described as the last one has been designed for the purpose of development of the diagnostic methods which rely on magnetic field measurements.

The MAG3110 sensor is an integrated, digital, tri-axial magnetic field sensor manufactured by Freescale. It has single measuring range and 8 sampling frequencies ranging from 0.63Hz to 80 Hz. The measuring range of the sensor is +/-1000uT, which in the case of a built-in 16-bit converter enables achievement of the resolution of 0.03uT. It is worth to note that the signal to noise ratio is very low for this sensor, as shown on the product sheet [4]. However, lack of information regarding the structure of the analogue part of the sensor suggests that not much attention was devoted to aliasing phenomena. The authors' experience with this sensor shows that the noise level is in fact lower than in the case of LSM303 sensor (described in the

further part of the article). The integrated electronic circuit of this digital sensor makes sure that the analog signal sampling is performed with pre-programmed frequency. Measurement data are available via the I2C bus. What is also worth noting there are separated power supplies for the analog and the digital parts. Thanks to this separation, the level of noise has been reduced in the measured signal. Temperature measurement of the semiconductor structure of the system is also available. The information regarding the temperature can be used for assuring temperature-wise adjustment of such parameters as sensitivity or bias, that is the parameters which are sensitive to temperature changes in a lesser or greater degree.

Another noteworthy sensor is the analog sensor which relies on the effect of giga-magnetoresistance. NVE Corporation manufactures numerous sensors. One of them, having the code AAH002 [5], is characterized by relatively high sensitivity and ability to operate in uni-polar configuration. It is undoubtedly the drawback but at the same time the characteristic feature of sensors of this type. The sensor can measure magnetic fields correctly only in the ranges from – to 0 or from 0 to + values. It is unable to perform measurements in the range from – to + values. At least the measurements cannot be performed in a simple measuring system. The sensor contains a bridge composed of measuring elements (Fig. 1). The voltage at the output of the bridge changes proportionally to the value of the applied magnetic field. The fact that the sensor is an analog one allows for building of own set of amplifiers and anti-aliasing filters, enabling much higher sensitivity and better elimination of measurement noise. What is more, this solution offers a theoretical possibility of constructing a low-cost differential magnetic field sensor.

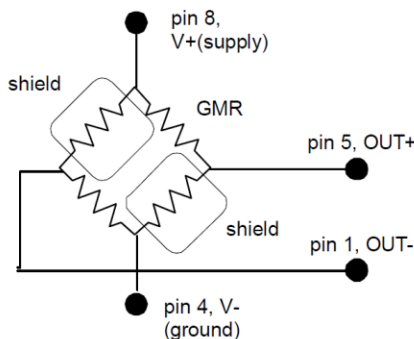


Fig. 1 Electrical diagram of AAH002 sensor [5]

Another interesting device is a RM3000 geomagnetic sensor offered by PNI Corporation [6].

This relatively cheap sensor relies on the hysteresis effect which occurs in the ferromagnetic core. The company supplies separate analog sensors as well as ASIC systems which are integrated analog-digital sets.

Analyzing available sensors, it is worth considering a ready integrated solution since analog sensors require quite complex electronic circuit to obtain a measurement. The sensors are characterized by a typical measuring range, similar to the ones mentioned earlier. Relatively high resistance to temperature changes is undoubtedly an advantage of this sensor. It is a very important feature, since there are numerous applications which require the sensors to operate in an environment with varying parameters, such as temperature, humidity, etc. Insensitivity of a sensor to changes of these parameters leads to reduction of measurement errors.

An acceleration sensor which deserves more attention from among the wide range of acceleration converters is the ADXL001 (Fig. 2).

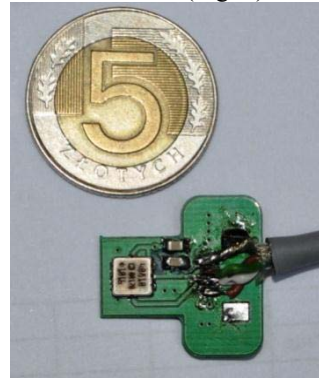


Fig. 2 Acceleration sensor ADXL001 on a test board

ADXL001 is a single-axis acceleration sensor from Analog Devices [7]. Depending on the version, the sensor can measure acceleration in the range of +/-70g, +/-250g and +/-500g. The sensor relies on MEMS technology. It is also an analog sensor. Since the sensor is characterized by quite extensive band of 0-33kHz, thus it can be used in various types of vibration tests as well as in modal analysis.

The acceleration and magnetic field sensor board (Fig. 3) has been developed for the needs of the experiment aimed at testing the possibilities of using the passive magnetic methods for diagnosis of structures (Fig. 3). The board consists of several principal parts. The main measuring element is an integrated LSM303 tri-axial accelerometer combined with a tri-axial magnetometer sensor. Basic technical parameters of the sensor can be found in the product sheet [8].



Fig. 3 Magnetic field and acceleration sensor board

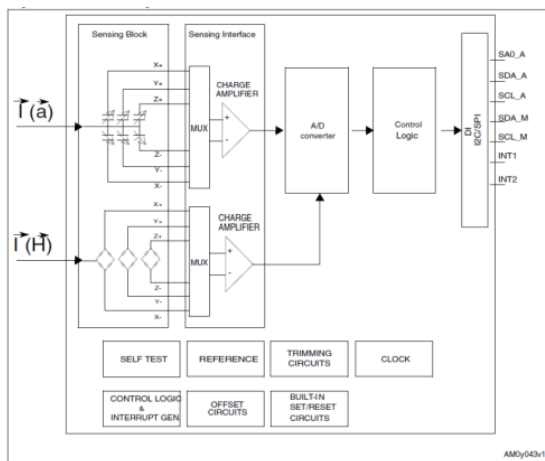


Fig. 4 Internal diagram of the LSM303 sensor [8]

The signal from the measurement bridges undergoes preliminary amplification and processing with the use of a 12-bit A/C converter. The signal becomes available to the master computer/microcontroller via the I2C bus. It is a typical bus for communication between two devices operating at a close distance from each other. It is not suitable for transmitting data over longer distances and that is why apart from communicating with the LSM303 sensor, the developed sensor board is also involved in transmitting data to the CAN bus. The magnetic sensor has 7 sensitivity settings. In the variant with the biggest sensitivity the sensor carries out measurements in the range of $\pm 1.3g$, which, when combined with the sensitivity of the converter, means measurement accuracy at the level of $1mg$. The last variant is the variant with the broadest range which enables magnetic field measurements in the range of $\pm 8.1g$. Frequency of measurements is the issue which is important in the case of measurements of this type. Seven sampling speeds can be set for this sensor ranging from $0.75Hz$ to $70Hz$. One should note that frequency of sampling is not synonymous with the necessity of reading the data from the sensor at the same rate. The manufacturer also informs that as the sampling frequency changes, so does the anti-aliasing filter band. It is a very important issue which, as it turned during the tests, has not been solved well by the manufacturer. While measurements are performed

on structures, there often happen situations where apart from the static magnetic field, which is associated with the earth's magnetic field and the magnetic field generated by the structure itself, there appears a magnetic field component which is characterized by significant frequency and often associated with the network noise. In order to properly filter off the noise it is necessary to create registration conditions which fulfill the Nyquist criteria. As it turned out the manufacturer did not provide sufficiently good anti-aliasing filters, which oftentimes caused numerous problems. The analog track is undoubtedly the weak side of the solution. An important feature of the LSM303 sensor is the fact that it has been factory-calibrated. The calibration concerns sensitivity of the axis, influence of temperature on the sensor's axis and offset. In this very case, offset is understood to be a certain permanent component which appears in the measured signal. It is worth remembering that calibration concerns the LSM3003 only. This sensor is embedded in a device and due to the presence of soft and hard ferromagnetic materials it requires re-calibration. This issue is very important, however due to its extensive nature it goes beyond the framework of the present article. It is also worth noting that the axis of the sensor need not necessarily be perpendicular while the errors associated with the axis not being perpendicular to one another may even be in the range of several degrees. These items are also the parameters which are subject to calibration. The manufacturer's solution, which gives a user the possibility of selecting the sensitivity, offers, on the one hand, bigger flexibility but on the other it generates a real calibration issue, since calibration would have to be done separately for each of the ranges.

The possibility of measuring the acceleration is an interesting feature of the constructed device. A tri-axial accelerometer, built-in into the LSM303 sensor, has been developed in MEMS technology. Its most important features include: sampling frequency of up to $1kHz$ (the signal from the accelerometers is only available in digital format), three measurement ranges: ± 2 , ± 4 , $\pm 8g$, as well as quite good temperature-related parameters, namely influence of temperature on the stability of sensitivity and influence of temperature on the stability of zero value. Quite a narrow measuring range makes it impossible for the device to be used for e.g. measuring the vibration of structures. However use of the sensor for measuring the deformation of structures presents an interesting application of the device. MEMS-technology-based sensors enable measurement of gravitational acceleration. Similarly as in the case of other types of sensors, the measurement is indirect and it is performed by measuring the force interacting with some standard mass as a result of acceleration. Since the sensor also measures the value of a constant component of acceleration, then while assuming that

the sensor is immobile it is possible to measure the gravitational acceleration. Since its value can be treated as a constant value, thus measurement of the acceleration vector can be used for determining the angle of turn of the sensor. A sensor located in a measurement device and attached to the examined structure, can easily be used for detecting a spot defect (e.g. caused by buckling of its elements). Choice of the angles which describe the variance of the acceleration vector, as seen in the system of the sensor's coordinates, depends on many factors. It is usually best to choose the ones whose interpretation will be easiest and the ones which will later on provide the best information. The below figure (Fig. 5) presents an example of a coordinate system of a sensor, featuring the marked acceleration vector and the two angles describing variance of the vector thus describing the movement of the sensor with regard to a certain straight line which is perpendicular to the earth.

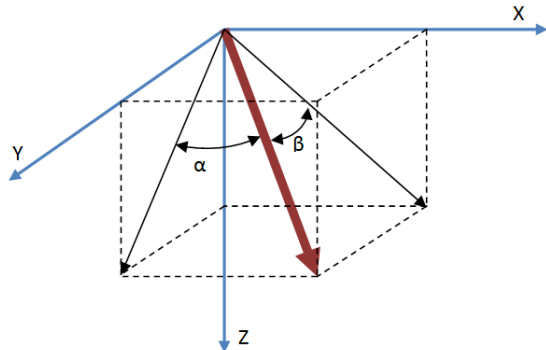


Fig. 5 Coordinate system showing angles of revolution of the sensor

It is worth noting that precision of acceleration measurement achieved for the resolution of the 12 bit ADC converter and its range of 2g is 1 mg. For this data the precision of angle measurement of 0.05° is achieved for small values of angles α and β. What causes the problem is the measurement noise and that is why it is suggested that analog sensors with an enhanced analog measurement circuit should be used for achieving a more precise measurement.

2. CALIBRATION

Characteristic features of low-cost sensors are the big discrepancies of such parameters as sensitivity or zero level (the so-called offset). Hence before the possibilities offered by these sensors are used in practice, they must first undergo calibration. Calibration of sensors is quite complex and it goes beyond the scope of the present article. Only an outline of the process will be presented here, along with the general principle demonstrating the way in which calibration can be performed. The equation presented below describes the easiest model which links the value registered by a sensor to the actual physical value:

$$m_f = s * (m_m - b) \quad (1)$$

The physical value m_f is registered by the sensor as m_m . Once a certain constant value b is subtracted and the result is multiplied by a sensitivity parameter s , we arrive at the physical interpretation of measurement m_f . In a situation of a measurement performed with the use of a tri-axial sensor, parameters b_i and s_i are assigned to each axis i . The model (1), however, fails to account for non-perpendicularity of the axis. This fact is only addressed by the model (2).

$$\begin{aligned} m_{f_i} = & s_{i1} * (m_{m_1} - b_1) + \\ & + s_{i2} * (m_{m_2} - b_2) + \\ & + s_{i3} * (m_{m_3} - b_3) \end{aligned} \quad (2)$$

which in the case of tri-axial measurement can be presented by means of a matrix equation (3)

$$\overline{m_f} = S * (\overline{m_m} - B) \quad (3)$$

where S is a matrix with a dimension of 3x3, while B is matrix with a dimension of 3x1. When the sensor is non-linear, then its non-linearity can be approximated by means of a second degree multinomial. In such a case the measurement model can be as presented by equation (4).

$$\overline{m_f} = S * \begin{pmatrix} a_x(m_{mx} - b_x)^2 & m_{mx} - b_x \\ a_y(m_{my} - b_y)^2 + m_{my} - b_y \\ a_z(m_{mz} - b_z)^2 & m_{mz} - b_z \end{pmatrix} \quad (4)$$

Similarly as (1) and (2), the model described by equation (4) can serve as the basis for developing a system of equations for the purpose of determining the unknown factors of matrices S , B and A (a_x, a_y, a_z). To solve such a system of equations one needs to use equation (5), i.e. an equation determining the module of a measurement vector which should be a constant value (on the assumption that the vector field has a constant value).

$$|\overline{m_f}| = \sqrt{m_{fx}^2 + m_{fy}^2 + m_{fz}^2} \quad (5)$$

While using equations (4) and (5) it is possible to develop a system of 15 equations, yet it will be impossible to make, in a simple way, a transformation which would enable determining all the coefficients which are sought. It could be done while using e.g. the Newton's algorithm which would bring us closer to the solution. However, it is also worth noting that the results of the measurements which have been obtained while using a tri-axial sensor can be shown on the graph XYZ. In the case of a calibrated sensor the vector should be "sliding" with its vertex on the surface of a sphere. Calibration errors for offset B will result in shift of the center of the sphere, sensitivity-related errors result in emergence of an ellipsoid instead of a

sphere, while the errors associated with skewness of the axis can lead to either a turn of the ellipsoid or its deformation. Fig. 6 presents a graph with a trace of a magnetic field vector obtained during multiple rotations of the sensor. Such a big number of measurement points is relatively easy to obtain for magnetic field sensors, however in the case of accelerometers, for which measurements have to be made in static conditions (only gravitational acceleration is permitted), such a big number of measurement points would be difficult to achieve.

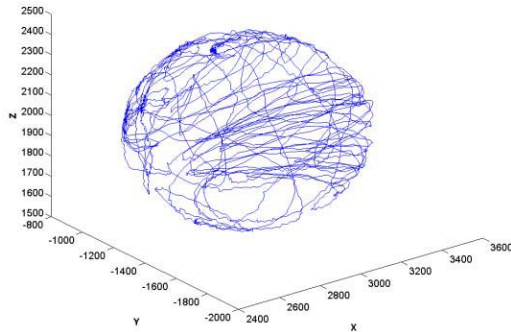


Fig. 6 Measurement data registered by the sensor MAG3110

3. EXEMPLARY RESULTS OF MEASUREMENTS

This section presents some of the results obtained during the experiment involving application of load to a steel truss used in the structure of rooftops of warehouses [3]. Numerous measurements were performed during the experiment, such as strain gauge measurements, measurements of deflection with the use of LVDT, modal measurements or measurements of deflection while relying on visual methods. Mainly the measurements involving low-cost sensors will be presented.

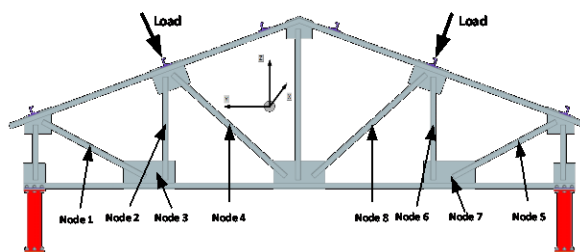


Fig. 7 Location of sensors

In the first phase of the measurement, the examined structure is subjected to a gradually increasing load produced by two hydraulic actuators generating force from 0 to 35 kN each (Fig. 7). The

structure was damaged due to buckling when the load reached around 35 kN.

Fig. 8 presents the graph showing the changes of the angle β during the experiment. The upper graph shows the input force while the lower graph contains the results of measurement of the angles in three measurement nodes. It should be noted that the 10 so-called measurement nodes were placed on the structure, with measurements conducted in these nodes while using strain gauges and magnetic sensors as well as accelerometers.

Figure 8 shows that during the first phase of the load application on the construction, when the force changed in the range from 10 to 35 kN, the angle of turn, as registered in respective nodes, practically did not change.

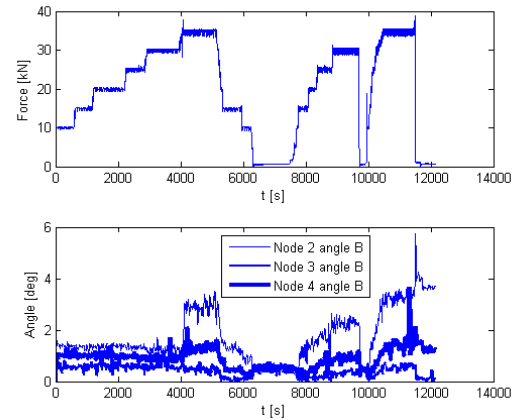


Fig. 8 Influence of the load on angle β

It is only the buckling that brought a rapid change of readings. The impact of buckling varied, depending on the location of a measurement node on the frame. Once buckling occurred (approx. in the 4000th second of the experiment), the load-exerting force had permanent influence on the value of the angle registered by the sensors. The reason was that once the load was released the structure did not return to its original form but remained permanently bent. Subsequent load cycles led to growth or decrease of the structure's deflection, which was registered by the sensors.

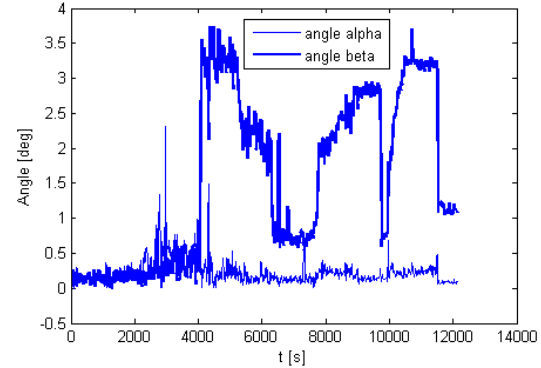


Fig. 9 Change of angles α and β for node 6 during the experiment

Fig. 9 presents a graph showing the values of angles α and β in the measurement node no. 6. It can be seen from the graph that angle α has not changed during the experiment. Due to the nature of the buckling, changes of angle α were small, that is why we neglected them while presenting the results. Figure 10 presents the results of measurement of angles β for measurement nodes 6,7,8. The impact of buckling is distinctly visible in each case. It should be added that the relatively high value of the measurement noise is associated with the rather poor properties of the filters. Since other additional measurements were performed on the structure's surface during each subsequent phase, thus each case of impact or leaning against the structure was registered by the accelerometers. The target version should be equipped with a filter cutting off higher frequencies of the signal.

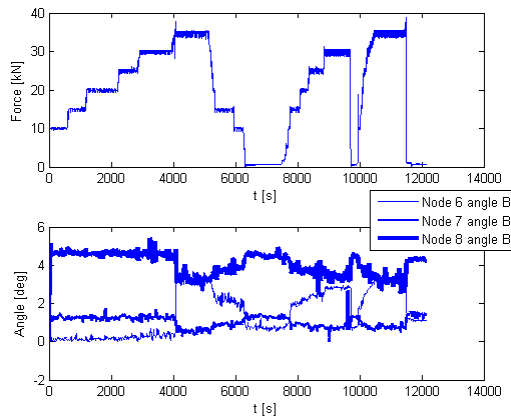


Fig. 10 Impact of the load on change of angle β

Figure 11 contains a graph showing changes of the module of the magnetic field's vector during the experiment. The presented results concern the measurement nodes 1-3.

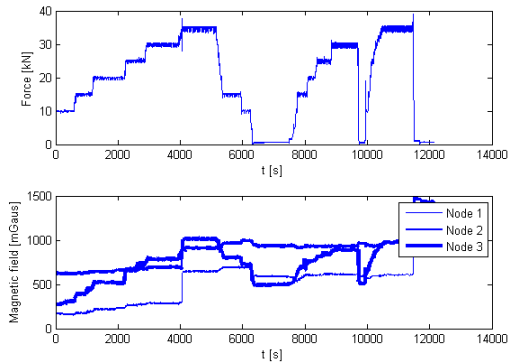


Fig. 11 Change of the module of the magnetic field's vector for the nodes 1,2 and 3

Figure 12 presents the same situation for measurement nodes 5-7. The influence of the load-exerting force, shown in the upper graph, is clearly visible. It can also be seen that occurrence of the defect led to rapid growth of the magnetic field's value.

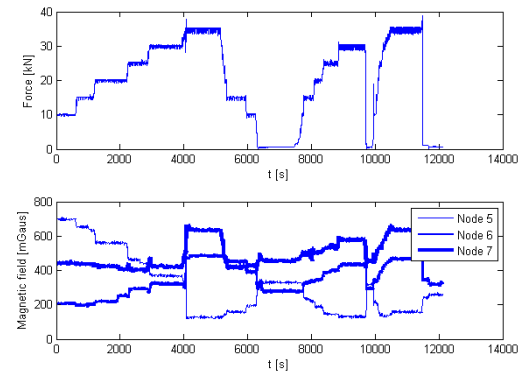


Fig. 12 Change of the module of the magnetic field's vector for the nodes 5,6 and 7

4. CONCLUSIONS

The article presents several selected low-cost magnetic field and acceleration sensors which can be used in diagnostic systems. A review of the sensors is presented while pointing to some of their features. Also an outline of the process of calibration of sensors is presented, along with the results of data registration during an actual experiment. As has been presented above, the sensors provide interesting information which can be successfully used while building diagnostic systems.

REFERENCES

- [1] Gontarz S., Radkowski S., *Impact of Various Factors on Relationships Between Stress and Eigen Magnetic Field in a Steel Specimen*, IEEE Transactions on Magnetics, 48(3), 2012
- [2] Gałęzia A., Gontarz S., Jasiński M., Mączak J., Radkowski S., and Seńko J., *Distributed System for Monitoring of the Large Scale Infrastructure Structures Based on Analysis of Changes of its Static and Dynamic Properties*, Key Engineering Materials, vol. 518, pp. 106–118, 2012,
- [3] Mączak J., *A Structural Health Monitoring System Based on an Analysis of Changes in the Static, Dynamic and Magnetic Properties of the Structure*, in B.H.V. Topping, (Editor), "Proceedings of the Eleventh International Conference on Computational Structures Technology", Civil-Comp Press, Stirlingshire, UK, Paper 86, 2012.
- [4] *Xtrinsic MAG3110 Three-Axis, Digital Magnetometer* [Online]. Available: http://freescale.com/files/sensors/doc/data_sheet/MAG3110.pdf. [Accessed: 01-Dec-2013]
- [5] *AA and AB-Series Analog Sensor*. NVE Corporation. [Online]. Available: http://www.nve.com/webstore/catalog/redirect.php?action=url&goto=www.nve.com%2FDownloads%2Fanalogue_catalog.pdf [Accessed: 01-Dec-2013]

- [6] *RM3000 / RM2000 | PNI Sensor Corporation* [Online]. Available: <http://www.pnicorp.com/products/RM3000-RM2000#Features>. [Accessed: 01-Dec-2013].
- [7] *ADXL001 datasheet and product info | High Performance Wide Bandwidth iMEMS® Accelerometer | MEMS Accelerometers | Analog Device* [Online]. Available: <http://www.analog.com/en/mems-sensors/mems-accelerometers/adxl001/products/product.html>. [Accessed: 01-Dec-2013].
- [8] *LSM303DLM Sensor module: 3-axis accelerometer and 3-axis magnetometer - STMicroelectronics* [Online]. Available: http://www.st.com/web/catalog/sense_power/FM89/SC1449/PF251902. [Accessed: 01-Dec-2013].

Jędrzej MĄCZAK, PhD is an assistant professor at the Institute of Vehicles of the Warsaw University of Technology. His scientific interests are distributed diagnostic systems, machine diagnostics and methods of analysis of vibroacoustic signals.



Przemysław SZULIM, M.Sc., a Ph.D. student in the Institute of Vehicles of Warsaw University of Technology.



Kamil LUBIKOWSKI, M.Sc., a Ph.D. student in the Institute of Vehicles of Warsaw University of Technology.



Krzysztof ROKICKI, M.Sc., a Ph.D. student in the Institute of Vehicles of Warsaw University of Technology.



TOPOLOGICAL MODEL OF APITUDE OF THE MEASUREMENT CIRCUITS OF MAIN SUBASSEMBLIES OF AN INTERNAL COMBUSTION ENGINE CRANKSHAFT-PISTON ASSEMBLY

Piotr BZURA

Gdansk University of Technology, Faculty of Ocean Engineering and Ship Technology
email: pbzura@pg.gda.pl

Summary

The paper presents a topological model allowing to determine the probability of aptitude of the diagnosing system (SDG) individual measuring circuits and also to determine to what degree they influence the assessment of the technical condition of an arbitrary main subassembly of crankshaft-piston assemblies as a diagnosed system (SDN).

Keywords: emitted signal F, measuring circuit.

MODEL TOPOLOGICZNY ZDATNOŚCI TORÓW POMIAROWYCH GŁÓWNYCH PODZESPOŁÓW UKŁADÓW KORBOWO-TŁOKOWYCH SILNIKÓW SPALINOWYCH

Streszczenie

W artykule przedstawiony został model topologiczny umożliwiający określenie prawdopodobieństwa zdatności poszczególnych torów pomiarowych systemu diagnozującego (SDG) oraz w jakim stopniu wpływają one na ocenę stanu technicznego dowolnego głównego podzespołu układów korbowo-tłokowych jako systemu diagnozowanego (SDN).

Słowa kluczowe: sygnał emitowany F, tory pomiarowe.

1. INTRODUCTION

Main subassemblies of a marine internal combustion engine crankshaft-piston assembly, in view of their durability, reliability and safety, require constant surveillance by the diagnosing system (SDG). Such systems are being produced by the biggest ship engine manufacturing companies: the German-Danish MAN Diesel company and the Finnish-Swiss Wärtsilä company. However, in the operation practice the same SDGs cannot be used for assessment of the state of different internal combustion engine types. Each engine type without its established diagnosing system should be first subjected to a proper identification procedure and only then the best-fitting diagnosing system can be selected from the existing ones. However, it must be remembered that rational use of engines requires good knowledge of the reliability and durability of the diagnosing systems. The diagnosis is formulated under the assumption that the diagnosing system is in a state of full aptitude. The less the SDG reliability and durability is, the less is the probability that at any time the diagnosing system will be in the state of full aptitude.

This means that probability of formulating a wrong diagnosis is then greater. Therefore, this paper presents a topological model allowing to determine the probability of aptitude of SDG individual measuring circuits and also to determine to what

degree they influence the assessment of the technical condition of an arbitrary main subassembly of the crankshaft-piston assemblies (SDN).

2. MEASURING CIRCUITS

In order to perform a measurement [4,8], a measuring circuit must be set up, i.e. a path of signal from the source – friction node where the investigated physical phenomenon occurs – through the processing, comparing and transmitting elements to the output devices for visualizing and archiving the measurement results (Fig.1).

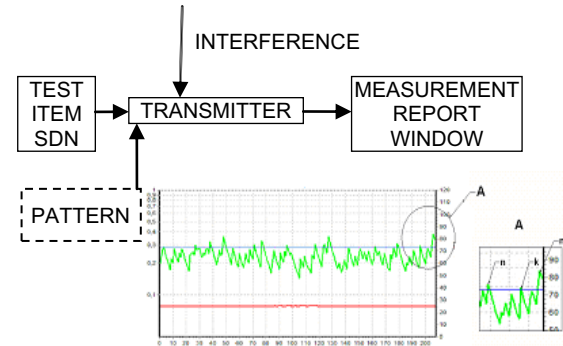


Fig. 1. Diagram of a measuring circuit
where: n - emitted signal amplitudes exceeding the reference level; k - very indistinct amplitudes

Measuring transducer is the measuring circuit basic element performing processing and detection of signals by means of piezoelectric (vibration and pressure) sensors. In other words, the function of those transducers is converting e.g. vibration into a corresponding modulated electric signal. The signal is then prepared for correct conversion into the digital form (e.g. electric charge amplification, removing the electronic noise, galvanic separation). Then the analogue (continuous) signal is changed into digital representation (digital signal) in the A/C converter. This process is carried out in 3 stages: sampling, quantization (digitization) and coding. The obtained digital output signal in the form of digital code is recorded as a bit word. Additionally, at the end the digital signal can be re-converted into voltage analogue signal and displayed. Fig.1 presents an example of measurement report window of the modified T-03 four-ball extreme pressure tester friction node vibration level [3]. The reference level, determined from pattern, defines the surface layer damage due to pitting.

In order to secure proper functioning of all the measuring circuit elements in a given application, the following parameters must be determined: transmission band, measurement range, measurement resolution, measurement sensitivity, measurement accuracy, measurement repeatability, and also the operation conditions (e.g. temperature, corrosion resistance, pressure fluctuations on the transducer etc.).

All the measuring circuit elements should be treated as dynamic objects, therefore all the quantities are time-dependent variables. In the case of disturbances a transitory phase occurs characterised by variability of all the quantities. In effect each measurement result is encumbered with errors of different character and causes. The following errors are distinguished [4,8,9,10,11]:

- measurement static errors resulting from non-ideal characteristics of the measuring elements caused by wrong calibration or by random character effects,
- dynamic errors resulting from the fact that the analogue part of the measuring circuit, the measurement sensor in particular, is not a proportional element (in the dynamic model sense), and also from the fact that digitization is performed at the end of the measuring circuit,
- signal errors: spurious signal caused e.g. by high combustion temperature – so called thermal shock,
- temperature drift caused by temperature fluctuations,
- signal deformations caused by the measuring circuit element connections.

Therefore, after a certain operation time the SDG will not be in a state of full aptitude and the measurement results will not be a sufficiently

reliable basis for assessment of the technical condition of a diagnosed main subassembly.

Therefore, the ability of measurement circuit diagnosing must be analysed.

3. RELIABILITY OF DIAGNOSIS

The main subassemblies of a crankshaft-piston assembly are the following: piston with rings and cylinder liner, piston rod with crosshead and, although in a less degree, slide bearings [2]. Safe functioning, particularly during starting the engine, depends on the degree of identification of their real technical condition. Therefore, reliability of the technical condition diagnosis will have an impact on the desired engine operation process. Preparing a reliable diagnosis means identifying the condition of a main subassembly as a diagnosed object (SDN). As SDN characteristics are random variables, estimation of their values is only approximate and the diagnosis of the object technical condition is reliable to a certain degree [5]. In order to estimate the degree of reliability, a multiplexer-based model of many measuring circuits must be constructed allowing to connect in turn many measuring circuits to one measurement system and to obtain precise SDN diagnoses (Fig.2).

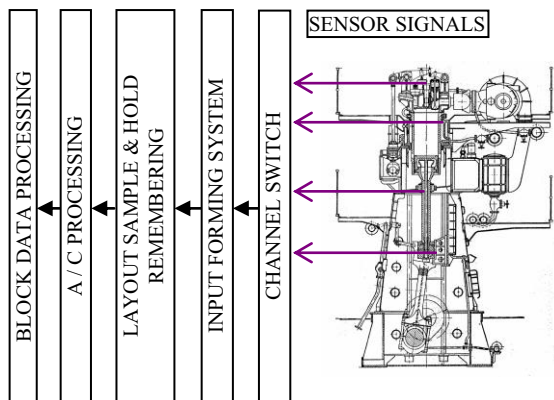


Fig.2. Block model of measuring circuits of the crankshaft-piston assembly main subassemblies

During operation of an engine equipped with SDG the durability of measurement circuit elements must be taken into account, therefore SDG may be divided into the following states of aptitude [5]:

- z_1 – active use state when SDG is in a condition of full aptitude,
- z_2 – active use state when SDG is in a condition of partial aptitude,
- z_3 – active use state when SDG is incapable of identifying the SDN current technical condition,

Therefore, it may be said [5] that probability P_1 is the probability of emitting the F^1 signals meaning the use of SDG during the z_1 state, i.e. $P_1 = P(F^1)$; $F^1 = \{z_1\}$. Probability P_2 may be treated as probability of emitting the F^2 signals meaning the use of SDG during the z_2 state, i.e. $P_2 = P(F^2)$; $F^2 = \{z_2\}$.

Probability P_3 may be treated as probability of emitting the F^3 signals meaning the use of SDG during the z_3 state, i.e. $P_3 = P(F^3); F^3 = \{z_3\}$.

4. TOPOLOGICAL MODEL

The topological diagnostic model [1] of measurement circuits of the main subassemblies of an internal combustion engine crankshaft-piston assembly (Fig.3) presents clearly the technical condition – emitted signal relations. Besides, in mapping the set of states of the main crankshaft-piston subassemblies into a set of emitted signals characterizing the states of crankshaft-piston assembly elements, one can use the conditional probabilities that the value of an emitted signal F will change when a certain state s occurs. Making use of the notion of conditional probability, from the same relations a probable conclusion can be drawn that the state s had occurred as the emitted signal F has changed.

The example (Fig.1) of a measurement report window shows that $n = 12$ emitted signal amplitudes exceeded the reference level, with $k = 2$ amplitudes very indistinct, which indicates a defect of the measuring circuit. Such observations mean that the signal emitting aptitude probability can be determined [5,6]:

$$P = (n - k)/n = 0,83 \quad (1)$$

As the example indicates a significant degree of diagnosis reliability, so it may be intuitively assumed that the measuring circuit is in the z_1 state. Then:

$$P = P_1 = p(s_2/F_1) = p(s_2) \quad (2)$$

Additionally, it is also proper to determine to what degree the presented signal emitting capability influences the reliability of assessment of the technical condition of main crankshaft-piston system subassemblies. The T. Bayes axiom on conditional probability [3,7] may be used for the purpose (Table 1).

Table 1: Method of determining the conditional probability

Measuring circuit	1	2	N
,n"	n_1	n_2	n_N
,k"	k_1	k_2	k_N
$P_1 = P(F_1)$	$\frac{n_1 - k_1}{\sum_{i=1}^N (n_i - k_i)}$	$\frac{n_2 - k_2}{\sum_{i=1}^N (n_i - k_i)}$	$\frac{n_N - k_N}{\sum_{i=1}^N (n_i - k_i)}$
$P_1 = P(F_1/s_2)$	$\frac{P(F_1) \cdot P(s_2 / F_1)}{\sum_{i=1}^N P(F_i) \cdot P(s_2 / F_i)}$	$\frac{P(F_2) \cdot P(s_2 / F_2)}{\sum_{i=1}^N P(F_i) \cdot P(s_2 / F_i)}$	$\frac{P(F_N) \cdot P(s_2 / F_N)}{\sum_{i=1}^N P(F_i) \cdot P(s_2 / F_i)}$

The probability $P(F^1/s_2)$ may be treated as the value of probability indicating to what degree a given measuring circuit can assess the technical condition of a diagnosed main crankshaft-piston subassembly.

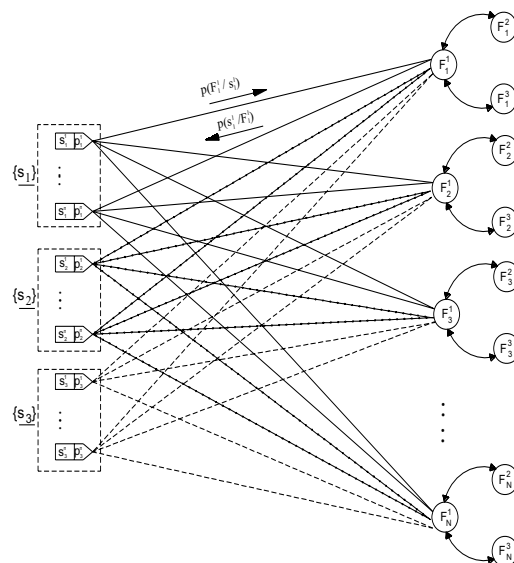


Fig.3. Topological diagnostic model of measurement circuits, where: $F_1^1, F_1^2, \dots, F_N^1$ – signals emitted from piezoelectric measuring transducers about z_1 aptitude; $F_2^1, F_2^2, \dots, F_N^2$ – signals emitted from piezoelectric measuring transducers about z_2 aptitude; F_3^1, \dots, F_N^3 – signals emitted from piezoelectric measuring transducers about z_3 aptitude; $\{s_1\}$ – state of full aptitude of a main subassembly of engine crankshaft piston assembly; $\{s_2\}$ – state of partial aptitude; $\{s_3\}$ – state of inaptitude; $p(F_1^1/s_1)$ – probability that emitted signal F_1^1 is observed on the condition that state s_1 occurs; $p(s_1/F_1^1)$ – probability that state s_1 occurs on the condition that emitted signal F_1^1 is observed.

5. CONCLUSIONS

The paper presents methods of determining conditional probabilities of aptitude of the measuring circuits diagnosing the technical condition of main subassemblies of a compression-ignition engine crankshaft-piston assembly.

As the measuring circuit wear and tear process progresses, the amplitudes of emitted signal with indistinctly exceeded reference level "k" increase, i.e. the $P(F^1/s_2)$ value decreases. Therefore, it is recommended to establish a limit level, which, when exceeded, would indicate that the measuring circuit requires repair.

BIBLIOGRAPHY

- [1] Bzura P. Diagnostic Model Of Compression-Ignition Engine Slide Bearings For Controlling The Changes Of Their State. Journal of POLISH CIMAC. - vol. 2, no.2 (2007),

- [2] Bzura P.: *Failure model of main elements of the ship engine crankshaft-piston assembly.* Journal of POLISH CIMAC. - vol. 7 , no.1 (2012).
 - [3] Bzura P.: *Reliability model of the crankshaft-piston assembly.* 38th International Scientific Congress on Powertrain and Transport Means - Warsaw 2012 - Vol.19, no.1.
 - [4] Gajek A., Juda Z.: *Czujniki.* Wydawnictwo Komunikacji i Łączności, Warszawa 2011
 - [5] Girtler J.: *Zastosowanie wiarygodności diagnozy do podejmowania decyzji w procesie eksploatacji urządzeń.* Wydział Elektroniki Wojskowej Akademii Technicznej, Warszawa 2003
 - [6] Girtler J, Kuszmider St., Plewiński L.: *Wybrane zagadnienia eksploatacji statków morskich w aspekcie bezpieczeństwa żeglugi,* Wyższa Szkoła Morska, Szczecin 2003.
 - [7] Grabski F., Jaźwiński J.: *Metody Bayesowskie.* Wydawnictwo Komunikacji i Łączności, Warszawa 2001
 - [8] Kuratle R. H. *Influencing Parameters and Error Sources During Indication on Internal Combustion Engines,* SAE Technical Paper Series 920233, Detroit 1992.
 - [9] Piotrowski J., Kostyro K.: *Wzorcowanie aparatury pomiarowej.* PWN, 2000.
 - [10] Szabatin J.: *Podstawy teorii sygnałów.* Wydawnictwo Komunikacji i Łączności, Warszawa 1982.
 - [11] Zakrzewski J.: *Czujniki i przetworniki pomiarowe.* Wydawnictwo Politechniki Śląskiej, 2004.
-

Dr. **Piotr BZURA** – lecturer in the Faculty of Ocean Engineering and Ship Technology, Gdańsk University of Technology



STRUCTURE AND ALGORITHMS OF A DIAGNOSTIC DEVICE IN A WHEELED TRACTOR

Ryszard ARENDT, Ryszard MICHALSKI

Gdańsk University of Technology, University of Warmia and Mazury in Olsztyn
ul. G. Narutowicza 11/12, 80-233 Gdańsk, fax: (+48) 58 347 24 87, email: rarendt@ely.pg.gda.pl

Summary

Diagnostic device monitors the tractor's technical condition and identifies the location of damaged components during operation. The diagnostic device detects and identifies the following types of defects: functional defects (u_f) which affect performance, exhaust defects (u_e) which increase toxic emissions and fuel consumption, defects that jeopardize driving safety (u_s), defects that affect engine performance (u_d). The key component of diagnostic device is on-board computer with touch screen, connected by USB/DeviceNet converter (master module) via the USB port. The CAN bus connects the interface module with three slave modules collecting data from sensors installed in various locations of wheeled tractor. Slave devices acted as data concentrator units. In the paper structure and basic algorithms are presented.

Keywords: wheeled tractor, algorithm, diagnostics device

STRUKTURA I ALGORYTMY URZĄDZENIA DIAGNOSTYCZNEGO CIĄGNIKÓW KOŁOWYCH

Streszczenie

Urządzenie diagnostyczne jest ukierunkowane na monitorowanie i diagnozowanie, sprowadzone do kontroli stanu technicznego i lokalizacji elementów uszkodzonych ciągnika w trakcie eksploatacji. Założono możliwość wykrywania i lokalizowania uszkodzeń podzielonych na klasy związane z następującymi skutkami: funkcjonalnymi (u_f) powodującymi ograniczenia efektywności pracy, emisijnymi (u_e) wywołującymi wzrost emisji związków toksycznych i zużycia paliwa, zagrażającymi bezpieczeństwu ruchu (u_s) ciągnika, pogarszającymi dynamikę (u_d). Podstawowym elementem diagnostycznym jest komputer pokładowy z ekranem dotykowym, połączony łączem USB z konwerterem protokołu USB na DeviceNet, pracującym jako „master”. Sieć CAN łączy konwerter z trzema urządzeniami akwizycji danych czujników zainstalowanych w wybranych punktach ciągnika kołowego. Artykuł prezentuje podstawowe algorytmy urządzenia.

Słowa kluczowe: ciągnik kołowy, algorytm, urządzenie diagnostyczne

1. INTRODUCTION

The proposed mechatronic system monitors and diagnoses the technical condition of a wheeled tractor and identifies damaged elements during the tractor's operation. The system detects and identifies defects that are classified into the following groups in view of the resulting consequences [1, 2, 7]:

- functional defects (u_f) which inhibit performance (power, torque, towing force, working speed, fuel consumption),
- exhaust defects (u_e) which increase toxic emissions and fuel consumption due to a malfunction of the fuel supply system, layout of the diesel engine and the power transmission system,
- defects that jeopardize driving safety (u_s) affecting the following tractor systems: brake, suspension, steering and lights,
- defects that affect engine performance (u_d) and driving parameters in a tractor, including

decreased acceleration, delayed response to changes in movement parameters, unequal power levels, significant loss of power and moment of force, etc.

A diagnostic device necessitates the development a system for the acquisition and processing of performance data in a wheeled tractor. Such a system consists of a large number of cable connections and an on-board computer.

The Controller Area Network is a vehicle bus standard [5, 9] which contains a detailed communication protocol and has the following features:

- it supports the development of dispersed systems operating in real time – power supply and communication subsystems are connected by network nodes;
- it is highly resistant to transmission errors;
- data transmission speed reaches 1Mb/s (CANopen) and 0.5Mb/s (DeviceNet);

- it has an open structure which supports the incorporation of new nodes;
- collective communication is based on master-slave tasking.

CANopen and DeviceNet are the most popular specialized networks based on the CAN protocol. CANopen is available as European standard EN50325-4. CANopen networks support the operation of machines and devices which are embedded systems. They are used in vehicles, in particular passenger cars, the railway industry, ships, aircraft, control systems for small objects, and they are increasingly often deployed in complex production lines. DeviceNet was developed by Honeywell in 1989 based on the CAN technology as a Smart Distributed System (SDS) standard. The DeviceNet protocol was engineered in 1994 by Allen-Bradley as a combination of the CAN protocol and the Common Industrial Protocol (CIP). SDS gained widespread popularity in the US, and it is used to automate production lines and control vehicle subassemblies.

A dispersed tractor diagnostic system was proposed due to the simplicity of cable connections and the ease of communication with the existing OBD systems. Up to 64 data acquisition nodes or two-state and analog control nodes can be used in the system. Dedicated slave nodes such as thermocouple modules and acceleration sensors can be additionally incorporated.

In networks with a DeviceNet protocol, data acquisition procedures involve two types of messages: information about input/output status (I/O messages) and general configuration data (explicit messages). There are three data exchange methods: Change of State (COS), Bit Strobe (BS) and Polling (PO). The COS mechanism uses the connection only when the status of the device has changed. A typical

COS transmission is a one-way and one-to-many transmission. Cyclic data exchange with a defined cycle repeat time is a variant of the COS mechanism. The BS master mechanism sends a strobe signal to the network. Transmitted data can be received by all network devices. Devices configured for processing BS messages send a data frame to the master device in a given sequence (based on the address). In the PO mechanism, the master device communicates cyclically with slave devices based on the indicated addresses. A slave device sends a data frame upon request from the master device.

In the CAN standard data frame with the DeviceNet protocol, 8 bytes of data are transmitted. Typical nodes support 4 sensors which process analog data into 2 bytes of data per sensor. Nodes are identified based on their Media Access Control (MAC) address. Larger data transmissions require messages from many frames or the use of other mechanisms.

This paper discusses the hardware structure, components, object data and software for the proposed diagnostic system of a wheeled tractor.

2. HARDWARE STRUCTURE OF A DIAGNOSTIC SYSTEM

The key component of the proposed diagnostic system (Fig. 1) is the Fujitsu FUTRO S100 on-board computer in shock and vibration-proof housing, with passive cooling and a 16 GB Compact Flash memory card. The computer was provided with a NVOX LCD 10" VGA/FVAT touch screen. The following software was used: Windows XP-2000, USB/DeviceNet interface module and a diagnostic program. The installed memory card supports the operation of the diagnostic device.

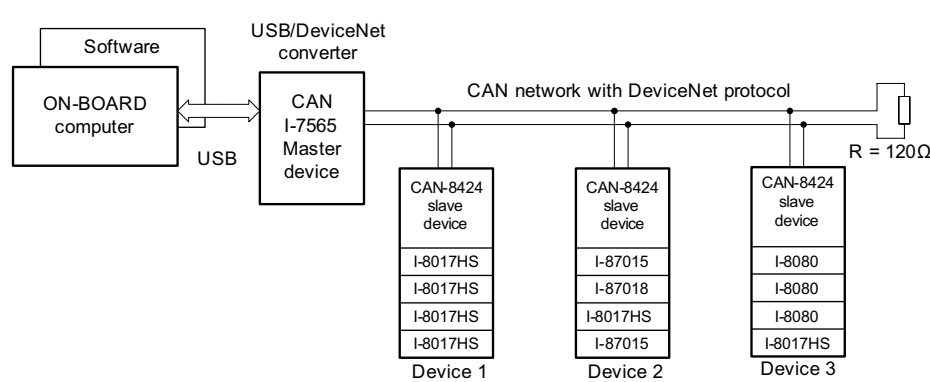


Fig. 1. Structure of a diagnostic device in a wheeled tractor

The computer was connected to the I-7565USB/DeviceNet master device via the USB port. The CAN bus connects the interface module with three slave devices collecting data from sensors installed in various locations of a wheeled tractor. Slave devices act as data concentrator units. Every device has a unique ID and is equipped with 4 input

(output) cards which correspond to the range and type of the measured signals.

ICP DAS network devices and data acquisition modules with high resistance to shock and temperature change (-25° ÷ +75°C) were used. The diagnostic device was designed for use with 4 types of data acquisition modules:

- I-8017HS – analog input module which supports the acquisition of data from 8 analog signals ($\pm 10V$, $\pm 5V$, $\pm 2.5V$ and $\pm 20mA$) or 16 analog signals excluding negative values;
- I-87015 – analog input module of RTD sensors which supports the acquisition of data from 7 analog signals in resistance sensors of various type and temperature range; Pt100 sensors with $0^\circ \div +200^\circ C$ temperature range were used;
- I-87018 – analog input module which supports the acquisition of data from 8 analog signals with varied range, including the output voltage range of thermocouples; type K thermocouples with $-270^\circ \div +1372^\circ C$ temperature range were used;
- I-8080 – pulse input module which supports the acquisition of data from 4 (8) two-state signals, up/down pulse counting and frequency measurement. The module was used to measure the rotational speed of shafts with the involvement of pick-up sensors.

The proposed diagnostic device is a research model whose data acquisition capability exceeds the needs of a standard diagnostic device in a wheeled tractor. The maximum quantity of available analog is limited to 144 sensors. Data transmission speed in the CAN network with the DeviceNet protocol reaches 500kb/s.

Many of the interesting features of the DeviceNet protocol described in the introduction have been lost due to high data concentration in three data acquisition devices. COS, BS and PO communication mechanisms for three devices are capable of sending 3 frames of 8 bytes each, i.e. data from only 12 sensors. For this reason, communication mechanisms based on explicit messages had to be used in the proposed diagnostic program.

3. STRUCTURE OF THE DIAGNOSTIC INTERFACE TOOL IN A WHEELED TRACTOR

The following diagnostic procedures were deployed at the current phase of development:

- on-line diagnostics – cyclic operation of the data acquisition program with data readout from sensors at intervals of $T = 1s$ (default value), diagnosis, error code generation;
- vibration tests – acquisition of data files from acceleration sensors, the use of fast Fourier transform and dedicated diagnostic procedures;
- engine performance tests – acquisition of data files from shaft speed sensors, determination of speed and acceleration characteristics under given operating conditions based on the knowledge of engine performance diagnostics;

- steering system tests – controlling steering clearance.

The main window of the diagnostic program is presented in Fig. 2.

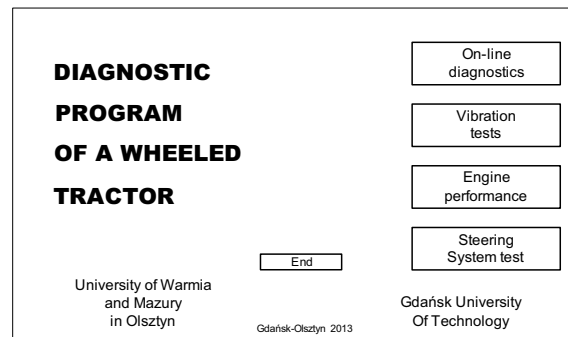


Fig. 2. Main window of the diagnostic program

The data acquisition system can be configured and diagnostic and testing procedures can be initiated in the respective diagnostic or test window.

3.1. Configuration subprogram

In the first stage of configuring the data acquisition system based on CAN-8424 network devices, hardware parameters are defined and the transmitted measurement data is organized with the use of the SlaveUtility (ICP DAS) application. The user defines the types of modules installed in successive punch-down blocks of the CAN device, the functions of each input and, optionally, the sensitivity ranges of module inputs. Data inputs (connected sensors) and the readout sequence are defined in the Assembly Object layer of the CAN network. One data frame can contain up to 8 bytes, and up to 16 frames can be described. Data selected by the user is saved in an Electronic Data Sheet (EDS) file which is used to configure the CAN-8424 module. A text file is additionally generated for the user.

Read data contains measured parameters – 2 bytes per measurement. The configuration subprogram assigns the name of the measuring element to the measurement, it converts bytes to numeric values in MKS units and assigns the name of the measuring element to the calculated variable. An unnamed field implies that a given measurement was omitted.

The user enters the following data in the configuration subprogram (Fig. 3):

- MAC address of a data acquisition device,
- number of lines of transmitted measurement data,
- names of measuring devices.

The designed subsystem also features a data configuration option based on connected data frames of different device modules for 16 to 48 byte transmissions. The above option relies on the Application Object layer of the CAN network.

Subject to module type, successive inputs and the assigned bytes are displayed on the screen. When a name is assigned to an input, a given measurement is taken into account, and its physical value is computed. The above option was used to configure testing subprograms.

DEVICE CONFIGURATION

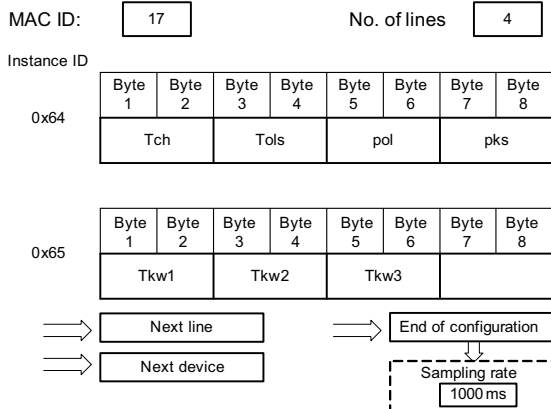


Fig. 3. Screenshot of the subprogram for configuring measuring data

3.2. Conversion of measurement data

Measurement modules have different data representations in bytes. The following information should be taken into account during conversion:

- number of data bytes – 2, 4 and 6 bytes are used,
- number of bits in two bytes of data – 14 and 16 bits are used,
- maximum range of data in 2 bytes, e.g. 7FFFh, 1FFFh,
- minimum range of data, e.g. 0000h, for a negative range – 2000h,
- maximum and minimum physical ranges of a sensor which correspond to data ranges in bytes,
- effective measuring range of $4 \div 20\text{mA}$, for the applied range of $\pm 20\text{mA}$,
- conversion of physical units.

Eleven computing procedures have been developed for the conversion of measurement data. The procedure is selected based on the name of the measuring device.

The measured parameters of a wheeled tractor can be viewed during the online diagnostic process (Fig. 4).

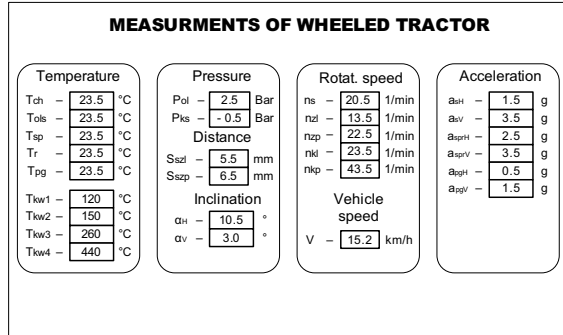


Fig. 4. Window displaying the measured parameters of a wheeled tractor

Computed parameter values which are not available during direct measurement (another window) can also be previewed.

4. SELECTED PROGRAM ALGORITHMS

A real-time clock controls data readout in the online diagnostic process. The data readout procedure is called at time intervals T . Bytes written in a table are converted into physical values that are assigned to variables named after the measuring sensor. Physical values of performance variables which are not available during direct measurements are computed based on registered data and the parameters stored in memory. Registered and computed values are used in the diagnostic process, and they may be displayed on the screen. Cause-and-effect relationships between a fault and its symptoms are identified as defects and are communicated by the respective error codes.

4.1. Real-time control

In the Windows environment, real-time control is problematic due to difficulties with stability and sampling frequency. The available tools in popular programming languages do not support stable and precise time control. The *WinApi* library offers the only solution to the problem.

A separate time control option with the highest priority (*tpHighest*) has been introduced to guarantee the accuracy of time intervals between successive measurements. The accuracy of intervals between measurement samples was maximized with the use of the *timeBeginPeriod* function which increases the precision and resolution of the Windows timer (this function is used in real-time applications and multimedia systems). The value of the expected stable timer resolution in milliseconds is the function parameter. The function is called directly before the use of other counting functions and measurements that require a stable real-time clock.

Accurate time measurements are performed with the involvement of the *QueryPerformanceCounter* function which returns the number of the clock cycle performed by the processor as a parameter and the

QueryPerformanceFrequency which indicates the frequency of clock cycles.

A waitable timer object for synchronizing timing tasks has been used to control the passage of time and the arrival of a specified due time. When the "time synchronization object" has been created, the user can control the expiry of successive time intervals. Time intervals can be set in accordance with Windows instructions with a minimum step of 100 ns.

4.2. Data readout procedure

The MAC address of the device and the number of lines (successive Instance ID numbers, beginning from 0x64) are specified in the Assembly Object layer of the configuration subprogram in the data acquisition system. Data can be cyclically read from the loop with the use of explicit messages.

The data readout procedure is called cyclically at intervals T which are specified in the configuration subprogram. Two bytes of data are combined to form words, and they are entered into the table. Identical indicators are found in the table specifying the names of measurement sensors in the configuration subprogram.

4.3. Data conversion procedure

The table specifying the names of measurement sensors is reviewed. Elements without names are omitted. The procedure assigned to a named element is called. The table index also indicates the source of measurement data which is sent to the procedure. The computed physical value of a parameter is assigned to the variable named after the sensor.

4.4. Procedure of computing physical values which are not available during direct measurements

Not all physical parameters are measured directly, and they may have to be computed independently. The most important values are: N_e – effective engine power and M_e – effective torque. Parameters were computed mechanically based on formulas (1) ÷ (5):

$$V = \frac{\Pi n_k r_d}{30} [\text{m/s}], \quad (1)$$

$$a = \frac{\Delta V}{\Delta t} [\text{m/s}^2], \quad (2)$$

$$F = ma [\text{N}], \quad (3)$$

$$N_e = FV [\text{kW}], \quad (4)$$

$$M_e = \frac{Fr_d}{i\eta_c} [\text{Nm}], \quad (5)$$

where: V – velocity read from a GPS receiver, n_k – average velocity of drive wheels, a – acceleration, F – inertial force, η_c – total efficiency of the power

transmission system, $i = \frac{\Pi r_d n_s}{30V}$, m – tractor mass, r_d – rolling radius, n_s – rotational speed of engine shaft, i – overall gear ratio.

The percentage relative slip ratio of rear axis wheels S_{ot} is determined based on the following formula:

$$S_{ot} = \left(\frac{n_{kl} + n_{kp}}{n_{zl} + n_{zp}} - 1 \right) 100\%. \quad (6)$$

The below equation is used to calculate slip based on GPS data:

$$s = \frac{V - \omega R}{V}, \quad (7)$$

where: $\omega = 2\Pi n_k / 60$ – angular velocity of drive wheels, ωR – circumferential speed of the drive wheel tire.

4.5. Diagnostic procedure

Parameter values are analyzed at various engine states. During effective tractor operation, the measured values should fall within the given intervals. A defect changes the value of measured parameters and produces a "diagnostic symptom" [3, 4].

In the proposed diagnostic system, a defect is defined as a destructive event which deteriorates tractor performance and effectiveness [6, 7]. A diagnostic system should effectively identify all defects. A tractor's fault S_N is caused by one of the four categories of defects $\{u_f, u_e, u_s, u_d\}$, and the above is expressed by formula (8):

$$S_N \Rightarrow \{u_f \cup u_e \cup u_s \cup u_d\} \neq 0. \quad (8)$$

The diagnostic process verifies the relationship R between a defect (fault) and a diagnostic symptom. Specific defects (9) or a possible set of defects (10) (one-to-many relationship) can be identified for cause-and-effect relationships between a fault $f_i \subset F$ and symptoms s_j which are represented by set S based on formula (9) or (10):

$$R : \{s_j\} \Rightarrow f_i, \quad (9)$$

$$R : \{s_j\} \Rightarrow \{f_i\}_{kj}, \quad (10)$$

Defect sets are represented by error codes displayed on the screen of a tractor's diagnostic device.

Diagnostic tests are presently being carried out, and cause-and-effect relationships between a defect (fault) and a symptom (values of a selected set of physical parameters) are identified in a wheeled tractor.

5. CONCLUSIONS

The proposed diagnostic system for a wheeled tractor was developed with the involvement of the CAN system and the DeviceNet protocol engineered in 2008-2010. The construction of a diagnostic

device was fraught with problems due to incomplete ICP DAS documentation.

The developed device is currently being tested in a wheeled tractor to identify cause-and-effect relationships between damage symptoms and four groups of defects. Vibration tests will support the determination of the effective band of registered frequencies – testing time influences the evaluation of the lowest frequencies, whereas sampling rate affects the highest analyzed vibration frequencies.

Acknowledgments: This study was supported by research grant No. N N504 513740 from the Ministry of Science and Higher Education.

REFERENCES

- [1] Arendt R., Michalski R.: *Struktura systemu diagnostycznego ciągnika kołowego*. Zeszyty Naukowe Instytutu Pojazdów, 2012, nr 3 (89).s.5-12,
- [2] Arendt R., Michalski R.: *Functional structure of diagnostics system for wheeled tractors*. Pomiary Automatyka Robotyka, 2012, nr 12, s. 117-120.
- [3] Kościelny J. M.: *Diagnostyka zautomatyzowanych procesów przemysłowych*. Wyd. Akademicka Oficyna Wydawnicza EXIT; Warszawa 2000.
- [4] Korbicz J., Kościelny J. M., Kowalcuk Z., Cholewa W.: *Diagnostyka procesów, modele, metody sztucznej inteligencji, zastosowania*. WNT, Warszawa 2002.
- [5] Merkisz J., Mazurek S.: *Pokładowe systemy diagnostyczne pojazdów samochodowych*. WKŁ, Warszawa 2000.
- [6] Michalski R.: *Diagnostyka maszyn roboczych*. Wyd. ITE Radom – Olsztyn, 2004.
- [7] Michalski R., Gonera J., Janulin M., Arendt R.: *Structural analysis of wheeled tractor oriented towards damage diagnostics*. Monografie, studia, rozprawy “Selected problems of mechanical engineering and maintenance” M29, Politechnika Świętokrzyska, Kielce 2012 s. 16-30.
- [8] Natke H. G., Cempel C. *Model-Aided Diagnosis of Mechanical Systems: Fundamentals, Detection, Localization, Assessment*. Berlin. Springer-Verlag 1997.
- [9] Niziński S., Wierzbicki S.: *Zintegrowany system informatyczny sterowania pojazdów*. Diagnostyka, nr 30 t.2/2004. s. 47-52.
- [10] Zimmermann W., Schmidgall R.: *Magistrala danych w pojazdach. Protokoły i standardy*, WKiŁ 2008.



dr hab. inż. Ryszard Arendt is a professor of the Faculty of Electrical and Control Engineering in Gdańsk University of Technology, G. Narutowicza 11/12, 80-233 Gdańsk, Poland. E-mail: rarendt@ely.pg.gda.pl. His current research interests are: an application of artificial intelligence in automation of ship systems design, mechatronic systems and diagnostic of control elements and systems.



prof. dr hab. inż. Ryszard Michalski is a professor of the Faculty of Technical Sciences in University of Warmia and Mazury in Olsztyn, Oczapowskiego 11, 10-736 Olsztyn, Poland. E-mail: ryszard.michalski@uwm.edu.pl. His current research interests are: technical diagnostic, reliability, repair engineering and system analysis of vehicle and working machines exploitation.

SELECTION OF DIAGNOSTIC FUNCTIONS IN A WHEELED TRACTOR

Ryszard MICHALSKI, Ryszard ARENDT

University of Warmia and Mazury in Olsztyn, Gdańsk University of Technology
ul. Oczapowskiego 11, 10-736 Olsztyn, adres, fax: (+48) 89 523 34 63, email: Ryszard.michalski@uwm.edu.pl

Summary

In a classical approach to damage diagnosis, the technical condition of an analyzed machine is identified based on the measured symptoms, such as performance, thermal state or vibration parameters. In wheeled tractor the fundamental importance has monitoring and diagnostics during exploitation concerning technical inspection and fault element localizations. The main functions of a diagnostic system are: monitoring tractor components which affect operation, safety, performance parameters and exhaust gas emissions; registering information about component damage; registering performance parameters at the moment of damage. In the paper research problem, methodology and achieved results are presented.

Keywords: wheeled tractor, algorithm, diagnostics device

DOBÓR FUNKCJI URZĄDZENIA DIAGNOSTYCZNEGO CIĄGNIKA KOŁOWEGO

Streszczenie

W klasycznych metodach diagnozowania uszkodzeń maszyn wykorzystuje się odwzorowanie stanu technicznego obserwowanej maszyny poprzez mierzony symptom np.: efektywność pracy, stan cieplny, drganiowy. W ciągniku kołowym podstawowe znaczenie ma monitorowanie i diagnozowanie w toku eksploatacji, sprowadzone do kontroli stanu technicznego i lokalizacji elementów uszkodzonych. Podstawowe funkcje urządzenia diagnostycznego to: monitorowanie elementów ciągnika kołowego mających wpływ na funkcjonowanie, bezpieczeństwo, dynamikę i poziom emisji toksycznych składników spalin; zapis informacji o uszkodzeniach elementów ciągnika; zapis informacji o parametrach ciągnika w chwili uszkodzenia. W artykule przedstawiono problem badawczy, zastosowane metody i uzyskane wyniki.

Słowa kluczowe: ciągnik kołowy, algorytm, urządzenie diagnostyczne

1. INTRODUCTION

The performance of a wheeled tractor is influenced by various factors, including the condition of mechanical, electrohydraulic and electromechanical systems which affect engine supply and the efficiency of the power transmission system. The choice of adequate steering and control methods also influences tractor operation.

Damage of complex tractor systems impairs system effectiveness, performance and operating safety. Failure mode and effects analyses as well as failure mode, effects and criticality analyses should be performed regularly in tractors to guarantee optimal performance [5, 6, 7]. Complex mechanical systems in wheeled tractors require increasingly sophisticated research methods to detect defects during design and operation.

According to Machinery Directive 93/68/EEC, a machine's technical design has to be evaluated in view of durability and susceptibility to damage. Those issues are often addressed separately at the stage of tractor design and construction due to:

- limited knowledge about modeling principles for vehicle units which are designed for operation in a changing environment,
- absence of damage analysis methods which are based on maintenance engineering,
- absence of methods for acquiring information about damage sustained during operation and the use of the resulting knowledge in machine design.

In a classical approach to damage diagnosis, the technical condition of an analyzed machine is identified based on the measured symptoms, such as performance, thermal state or vibration parameters [8]. The quality of the diagnostic process is determined by the accuracy with which damage is modeled based on the observed symptoms. They can be identified experimentally or by theoretical analysis which relies on functional models (e.g. frequency characteristics) and structural models (changes in nonlinearity, changes in weight, rigidity and attenuation parameters).

During a technical inspection, the operation and performance of a wheeled tractor is diagnosed, and the location of damaged components is identified.

Periodic inspections in service stations do not always deliver optimal results due to limited service time, restricted scope of inspection and the absence of working load during the diagnostic process.

A general structural concept of a mechatronic system in a wheeled tractor (MSDC) was proposed by [3] for diagnosing defects which affect operation, toxic gas emissions safety and performance. The structure of the MSDC [1], the damage simulation model and the diagnostic relations model were developed as part of research project No. N N504513740.

This paper discusses the main functions of a mechatronic diagnostic system in a wheeled tractor, the relations between system elements, types of diagnostic algorithms and a data communication system with a data bus.

2. SPECIFICATION

A mechatronic diagnostic system of a wheeled tractor (MSDC) can be represented by the following relationship:

$$\text{MSDC} = [\text{PI}, \text{PS}, \text{PZ}, \text{PP}, \text{PD}, \text{CK}, \text{R}_D], \quad (1)$$

where : PI – computer subsystem,

PS – control subsystem,

PZ – power supply, data communication and material supply system,

PP – working and auxiliary process subsystem,

PD – diagnostic subsystem,

CK – wheeled tractor,

R_D – diagnostic and control relations.

The main functions of MSDC are:

- monitoring components which affect the operation, safety, performance and toxic gas emissions of a wheeled tractor,
- recording information about component failures,
- recording information about tractor parameters at the moment of damage,
- communicating defects to the operator.

A tractor's diagnostic subsystem has the following elements:

$$\text{PD} = [\text{E}_d, \text{C}_d, \text{S}, \text{M}_d, \text{I}_z, \text{O}_p, \text{A}_d, \text{R}_d], \quad (2)$$

where: E_d – set of elements which are diagnosed in a selected monitoring function,

C_d – sensor set,

S – electronic control system (controller),

M_d – data bus,

I_z – system for the visualization of diagnostic data,

O_p – software,

A_d – diagnostic algorithms,

R_d – diagnostic relations.

A diagnostic subsystem in a wheeled tractor:

- monitors a tractor's operating state,
- monitors performance parameters,
- generates error (fault) codes,
- monitors instantaneous fuel consumption,
- registers operating time,
- registers GPS data (map, trace, speed, altitude).

The list of parameters monitored by a wheeled tractor's diagnostic system is presented in Table 1.

Table 1. Diagnostic parameters of a wheeled tractor

No.	Subassembly	Diagnostic parameter X(t)
1.	Engine	<p>T_c – coolant temperature Coolant temperature is measured by a cooling system sensor installed in the area of the coolant pump. $T_c > T_{c\max}$ indicates:</p> <ul style="list-style-type: none"> - engine overheating due to overload, - coolant pump failure, - low coolant level, - thermostat failure, - radiator failure, - cooling system airlock. <p>T_{oil} – engine oil temperature Engine oil temperature is measured directly by a sensor installed in the lubrication system. $T_{oil} > T_{oil\max}$ indicates:</p> <ul style="list-style-type: none"> - engine overheating due to overload, - excessive engine speed under given operating conditions /inadequate setting of the power transmission system, - low engine oil level, - engine seizure. <p>T_{ex1} – exhaust gas temperature in cylinder 1, T_{ex2} – exhaust gas temperature in cylinder 2, T_{ex3} – exhaust gas temperature in cylinder 3, T_{ex4} – exhaust gas temperature in cylinder 4. Exhaust gas temperature is measured by sensors installed in the exhaust manifold by every cylinder.</p>

		<p>$T_{exi} > 1.15 \cdot T_{exavr}$ or $T_{exi} < 0.85 \cdot T_{exavr}$, where: $T_{exavr} = \frac{1}{j} \sum_{i=1}^j T_{exi}$</p> <p>indicates injector system failure or abnormal pressure in the i^{th} cylinder.</p> <p>p_{oil} – oil pressure.</p> <p>Oil pressure is measured directly by the pressure sensor. $p_{oil} > p_{oil\max}$ is indicative of:</p> <ul style="list-style-type: none"> - oil pump failure. <p>$p_{oil} < p_{oil\min}$ indicates:</p> <ul style="list-style-type: none"> - oil pump failure, - low oil level, - oil leak, - inadequate oil parameters, - significant fuel or coolant leak into engine oil, - main bearing failure, - oil filter blockage. <p>p_{sm} – suction manifold pressure.</p> <p>Pressure is measured directly by a sensor in the engine's suction manifold.</p> <p>$p_{sm} < p_{sm\min}$ indicates:</p> <ul style="list-style-type: none"> - air filter blockage, - blockage of the air supply conduit. <p>n_{eng} – crankshaft speed.</p> <p>a_{eng} – engine vibration level.</p> <p>Engine vibration levels are measured directly by a biaxial vibration sensor.</p> <p>$a_{eng} > a_{eng\max}$ is indicative of engine failure.</p> <p>N_e – power measurement.</p> <p>M_e – torque measurement.</p> <p>MECHANICAL METHOD:</p> <ol style="list-style-type: none"> 1. $V = \frac{\Pi n_k r_d}{30}$ [m/s]. 2. $a = \frac{\Delta V}{\Delta t}$ [m/s²]. 3. $F = m a$ [N]. 4. $N = F V$ [kW]. 5. $M_s = \frac{F r_d}{i \eta}$ [Nm]. <p>$i = \frac{\Pi r_d n_{eng}}{30 V}$,</p> <p>where: r_d – rolling radius, n_{eng} – engine speed, i – overall gear ratio, Power and torque characteristics as a function of speed.</p>
2.	Gearbox	<p>a_{gbx} – vibration levels in gearbox and reduction gear.</p> <p>Vibration levels are measured directly by a biaxial vibration sensor installed on gearbox housing. $a_{gbx} > a_{gbx\max}$ is indicative of gearbox or reduction gear failure.</p> <p>T_{gbx} – gearbox temperature.</p> <p>Gearbox temperature is measured directly by a sensor installed on gearbox housing. $T_{gbx} > T_{gbx\max}$ indicates gearbox failure or low gearbox oil level.</p>
3.	Reduction gear	<p>a_{rgx} – vibration levels in gearbox and reduction gear.</p> <p>Vibration levels are measured directly by a biaxial vibration sensor installed on gearbox housing. $a_{rgx} > a_{rgx\max}$ is indicative of gearbox or reduction gear failure.</p> <p>T_{rgx} – reduction gear temperature.</p> <p>Reduction gear temperature is measured directly by a sensor installed on gearbox housing. $T_{rgx} > T_{rgx\max}$ indicates reduction gear failure or low oil level in reduction gear.</p>
4.	Final drive and	<p>a_{fd} – vibration level in final drive.</p> <p>Vibration levels are measured directly by a biaxial vibration sensor installed in the final</p>

	differential	drive. $a_{fd} > a_{fd\max}$ is indicative of final drive failure. T_{fd} – final drive temperature. Final drive temperature is measured directly by a sensor installed on final drive housing. $T_{fd} > T_{fd\max}$ is indicative of final drive failure or low oil level in the final drive.
5.	Left hub reduction gear	n_{rgl} – left wheel speed. Wheel speed is measured directly by a speed sensor. When the differential is locked and the clutch is disengaged, $n_{rgl} < \frac{n_{eng}}{i}$ is indicative of power transmission failure.
6.	Right hub reduction gear	n_{rgr} – right wheel speed. Wheel speed is measured directly by a speed sensor. When the differential is locked and the clutch is disengaged, $n_{rgr} < \frac{n_{eng}}{i}$ is indicative of power transmission failure.
7.	Steering system	φ_{sa} – steering angle. The steering system's response to a given wheel angle is determined.
8.	Braking system	S_{bl} – distance between brake shoes in the left wheel. S_{br} – distance between brake shoes in the right wheel. The distance between brake shoes is measured directly by distance sensors. $s_{bl} \leq s_{bl\min}$ or $s_{br} \leq s_{br\min}$ is indicative of break shoe failure.
9.	Location	α – vehicle tilt angle. The tilt angle is measured directly by an inclinometer.
10.	Front axle wheels	n_{fwr} – right wheel speed. n_{fwl} – left wheel speed. s_{fw} – relative slip of drive wheels (indirect measurement). Rotational speed of rear right n_{wr} and left n_{wl} wheels. s_{rel} – relative slip of rear wheels [%] (indirect measurement); if $n_{fwl} + n_{fwr} < n_{rgl} + n_{rgr}$, then $s_{rel} = \left(\frac{n_{fwl} + n_{fwr}}{n_{rgl} + n_{rgr}} - 1 \right) \cdot 100\%$ if $n_{fwl} + n_{fwr} \geq n_{rgl} + n_{rgr}$, then $s_{rel} = 0\%$ Determination of slip based on GPS data: $\omega = \frac{2\pi \cdot n_{eng}}{60}$ – angular velocity, V – vehicle speed given by GPS receiver, $\omega \cdot R$ – wheel circumferential speed, $s = \frac{V - \omega \cdot R}{V}$, $s > 0$ – braking slip, $s < 0$ – acceleration slip, $s = 0$ – slip-free driving, $s = 1$ – wheel lock.

3. DIAGNOSTIC SYSTEM HARDWARE

The key component of the proposed diagnostic system (Fig. 1) is an on-board computer in shock and vibration-proof housing, with a touch screen and passive cooling. The computer is connected to a USB/DeviceNet protocol converter (extended CAN protocol) via the USB port. The CAN bus connects the interface module with three slave devices collecting data from sensors installed in various locations of a wheeled tractor. Every module has a unique ID and an individual data processing mode. Data transmission speed in the CAN network with the DeviceNet protocol reaches 500kb/s.

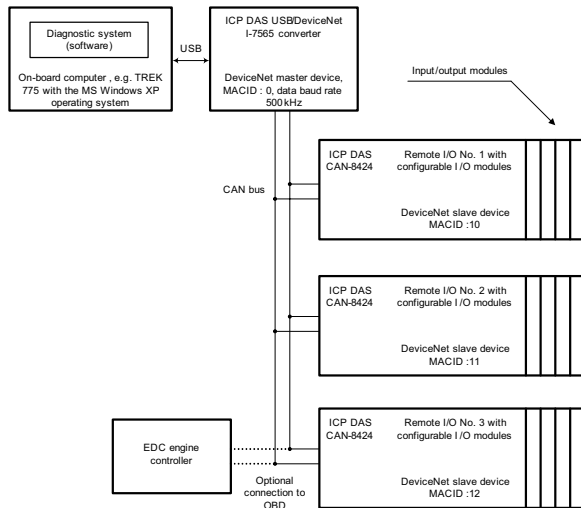


Fig. 1. Structure of the computer subsystem in a diagnostic device

The first I/O module has the highest data acquisition speed, and it supports rotational speed sensors (pick-up pulse sensors) and acceleration sensors which diagnose vibration levels in a tractor. The first I/O module also collects information about the instantaneous position of a rotating shaft and control voltage for electrostatic injector valves in the CommonRail system.

The second I/O module has low (average) data acquisition speed. It collects information about the following operating parameters: pressure, fluid levels, voltage and current values. One of the four module cards controls actuating elements during the performance of test programs and during failures.

The third I/O module has low data acquisition speed. It supports temperature sensors (Pt-100) in selected engine locations and exhaust gas temperature sensors (thermocouple sensors) in each cylinder. Due to low variations in time constants, measurements are repeated up to several times per second. One of the module cards diagnoses voltage and current data in electrical circuits.

4. DIAGNOSTIC SYSTEM SOFTWARE

The system operates in the Windows XP (optionally Win98/Win2000/WinNT) environment. A corresponding driver has to be installed for the USB/DeviceNet converter. A special application has been developed for the DeviceNet device in the

Windows environment for configuring the inputs and outputs of all extension modules (Fig. 2).

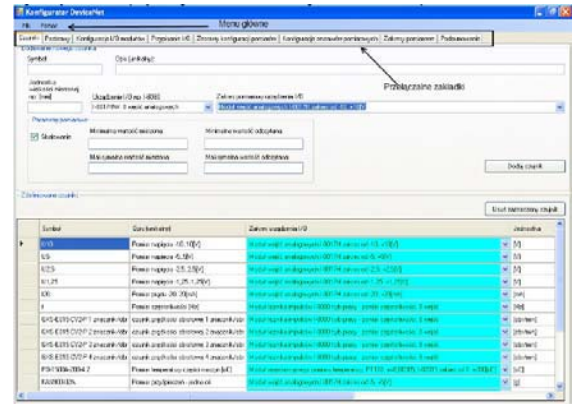


Fig. 2. Main window of the KONFIGURATOR application

The KONFIGURATOR application creates and saves files (XML and XSD) which describe the structure of the DeviceNet network based on ICP DAS CAN-8424 slave devices and an ICP DAS DeviceNet I-7565-DNM master device. Configuration data and the remaining information is saved in XML files. XML files contain data, whereas data structure is written in XSD files. XML and XSD are text files which can be viewed in any text editor such as the notepad. Configuration data used in the measurement system is also registered, including the type of I/O devices (voltage, current, frequency input and output signals) installed in CAN-8424 slots. Device inputs are configurable. The main configuration parameter is the measurement range which is set for all system inputs. Additional parameters are collected from external devices connected to I/O modules. The application has been developed for a linear data processing system.

Additional information includes: measurement kits identifying I/O devices which are installed in slots and which participate in a given measurement within the set time intervals (measurement frequency). The automatic measurement option is activated in a given measurement kit to identify the I/O device and measurement frequency. The following measurement kits can be developed for different diagnostic strategies:

- standard kits for detecting failures,
- dedicated kits for identifying possible defects, activated when failure of a tractor element or subassembly is suspected.

DeviceNet hardware of the proposed system is presented in Fig. 1. A mechatronic diagnostic system collects and processes data in real time. The diagnostic device collects and processes data at time intervals T , it computes state variables for the applied models, activates diagnostic procedures, the keyboard operating procedure and diagnostic signal circuits. Real-time operation implies that the total computer operating time dedicated to data acquisition and other processes is shorter than the adopted time interval T . The purpose and priority of

procedures in the software developed for the diagnostic device is presented in Table 2.

Table 2. Diagnostic software procedures

No.	Procedure	Priority
1.	Collection of measurement data, generation of control signals	I
2.	Keyboard (touch screen) operation, program switching to dedicated diagnostic procedures	II
3.	Fast Fourier Transform (FFT)	III
4.	Determination of angular acceleration of the crankshaft	IV
5.	Determination of selected state variables of diagnostic models	V
6.	Diagnostic procedures	VI
7.	Diagnostic state signaling	VII
8.	Other procedures	VIII

Data collection and control signal generation procedures have the highest priority, and they are initiated by a signal from the computer clock. A signal from the internal clock interrupts all lower priority procedures and initiates data collection. The diagnostic device operates at time intervals T (default value = 1 s) and selected measurements and numerical calculations are performed cyclically. The time interval is set in view of the number and frequency of measurements, data transmission speed in the CAN network, the number and complexity of diagnostic procedures.

After moment t_k , the procedure of cyclic data readout from the first module is initiated, and data is collected from speed sensors, shaft position sensors, acceleration sensors and injector valve voltage sensors (cyclic message ID-I). An n number of moments $t_1, t_2, t_3 \dots$ during which measurement parameters are read was set in interval T_I ; $T_I < T$. The transmission of data from the first module is completed within approximately $t_{pl} = 0.143$ ms. The data acquisition process is presented in a time diagram in Fig. 3.

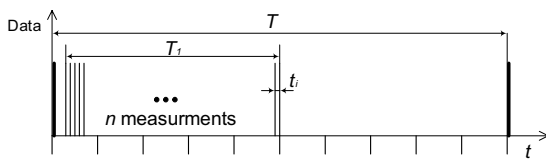


Fig. 3. Time diagram of data acquisition in a diagnostic system; bold line – overall data transmission time, thin line – time of data transmission from module I, T – time of diagnostic system operation, t_i – one cycle of data readout from module I

4. CONCLUSIONS

The discussed functions of a mechatronic diagnostic device include a set of monitored tractor elements, sensors, a system controlling the acquisition and processing of data, a system for

visualizing diagnostic data, hardware and software components and diagnostic algorithms.

The key component of the proposed diagnostic system is an on-board computer with a touch screen which is connected to a USB/DeviceNet protocol converter (extended CAN protocol) via the USB port. The CAN bus connects the interface module with three slave devices collecting data from sensors installed in various locations of a wheeled tractor. Every module has a unique ID and an individual data processing mode. Data transmission speed in the CAN network with the DeviceNet protocol reaches 500kb/s.

The KONFIGURATOR application creates and saves files (XML and XSD) which describe the structure of the DeviceNet network based on ICP DAS CAN-8424 slave devices and an ICP DAS DeviceNet I-7565-DNM master device. Configuration data and the remaining information is saved in XML files. XML files contain data, whereas data structure is written in XSD files.

REFERENCES

- [1] Arendt Ryszard, Michalski Ryszard: *Struktura systemu diagnostycznego ciągnika kołowego*. Zeszyty Naukowe Instytutu Pojazdów Politechniki Warszawskiej. Warszawa 3(89)/2012 pp. 5-12.
- [2] Arendt R., Michalski R.: *Functional structure of diagnostics system for wheeled tractors*. Pomiary Automatyka Robotyka, 2012, nr 12, pp. 117-120.
- [3] Michalski R.: *Mechatroniczny system monitorowania stanu ciągnika kołowego*. Biuletyn Wojskowej Akademii Technicznej. Warszawa. Vol.LX 1(661) 2011, pp. 221-230.
- [4] ICP DAS User's manual, DeviceNet Slave Device, CAN-8x24, Version 2.0, Aug.2007,
- [5] PN- IEC- 812: 1994. *Techniki analizy nieuskadzalności systemów*. Procedura analizy rodzajów i skutków uszkodzeń.
- [6] Michalski R.: *Diagnostyka maszyn roboczych*. Wyd. ITE Radom – Olsztyn, 2004.
- [7] Michalski R., Gonera J., Janulin M., Arendt R.: *Structural analysis of wheeled tractor oriented towards damage diagnostics*. Monografie, studia, rozprawy "Selected problems of mechanical engineering and maintenance" M29, Politechnika Świętokrzyska, Kielce 2012 s. 16-30.
- [8] Natke H. G., Cempel C. *Model-Aided Diagnosis of Mechanical Systems: Fundamentals, Detection, Localization, Assessment*. Berlin. Springer-Verlag 1997.

dr hab. inż. Ryszard ARENDT is a professor of the Faculty of Electrical and Control Engineering in Gdańsk University of Technology, G. Narutowicza 11/12, 80-233 Gdańsk, Poland. E-mail: rarendt@ely.pg.gda.pl. His current research interests are: an application of artificial intelligence in automation of ship systems design, mechatronic systems and diagnostic of control elements and systems.

prof. dr hab. inż. Ryszard MICHALSKI is a professor of the Faculty of Technical Sciences in University of Warmia and Mazury in Olsztyn, Oczapowskiego 11, 10-736 Olsztyn, Poland. E-mail: ryszard.michalski@uwm.edu.pl. His current research interests are: technical diagnostic, reliability, repair engineering and system analysis of vehicle and working machines exploitation.



THE IMPACT OF ROTATIONAL SPEED SYNCHRONISATION OF EXCITERS ON THE DYNAMICS OF A VIBRATING SCREEN SIEVE

Janusz ZACHWIEJA

University of Technology and Life Sciences in Bydgoszcz, Faculty of Mechanical Engineering, Bydgoszcz

Summary

In the paper the results of examinations and numerical analysis of the vibrating screen sieve dynamics are presented. The working movement of the sieve is forced by one or two inertial exciters. They should display a self-synchronization feature. Since such self-synchronization effect is not always achieved, therefore the sieve vibration directions do not coincide with directions of loads transferred by the vibration isolators. In such case the frequencies of forced vibrations may be close to free vibration frequency for a given modal form and the system may work in resonance conditions.

Keywords: free vibration, resonance frequencies, self-synchronization of excitation

WPŁYW SYNCHRONIZACJI PRĘDKOŚCI OBROTOWEJ WZBUDNIKÓW NA DYNAMIKĘ SITA PRZESIEWACZA WIBRACYJNEGO

Streszczenie

W pracy przedstawione zostały wyniki badań oraz analiza numeryczna dynamiki sita przesiewacza wibracyjnego. Tego rodzaju maszyna modelowana jest zazwyczaj jako układ dyskretny o jednym stopniu swobody. Jego drgania mają charakter nadrezonansowy. Praktyka pokazuje jednak, że szereg efektów występujących podczas pracy przesiewacza można解释ć jedynie po przyjęciu modelu wielorezonansowego. Najlepsze odwzorowanie obiektu rzeczywistego na model uzyskuje się wówczas, gdy sítu jest traktowane jako układ ciągły. Rozważany przypadek jest tego przykładem. Pokazuje przy tym, że nieprawidłowo dobrane cechy konstrukcyjne znaczaco pogorszają właściwości eksploatacyjne urządzenia. Ruch roboczy sita wymuszają jeden lub dwa wzbudniki bezwładnościowe. Powinny one posiadać właściwość samosynchronizacji. Efekt ten nie zawsze jest osiągany, co powoduje, że kierunki drgań sita nie są zgodne z kierunkami obciążen przenoszonych przez wibroizolatory. Częstotliwości drgań wymuszonych mogą być wówczas zbliżone do częstotliwości drgań własnych dla określonej postaci modalnej i układ pracuje w warunkach rezonansu.

Słowa kluczowe: drgania własne, częstotliwości rezonansowe, samosynchronizacja wzbudzenia

1. WSTĘP

Vibrating screens are machines used in many industries, particularly in the mining industry, agricultural and food processing industry as well as the construction materials industry. The working motion of a vibrating screen is vibration of its main structural element, i.e. the sieve, imposes many strength-related requirements on the entire machine. The design of the sieve should be compact and resistant to high loads varying with time. Optimisation of functional properties of the vibrating screen comes down to achieving correct proportions between its overall dimensions and inertia, which limits the power of the machine driving mechanisms. The sieve is driven by exciters consisting of unbalanced discs mounted on the motor shaft and being the source of centrifugal force which enforces oscillations of the sieve. The vibrating isolators which limit the magnitude of force transmitted to the supporting structure and simultaneously ensure correct conditions if screening process, constitute important elements of

the sieve foundation. To achieve suitable output of the machine, the velocity of sieve vibration must be properly adjusted to the type of the screened material allowing smooth flow of it through the sieve.

The most commonly used vibration isolators are spring systems. Cylindrical springs are used in machines where the sieve vibrates mainly in vertical direction. Suspension of the sieve on flat springs allows for its axial movements. The vibration isolators with elastic inserts and three axes of relative movement of the moving elements allows the sieve to move in two directions and therefore to obtain better screening characteristics. The vibrating screen supporting structure should be stiff and stable in order to obtain conditions in which the dynamics of the machine is determined only by the excitation-vibrating isolation-sieve inertia system, since it should be remembered that vibrating screens are large machines and their sieves are sometimes mounted at significantly high level. Free vibration of the sieve founded on vibrating isolators with low stiffness along the

working direction are characterised by low frequencies and the forcing frequencies reach the values of a dozen Hz; in this way the design engineers are striving to eliminate resonance in the system at the working speed of the machine. However, the sieve is not a stiff body and also has its own free vibrating frequencies, usually quite high. In turn, the vibration isolators feature high stiffness along the direction other than the working direction of the sieve. As a result, beyond the free vibration frequencies falling within the low-frequency range, the vibrating screen may also perform free vibrations with higher frequencies, close to the forcing frequency. Then the resonance phenomenon occurs along the direction other than the direction in which the vibrating screen works; and this resonance has an adverse effect on both the strength of machine elements and the dynamic characteristics of the screening process.

In the past, many scientists were interested in conducting research concerning vibrating screens. In Poland, these issues were widely studied at the AGH University of Science and Technology [1-3]. The studies were conducted with relation to the nature of vibration of industrial machines and creation of their numerical models. In modern over-resonance screens the phenomenon of self-synchronisation of inertial vibrators is employed. However, it was found that in case of improper self-synchronisation the phase shift between discs imbalance vectors occurs, leading to differentiation of vibration parameters in various points of the screen structure. The results of spring-supported vibrating screens operation analysis prove that in case of short-term interactions appearing during transition of the system through a resonance zone the magnitude of dynamic interactions is several times higher than during stabilized movement. For stability of sieve movement the random-type interactions occurring in the vibrators' drives and suspension systems are significant [4].

2. NUMERICAL ANALYSIS OF THE DYNAMICS OF A VIBRATING SCREEN SIEVE

In the agricultural products processing industry a vibrating screen manufactured by a Spanish company, Urtasun, is employed. Its design is shown on Fig.1. The main component of the screen is the sieve with the mass of about 3500 kg. Two inertial vibrators are fixed to a transverse beam located in the upper part of the sieve at an angle of 45° with respect to the horizontal plane. Since the original solution of sieve foundation was not adapted to the value of the oscillation exciting force necessary for achieving suitable efficiency of the screening process and therefore breakages and fractures in both the sieve and supporting elements have occurred, it was necessary to redesign the

foundation in order to meet the requirements relating to its strength and stability (Fig.1). The columns which were originally made of closed stiffened profiles were replaced with posts made of thick-wall tubes and instead of resting directly on the floor the screen was positioned on specially built foundation made of steel-reinforced concrete. As a result, the structure vibration velocity was reduced from several dozen down to just a few mm s^{-1} [5].



Fig.1. The vibrating screen after modernisation.

1. Sieve;
2. Exciters;
3. Supporting structure;
4. Belt conveyors;
5. Foundation

The sieve of the vibrating screen rests on vibration isolators produced by a spanish company, ROSTA (Fig.2). These isolators have plastic inserts which play a role of elastic and damping elements and are selected depending on the weight of the oscillating mass. Low stiffness of the insert ensures low frequency of sieve free vibrations in 0y and 0x directions. This vibration isolator features low flexibility along the 0z direction, i.e. the direction perpendicular to its plane of deflection ($x0y$ plane). Thus, the frequency of free vibrations in this direction is high.

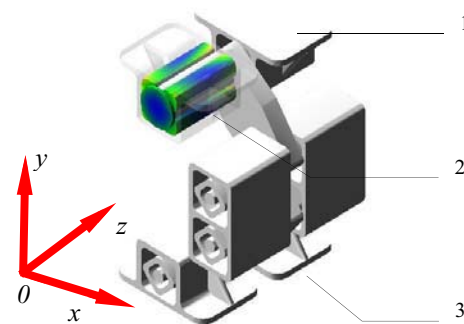


Fig.2. Vibration isolator with elastic insert.

1. Upper arm,
2. Elastic inserts,
3. Lower arm

Usually, the manufacturer declares the stiffness and damping characteristics of the vibration isolator. However, it applies only to these directions along which the isolator's deflections are expected. Other parameters should be determined either

experimentally or based on the analysis of the device model vibrations by comparing the measured values of free vibration frequencies with those obtained from the response analysis of a numerically simulated system.

Although simulation of a vibrating isolator with elastic inserts made of plastic material with high deformability turned out to be a quite complicated issue, the results obtained were very coincident with the results of examinations. The complexity of the problem was that the interactions between the inserts and surfaces of sockets are of contact character. To create a correct representation of the contact it is necessary to know the parameters of physical phenomena occurring within the zone of mutual contacts of the elements. The assumed stiffness of inserts corresponds to the actual values because the calculated static characteristic curve for the model of the vibrating isolator is close to such curve determined during examinations. The difference is that the calculated stiffness/deflection curve is almost linear for deflections within the range of up to 10 mm, while in this range the actual curve shows the change in vibrating isolator stiffness of more than 100 N mm^{-1} . Of course, the flatter the vibrating isolator stiffness characteristic curve is, the easier the selection of the vibrating isolator is.

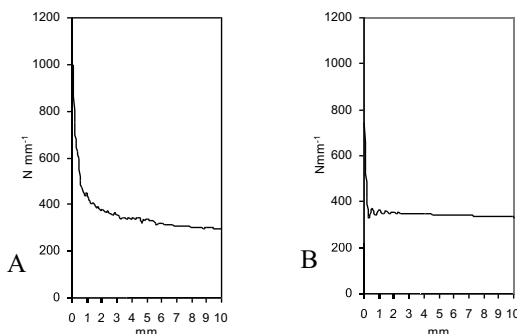


Fig.3. The stiffness / deformation characteristic curve of a vibrating isolator determined: (A) experimentally, (B) based on a numerical model

The model of inertial exciter produced by the ROSTA Company is shown in Fig.4A. On each end of the motor shaft an asymmetrical disc is fixed. By changing the angular displacement between these two discs it is possible to adjust the value of centrifugal force within the range of up to 64 kN. In the original design developed by the vibrating screen manufacturer the exciters are placed at an angle of 45° relative to the material feed plane. At first glance such arrangement of exciters may be surprising, since if the rotation of unbalance vectors for both discs is not synchronised, the centrifugal force can excite oscillations of the sieve in the direction perpendicular to its axis. As it was indicated above, vibrations in this direction are not suppressed by the vibration isolator. The movement

trajectory of the sieve gravity centre should have the form of an ellipse and in special cases – a circle lying in the vertical plane rather than the form of a three-dimensional curve. After approximately three seconds the exciter reaches the maximum rotational speed of almost 1000 rpm. The rise of force caused by unbalance of discs with time is illustrated in Fig.4B.

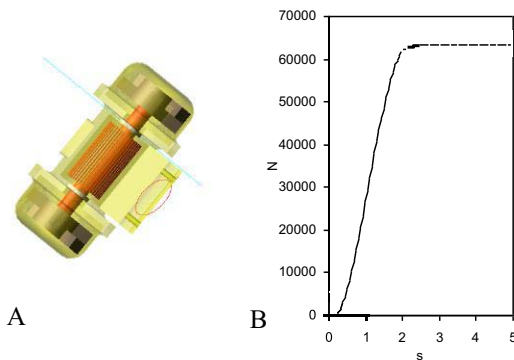


Fig.4. Numerical model (A) and the run-up time/force characteristic (B) of inertial exciter

In the arrangement of exciters as shown in Fig. 5 the projections of forces caused by disc unbalance on the straight line orthogonal to the vertical plane going through the sieve axis will not compensate in case of different values of resistance to the motion of their rotors. This is disadvantageous in the aspect of the vibrating isolators' design, particularly in cases where resonance oscillations occur in this direction. Such problem appeared in the vibrating screen being examined. The velocity of vibration in forbidden direction at the forcing frequency of 16.5 Hz reached the value of almost 100 mm s^{-1} .

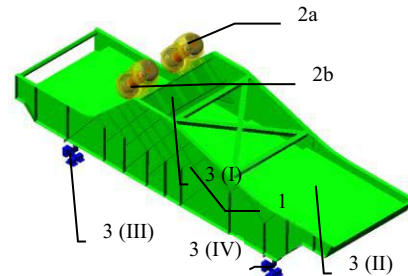


Fig.5. The model of vibrating screen simplified to the system of vibrating mass – elastic and suppressing elements – excitation.

1. Sieve
2. Exciters
3. Load bearing columns
4. Foundation

To identify the reasons for rough running of the sieve it was necessary to perform detailed examinations. It was assumed that in order to take special countermeasures aimed at limiting the vibration amplitudes in a reasonable way, the numerical analysis of the system model should be performed first. The numerical model of the

vibrating sieve, including its main components, is shown in Fig. 5.

The presented method of vibrating screen modelling based on the dynamics of multi-body systems is a development of the method employed in the paper [6], where the solution of sieve motion equations derived on the ground of the calculus of variations was presented.

3. EXAMINATIONS OF THE SIEVE VIBRATION CHARACTER

The sieve dynamics was examined on the basis of modal analysis. Since the system vibrations were originally supposed to be over-resonant, the system response characteristics can be determined using a short-term Fourier transform of velocity vs. time waveforms of vibrations excited by the force generated by unbalance of vibrators' discs during run-up and run-down phases. Examinations were carried out during simultaneous operation of both exciters and during individual operation of each exciter independently.

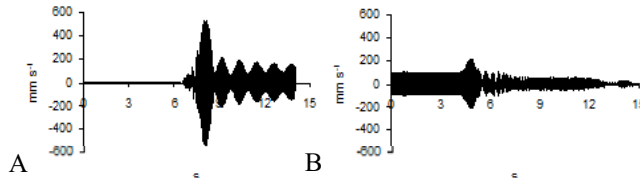


Fig.6. Velocity vs. time waveforms for sieve vibration in $0z$ direction during run-up (A) and run-down (B) phases with both exciters active

During operation of two exciters the velocity vs. time waveforms for sieve oscillations along the $0z$ direction during run-up and run-down phases are presented in Fig. 6A and Fig. 6B. In each case the dynamics of the system is different. During the run-up phase the transition through resonance zone at higher angular frequencies occurs with higher vibration velocity amplitudes than during the run-down phase. It occurs near the frequency of 16 Hz (see Fig. 6B). The resonance zone at low frequencies is better visible during the sieve run-down period. The sieve run-up is accompanied by a beat phenomenon caused by the fact that during the run-up phase the rotational speeds of exciters are slightly different.

In the image of short-time Fourier transform of vibration velocity (Fig.7) the area of resonance vibrations occurrence within the range of 15.5 Hz–16 Hz (Fig.7) is clearly visible. Also, the effect connected with differing resistance to motion of exciters can be noted. The vibrator marked with the symbol 2a in Fig.5 features higher resistance to motion; therefore the time to stop for this exciter is shorter than for the 2b exciter.

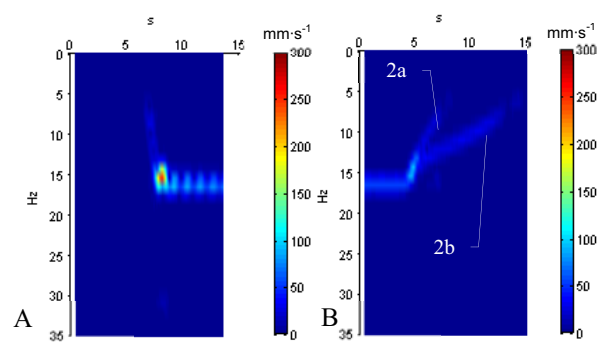


Fig. 7. Image of short-time Fourier transform of time waveforms of sieve vibration velocity during the run-up (A) and run-down (B) phases of the system with two exciters in operation

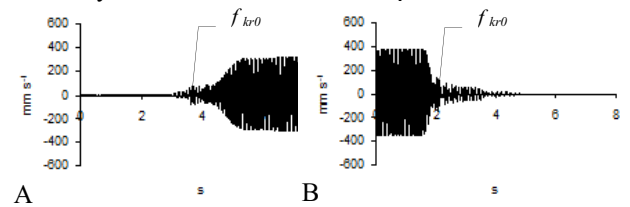


Fig.8. Velocity vs. time waveforms for sieve vibration in $0z$ direction during the run-up (A) and run-down down (B) phases with exciter 2a in operation

If only exciter 2a is in operation the beat effect does not occur (Fig.8). The amplitudes of sieve vibration velocity are much higher than during simultaneous operation of both exciters. This is understandable, since the angular velocities of exciters have opposite senses and $0z$ components of forces generated by disc unbalance should mutually compensate. When only one exciter is in operation, such condition cannot occur.

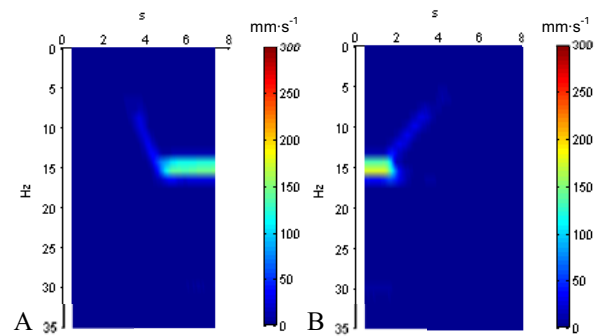


Fig.9. Image of short-time Fourier transform of time waveforms of sieve vibration velocity during the run-up (A) and run-down (B) phases of the system with exciter 2a in operation

In such circumstances the amplitude of sieve vibration is very high but as a result of intense damping in the system the resonance does not occur because the rotational frequency of the exciter is lower than free vibration frequency of the sieve (Fig.9).

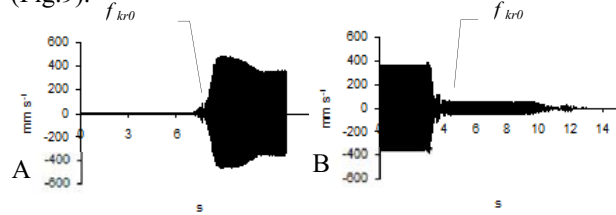


Fig.10. Velocity vs. time waveforms for sieve vibration in $0z$ direction during the run-up (A) and run-down down (B) phases with exciter 2b in operation

Driving the sieve using only exciter 2b leads to very high amplitude values of its vibration velocity (Fig.10). The occurrence of resonance vibration is clearly visible, particularly during the sieve run-up phase.

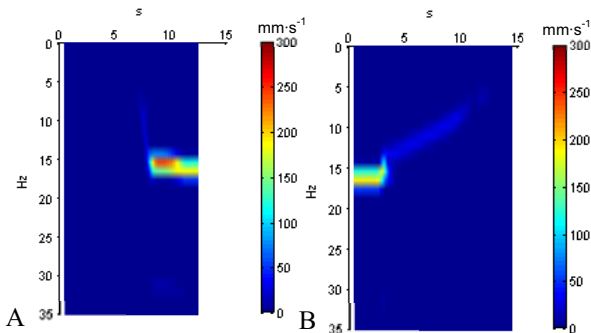


Fig.11. Image of short-time Fourier transform of time waveforms of sieve vibration velocity during the run-up (A) and run-down (B) phases of the system with exciter 2b in operation

The smooth increase of vibration velocity amplitude during the sieve run-up phase confirms the presence of high damping in the system along the $0z$ direction (Fig.11).

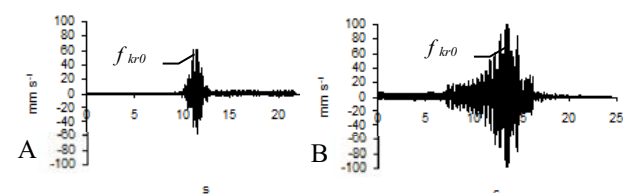


Fig.12. Velocity vs. time waveforms for sieve vibration in $0z$ direction during the sieve run-up (A) and run-down down (B) phases with both exciters running, for the excitation frequency of 13.5 Hz

The amplitude of sieve vibration velocity in forbidden direction can be effectively reduced by pulling the system out of resonance. To this end,

using the frequency converters, the angular velocities of exciters were reduced down to the value of about 85 s^{-1} , with simultaneous increase of the exciters' disc unbalance to the maximum value at which the centrifugal force has the absolute value of 64 kN.

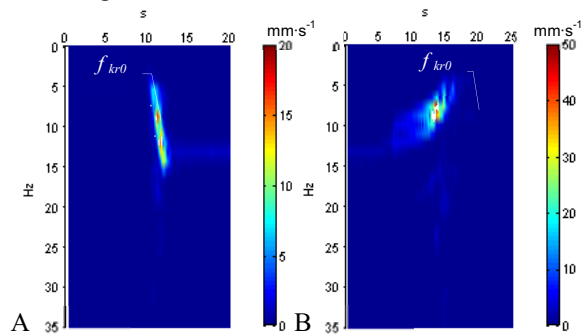


Fig.13. Image of short-time Fourier transform of time waveforms of sieve vibration velocity during the run-up (A) and run-down (B) phases with both exciters in operation, for the excitation frequency of 13.5 Hz

As a result of forcing frequency reduction, after passing through the critical frequency f_{kr0} the amplitude of vibration velocity was reduced to a few mm·s⁻¹ (Fig.12-13). Since the amplitudes of vibration velocity in the directions $0y$ and $0x$ reach the values of almost 160 mm·s⁻¹, the screen operates smoothly with assumed output (Fig.14).

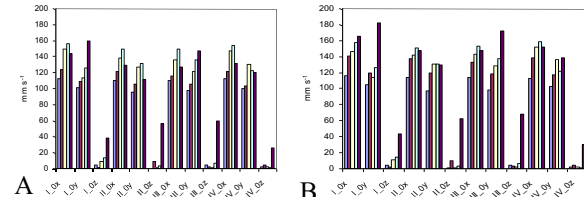


Fig.14. Values of amplitudes (A) and RMS (B) of sieve vibration velocity in directions $0x$, $0y$, $0z$ at excitation frequencies of 10 Hz, 11.5 Hz, 12.5 Hz, 13.25 Hz and 16.5 Hz, respectively

At excitation frequency of 16.5 Hz the level of sieve vibration in the $0z$ direction increases abruptly. The Roman numerals I, II, III, IV on Fig. 14 indicate the numbers of vibrating isolators in the system presented on Fig.5.

4. MODELLING SIEVE VIBRATIONS AND SCREENING PROCESS

The analysis of sieve vibration using the dynamics of multi-body systems allows considering the screen as a stiff body supported by elastic-damping elements. The mass of 3500 kg was assigned to the body simulating the sieve. The values of the stiffness of vibrating isolators determined by numerical modeling were verified experimentally. The vibrators attached to the sieve model were considered to be a set of stiff bodies linked by appropriate constraints. It was assumed that the

vibrators operate in self-synchronisation conditions and the vectors of angular velocities of rotors have opposite senses. The force generated by the disc unbalance was established at the maximum level possible for ROSTA vibrators, i.e. at the level of 2×64 kN at rotational frequency of 16.6 s^{-1} .

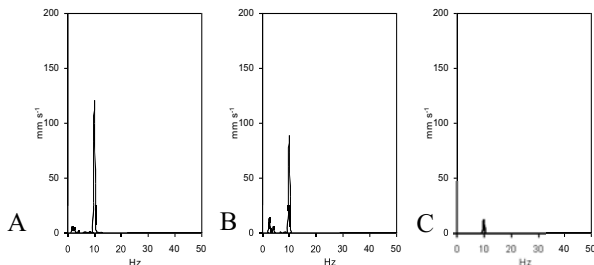


Fig.15. Amplitude-frequency characteristic curves obtained on the basis of vibration velocity vs. time waveforms for the frequency of 10 Hz in the directions: (A) - $0x$, (B) - $0y$, (C) - $0z$

Fig.15 shows the amplitude-frequency characteristic curves of sieve vibration velocity, determined on the basis of numerical calculations of time waveform for excitation frequency of 10 Hz. The vibration velocity amplitudes at this frequency are close to the measured values presented in Fig.14A as the first left stripe in each bar. The amplitudes of vibration velocity in $0z$ direction for the frequency of 16 Hz are lower than the actual values. This means that the assumed value of damping is lower than the value of damping which actually exists in the system.

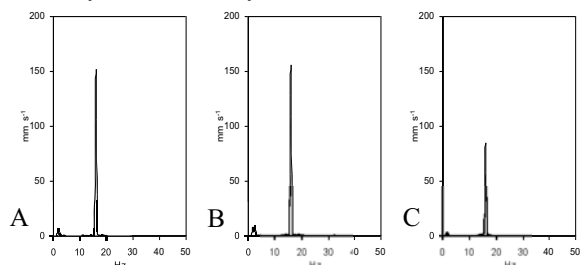


Fig.16. Amplitude-frequency characteristic curves obtained on the basis of vibration velocity vs. time waveforms for the frequency of 16 Hz in the directions: (A) - $0x$, (B) - $0y$, (C) - $0z$

By comparing the sieve vibration velocity determined for a given forcing frequency with values of vibration velocity amplitudes obtained from numerical calculations it is possible to evaluate the conformity of physical properties of the model with the real object. As these values do not differ significantly, it can be stated that such compliance is satisfactory.

When considering the potential for reduction of sieve excitation frequency it is important to take into account the possible change in screening process efficiency, because this efficiency should not be less than the assumed one. Otherwise, the machine would

be a weak link in the technological process. The best way to learn about the extent of the possible change in the efficiency is to simulate the screening process for various sieve excitation frequencies; however, it is an issue to simulate the loose feed material. In the majority of studies two approaches to this issue are employed – the first is to simulate the feed material as a set of particles [7] and the other is to simulate it as layers [8].

The simulation method applied here can be described as a simplified particle-like approach. The course of the screening process and its efficiency was analysed on the basis of the speed of transporting the body with the mass of 45 g along the screen. The mass of 45 g was assumed to be the value corresponding to the average mass of a vegetable being screened. Thus, the interactions between particles of feed material are neglected while the relations between the particle and the sieve are the focus of attention.

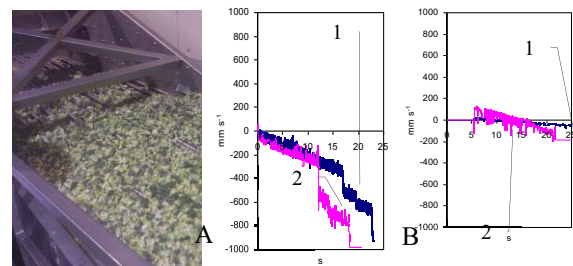


Fig.17. Variations in the feeding speed of the screened material in the $0x$ (A) and $0z$ (B) directions for excitation frequency of 10 Hz (1) and 13 Hz (2)

It can be noted that at the sieve vibration frequency of 10 Hz the movement of raw material is smoother than at the frequency of 13 Hz. The velocity fluctuations in the direction perpendicular to the sieve axis are smaller (Fig.17B), similarly as for material feed velocity along the sieve axis. In consequence, the efficiency of the screening process is also worse.

The sieve is a thin-walled structure. From the point of view of its strength the value of stress in cross-sections of steel plates forming the sieve frame is important. In the examined structure many material discontinuities were present, particularly near the joints. It can be assumed that it was the effect of both resonance vibrations in the $0z$ direction at the exciters' rotational frequency of 16.5 Hz and asynchronous operation of exciters.

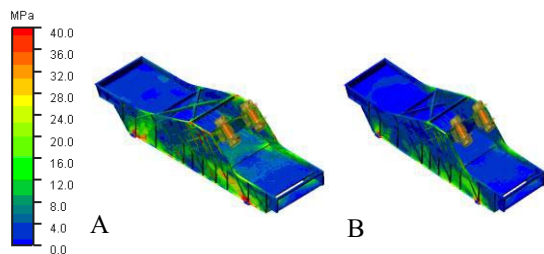


Fig. 18. Stress maps in sieve framework plates at excitation with the frequency of 10 Hz for asynchronous (A) and synchronous (B) operation of exciters

As it can be seen from stress map shown in Fig.18, in extreme asynchronous state, i.e. when only one exciter is operating, the reduced stresses in some areas of the sieve structure exceed the value of 40 MPa, while during synchronous operation such level of stresses occurs only in points of fixing the vibrating isolators to the sieve frame. It is understandable that with the increase of excitation frequency the values of stress will rise. With the stress cycle varying with time the above can lead to damage of the sieve structure.

5. CONCLUSIONS

Oscillations of numerous machines founded on vibration isolators can be analysed by considering these machines as vibrating systems composed of stiff bodies supported with elastic-damping elements featuring specified stiffness and damping values. Usually, the free vibrations frequency of the structure is sufficiently high to avoid excitation of such vibrations by the moving elements of the machine. The properly selected disc-type vibration isolator has the ability of damping vibrations in many directions. For vibrating screens, where for proper operation of the sieve its gravity centre should draw an ellipse or circle in vertical plane, the specially designed vibrating isolators are used which allow for substantial displacements of the element founded on them. The product of the ROSTA Company is one of examples of such vibration isolators. It features low stiffness in the plane parallel to the plane of gravity centre trajectory and high stiffness in the direction perpendicular to this plane. In consequence, the sieve free vibration frequency in the direction of high stiffness of a support is also high.

Operation in conditions of free vibrations adversely affects both the strength of sieve's structural elements and the efficiency of screening process. The system can be pulled out of resonance by attaching additional mass to it. However, such countermeasure is of limited effectiveness, since attaching mass as high as 500 kg does not lead to noticeable reduction of free vibration of a sieve, as it was confirmed during examination of the machine during its operation. In the case being considered it was observed that asynchronous operation of exciters

is also a source of high-amplitude vibrations of the sieve. The sieve driving mechanism was designed so that the exciters' discs with the same unbalance should rotate in opposite directions synchronically, starting from the lowest position of the gravity centre. The exciters may operate synchronically provided that the values of resistance to motion of their rotors are identical. As it is practically impossible, the vectors of the disc unbalance in the Oz direction do not mutually compensate. At the excitation frequency close to the free vibration frequency very high amplitudes of vibration occur. Upon reduction of the excitation frequency, this phenomenon is limited.

Numerical simulations lead to the conclusion that an increase in the excitation frequency causes an increase of material travel speed but also enhances the effect of feed material fluctuation in the direction perpendicular to the sieve axis, which obstructs the movement of material being fed. Therefore, with free vibrations in the direction perpendicular to the sieve axis the efficiency of the screening process is limited and also the value of stress in the sieve frame cross-sections increases. However, the main reason for sieve frame breakages and fractures is damage of one of the exciters. Such damage has occurred several times during operation of the vibrating screen, causing damage of the sieve frame in many points and therefore, reduction of its stiffness. In consequence, the free vibration frequency of the sieve decreased near the excitation frequency and the system returned to work in resonance conditions again. Only when the excitation frequency was significantly reduced, the amplitude of the sieve vibration velocity was lowered.

Self-synchronisation of exciters may occur only when the values of their rotors' resistance to motion are identical. However, practice shows that this is very difficult to achieve. As a satisfactory solution for the concurrency of the exciters forced synchronisation can be considered. To this end, the frequency converters used in exciters' drives should be equipped with a controller for the process of equalizing the phase angle between rotating vector of the disc unbalance. The system for continuous measurement of relative angular displacement between the unbalance vectors must be equipped with phase markers. When the measurement of this angle shows that it is not equal to zero, the follow-up system commands the converter which drives the exciter with lower rotational speed to increase this speed until the angular difference between the disc unbalance vectors is eliminated.

REFERENCES

- [1] Banaszewski T., Filipowicz A., *Badania poprawności drgań przesiewaczy*, Maszyny Górnictwa, 20, 2, 2002s. 29-34,

- [2] Banaszewski T., Filipowicz A., *Oddziaływanie dynamiczne przesiewaczy nadrezonansowych na konstrukcję wsporczą*, Maszyny Górnictwa, 22, 2, 2004, s. 29-34,
- [3] Banaszewski T., *Wpływ położenia samocentrujących się wibroizolatorów na drgania przesiewacza*, Zeszyty Naukowe Politechniki Śląskiej, Górnictwo, 245, 2000, s. 17-26,
- [4] Zabawa M., *Zjawiska losowe w wybranych typach maszyn wibracyjnych*, Zeszyty Naukowe Akademii Górniczo-Hutniczej, Mechanika, 22, 2, 2003, s. 189-201,
- [5] Zachwieja J., *Application of numerical analysis in dynamic state diagnosis of the machine with a shok charakter of operation*, Diagnostyka, 63, 2012, pp. 63-68,
- [6] Michalczyk J., Cieplok G., *Model cyfrowy przesiewacza wibracyjnego*, Modelowanie Inżynierskie, 32, 2006, s. 381-388,
- [7] Blackmore D., Samulyak R. Rosato A., *New mathematical model for particle flow dynamics*, Journal of Nonlinear Mathematical Physics, 6, 2, 1999,
- [8] Sokołowska R., *Modelowanie i analiza dynamiczna pojemnikowych maszyn wibracyjnych UW do obróbki powierzchniowej*, Zeszyty Naukowe Politechniki Rzeszowskiej, 174, 52, 1999.

Dr hab. inż. **Janusz ZACHWIEJA** is the Professor in the Department of Applied Mechanics at the University of Technology and Life Sciences in Bydgoszcz (Poland). His scientific interests include dynamics of mechanical systems and fluid mechanics.



QUANTIFIABLE MEASURES OF THE STRUCTURAL DEGRADATION OF CONSTRUCTION MATERIALS

Henryk KAŽMIERCZAK, Tadeusz PAWŁOWSKI, Łukasz WOJNIŁOWICZ

Industrial Institute of Agricultural Engineering
ul. Starołęcka 31, 60-963 Poznań, Poland
e-mail: kazmhenr@pimr.poznan.pl

Summary

The authors have outlined a method for analysing the fatigue degradation of mechanical structures described in terms of variations in the mobility of dynamic impedances, their real and imaginary parts and fluctuations in the strength of dynamic rigidity and the strength of the internal damping of structures expressed as a function of degradation time (the number of degrading impulse impacts). The variations are identified over the full scope of destruction ranging from nucleation to dominant fracturing. Such an identification is carried out by the method of experimental modal analysis and by energy-based methods with the use of a mechatronic accelerated testing station. The paper provides definitions of the related measurable measures of the process[6]. The point is illustrated with an overview of selected strength characteristics of modern construction steel.

Keywords: structural changes, dynamic mobility, impedance, mode, work of damping forces

MIERZALNE MIARY PROCESU DEGRADACJI STRUKTURALNEJ MATERIAŁÓW KONSTRUKCYJNYCH

Streszczenie

Przedstawiono zarys metody analizy procesu degradacji zmęczeniowej struktur mechanicznych, opisanej przez charakterystyki zmian mobilności dynamicznych, impedancji, ich części rzeczywistych i części urojonych oraz zmian mocy sił sztywności dynamicznych i mocy sił tłumienia wewnętrznego struktur w funkcji czasu procesu degradacji (liczba degradujących uderzeń impulsowych). Charakterystyki te wyznacza się w pełnym zakresie procesu niszczenia od nukleacji do dominującego pęknięcia metodą eksperymentalnej analizy modalnej i metodami energetycznymi z zastosowaniem mechatronicznego stanowiska badań przyspieszonych. Praca zawiera definicje mierzalnych miar procesu. Jako przykład zamieszczono wybrane charakterystyki właściwości wytrzymałościowych nowoczesnych stali konstrukcyjnych.

Słowa kluczowe: zmiany strukturalne, mobilność dynamiczna, impedancja, mod, praca sił tłumienia

1. INTRODUCTION

The knowledge of fatigue strength is essential in many areas of structural design, particularly where key machinery comes into the picture. Mechanical structures are damaged wherever external impact alters structural properties while the continuous accumulation of energy elevates it beyond border values causing the destruction of a pivotal structural item[19]. To reflect the nature of such processes, degradation of mechanical structures has been described in terms of energy parameters.

Degradation processes in materials and building structures have an energetic dimension [8]. Changes in the parameters of structural materials will be described by an analysis of non-stationary profiles (shown as a function of degradation time) of power spectral density of damping forces (internal friction)

and, separately, power spectral density of dynamic rigidity forces as well as the work of forces causing degradation determined on that basis. The destruction of node sets in a mechanical system is described by a holistic energy model of loads[15].

2. THE CONCEPT BEHIND THE MODEL OF MECHANICAL STRUCTURE DEGRADA- TION

A holistic model of the load shifts which occur in the course of the degradation of a mechanical system can be described as a matrix of the spectral densities of dynamic loads [10, 3].

$$\{G_{N_k}(j\omega, \Theta)\} = H_{V_k}(j\omega, \Theta) \cdot G_{F_k F_k}(j\omega, \Theta), \quad (1)$$

where: H_{V_k} – dynamic mobility matrix,

\mathbf{G}_{FF} – external forcing actions spectral density matrix,
 \mathbf{k} – application points of external forcing actions (components F_{kx} , F_{ky} , F_{kz})[1],
 i – points of discrete stress tensor model,
 $i = k_1, k_2 \dots k_n, \dots r$.

Dynamic mobility is determined by spectral densities with account taken of frequencies of the vibrations and the impacts of the forces which degrade the structure:

$$H_{V_k}(j\omega, \Theta) = \frac{G_{VF}(j\omega, \Theta)}{G_{FF}(j\omega, \Theta)}. \quad (2)$$

The dynamic resistance of a system which undergoes changes in the course of degradation is measured by mechanical impendence which in turn can be determined by the spectral densities of impact and response signals:

$$R_{V_k}(j\omega, \Theta) = \frac{G_{FF}(j\omega, \Theta)}{G_{VF}(j\omega, \Theta)}. \quad (3)$$

The structure of a sample (i.e. all of its internal features) changes during the degradation of a system (a machine component or a material sample) taking place over degradation time Θ [3].

Due to its holistic nature, the modelling of the destruction of structures entails describing their behaviour in terms of physical processes whose individual components of the matrix of the distribution of dynamic loads, which are a function of dynamic time t or frequency, are determined in the function of the long time Θ they take to succumb to degradation. The real components of such a load provide a measure of the internal dissipation which causes the structural degradation of a structure[11].

The work performed by external forcing impact equals changes in rigidity and the effects of the system's damping forces which in turn are a measure of its degradation. The value of the work performed is a function of the measures of vibration damping and amplitude. Such a value reaches its peak when brought into resonance.

The degradation capacity of a structure (material sample) equals the total work of structural degradation

$$L_{degr.} = \int_{\Theta_0}^{\Theta_r} \operatorname{Re} N_{kk}(\Theta) d\Theta + \frac{1}{2} \int_{\Theta_0}^{\Theta_r} \operatorname{Im} N_{ik}(\Theta) d\Theta. \quad (4)$$

The energy capacity of construction material is defined as the work of the degradation forces which exert an impact upon the sample (item) multiplied by its capacity v , i.e.:

$$P_m = \frac{1}{v} \left[\int_{\Theta_0}^{\Theta_r} \operatorname{Re} N_{kk}(\Theta) d\Theta + \frac{1}{2} \int_{\Theta_0}^{\Theta_r} \operatorname{Im} N_{ik}(\Theta) d\Theta \right]. \quad (5)$$

Changes in the dynamic state of a mechanical structure described by the energy characteristics of vibration loads provide a significant indication of the resulting alterations and changes occurring within its structure. By focusing on the imaginary and real components of the strengths of degradation forces seen as functions of frequency, changes (peak shifts) in such functions may be identified. Shifts in extreme values of the relevant characteristics and the occurrence of valleys (anti-resonants) in the energy characteristics of dynamic rigidities offer general insights into preliminary stresses found in the structure and suggest the degrees of degradation exerted upon a mechanical structure manifested as changes in dynamic rigidity. Changing vibration damping forces, which affect the dissipation of mechanical energy, determine the structural degradation of mechanical structures over the duration of this process. Changes in dynamic rigidities manifesting themselves with cracking reach their highest intensities predominantly in the final stages of the technical degradation of mechanical structures. An analysis of such changes allows one to define the border loads which initiate the structural degradation of mechanical structures (in the form of e.g. cracking)[2].

3. RESEARCH POSITION

The research position comprised mainly of an automated impact control unit, an electro-dynamic hammer, troughs for measuring impulse impact forces and vibration accelerations, a dual channel analyser, a computerized data transmission and retransmission system as well as a post-processor for calculating energy values and characteristics in multi-dimensional space.

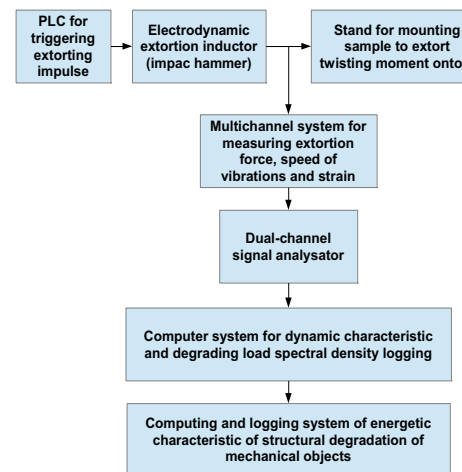


Fig. 1. Mechatronic system for determination of characteristic of structural degradation of mechanical objects[13]



Fig. 2. Photograph of a fatigue-fractured sample of construction steel

The authors carried out a comparative study of the fatigue strength of construction steel samples and laser weld joints of samples having the same dimensions. They determined the characteristics of the structural destruction of metal sheet samples cut with a water jet along and across rolling direction. Destruction to the point of fracture formation took several to over twenty hours – duration time was longer for solid samples and shorter for welded ones (Fig. 4 and 5).

4. DEGRADATION CHARACTERISTICS AND EXAMPLES

Relevant units of dynamic mobility \mathbf{H} (f, n) and their real (Re) as well as imaginary (Im) components, units of mechanical impendence \mathbf{R} (f, n) as well as their real and imaginary components and units of dynamic load as well as their real and imaginary components were marked on a vertical axis representing structural degradation characteristics. The horizontal axes of three-dimensional graphs were used to represent frequencies (in Hertz) and degradation time (in minutes). The minute scaling of the time axis was subsequently replaced with number n of the impulses brought to bear on each tested material sample.

When reviewing such characteristics, note the logarithmic or linear scales of amplitudes of individual physical parameters. Graphs of the spectral densities of real load power components describe the structural degradation resulting from changes in the internal structures of the tested materials (damping). On the other hand, the graphs showing the spectra of spectral densities of the imaginary components of degradation load powers describe changes in sample rigidity to cracking point. Load power graphs $N(t)$ are non-linear characteristics of sample degradation.

In analysing the graphs of spectral density spectra depicting parts of real loads and the structural degradation of individual samples, note should be taken of changes in the components of such spectra and the new induced components of the function of the number n of degrading impulses.

The documentation of study findings provides characteristics of various materials and samples and is helpful in drawing characteristic comparisons. A comparison has been offered of the selected characteristics of modules, real (Re) and imaginary (Im) components of dynamic mobilities, impendence

modules R , their real and imaginary components and changes in the strength of dynamic rigidity and damping forces shown as a function of process degradation time (the number of degrading impulse impacts) over the full range of destruction from nucleation to dominant fracturing.

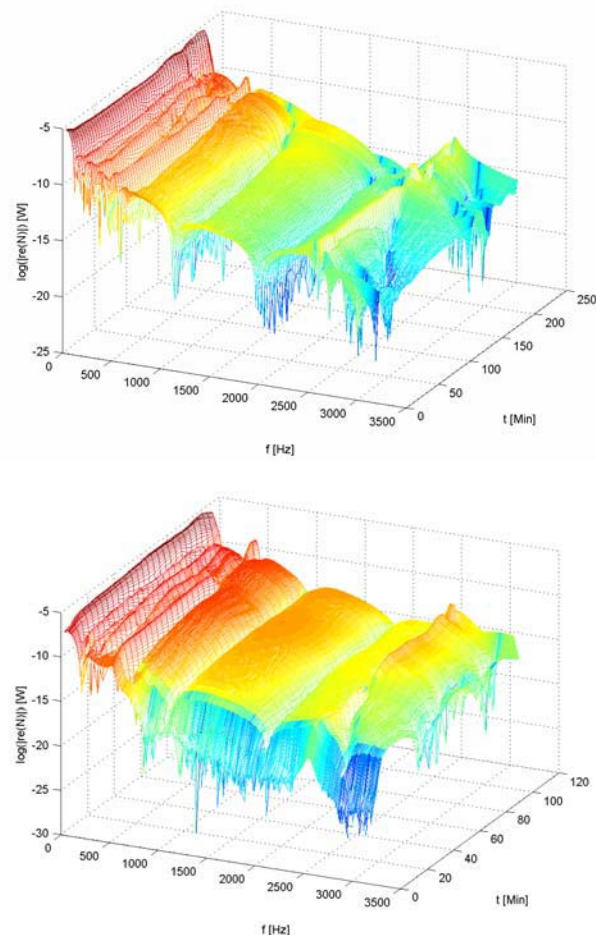


Fig. 3. Graphs representing the power of damping forces $\log ReN(f, t)$ as a function of steel sample degradation time following its electrical welding (figure below)

The number of impacts and the work of structural degradation forces vary from one construction material to another. Degradation characteristics are selected from a full set of characteristics of a wide range of samples. Such characteristics include specific information on changes in the structure at hand in its degradation process until fracture. A comparison and an analysis of the characteristics shown in the figures suggests specific conclusions.

The authors compiled the selected degradation characteristics for steel samples E and F without welding and with laser welds as well as an electrically-welded sample. Variations have been found in the modes of internal structure change force powers and the steel sample and electrically-welded sample degradation time (Fig. 3).

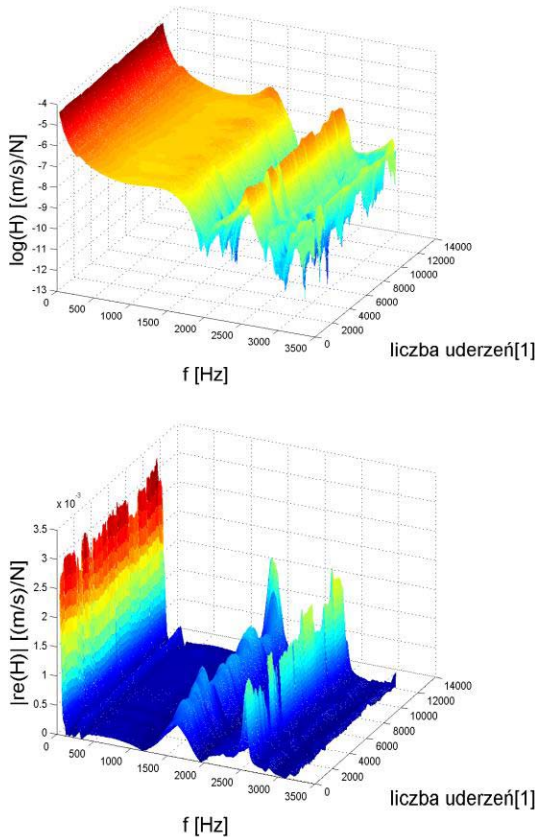


Fig. 4. Characteristics of structural degradation of welded steel sample E1

Changes in the amplitudes of dynamic mobility and impedance modes[12, 17] are essential (Fig. 3 to 5). The fact that the numbers of degrading load impulses and the changes in dynamic mobility and impedance mode amplitudes varied significantly has suggested substantial discrepancies in sample durability.

The characteristics include four intensive modes of the real part of dynamic resistance (Fig. 4 to 6). The energy characteristics of sample degradation take the form of rigidity $ImN(n)$ and damping force $ReN(n)$ graphs (Fig. 6).

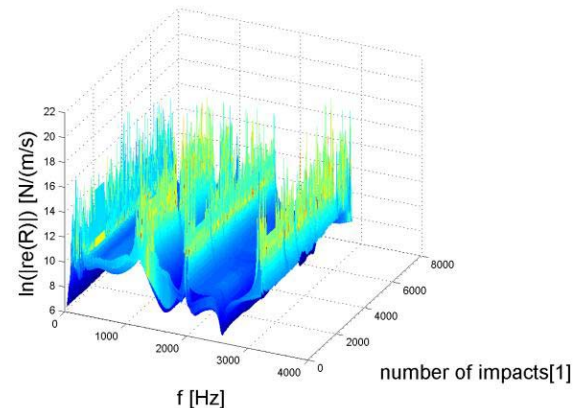
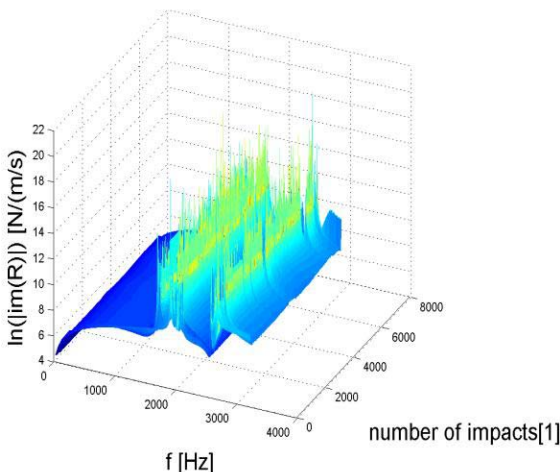


Fig. 5. Changes in mechanical impedances $ImR(f, n)$ and $ReR(f, n)$ during the degradation of steel sample F4

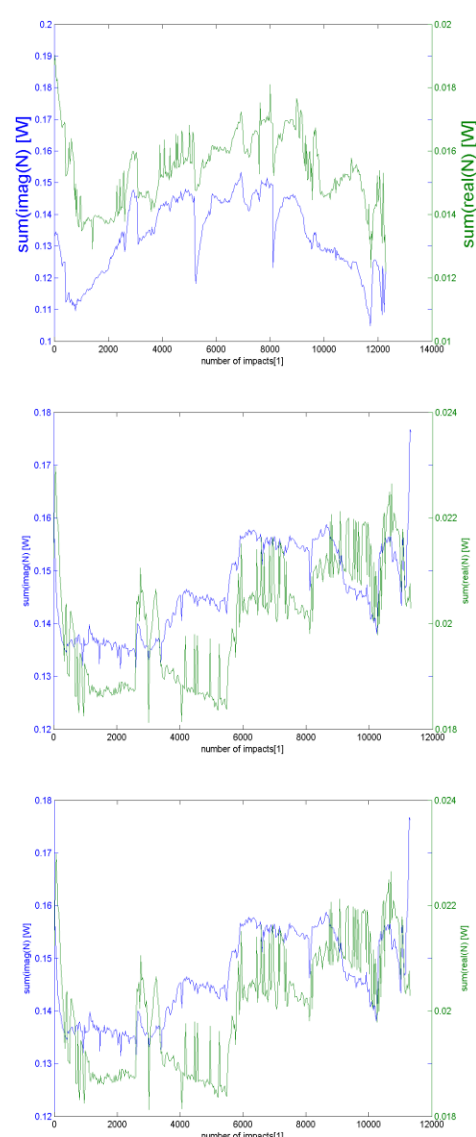


Fig. 6. Changes in the characteristics of rigidity forces $ImN(n)$ and damping force powers $ReN(n)$ causing the degradation of samples E8, F8, E3 (welded)

A symptom of structure degradation are changes in its dynamic properties manifesting themselves with variations in dynamic mobilities and mechanical impedances presented as a function of the number of degrading energy doses applied to the structure. Changes (declines and increases) in the frequency f of dynamic characteristic modes indicate alterations in the internal structure (damping) and the dynamic rigidities of structures (Fig. 7 through 8). A case in point is an increase in mode frequency, which is symptomatic of the strengthening of material structure.

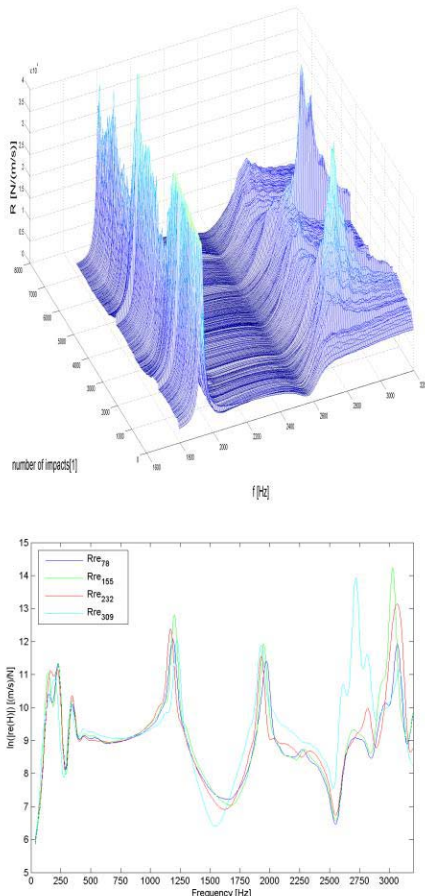


Fig. 7. Changes in impedance (dynamic resistance) $\text{ReR}(f)(\text{E}8)$

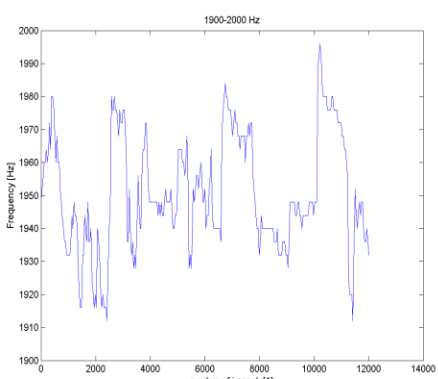


Fig. 8. Periodic changes in frequency f of impedance mode $\text{ReR}(n)(\text{E}8)$

The cumulative effects of loads which degrade a mechanical structure[9] are reflected in the curve of successive incremental growth in the work of structure degrading forces:

$$\Delta L(k) = \sum_k [L_k(dL)], \quad (6)$$

where: $k=0, 1, 2, \dots, n$ – successive region of degrading impacts,
 $L_k(dL)$ - work of degrading force performed after k impacts,
 dL – unit dose of the work of structure degrading forces.

The shape of curve $N_d(\Theta)$ indicates a trend in material sample degradation (Fig. 9).

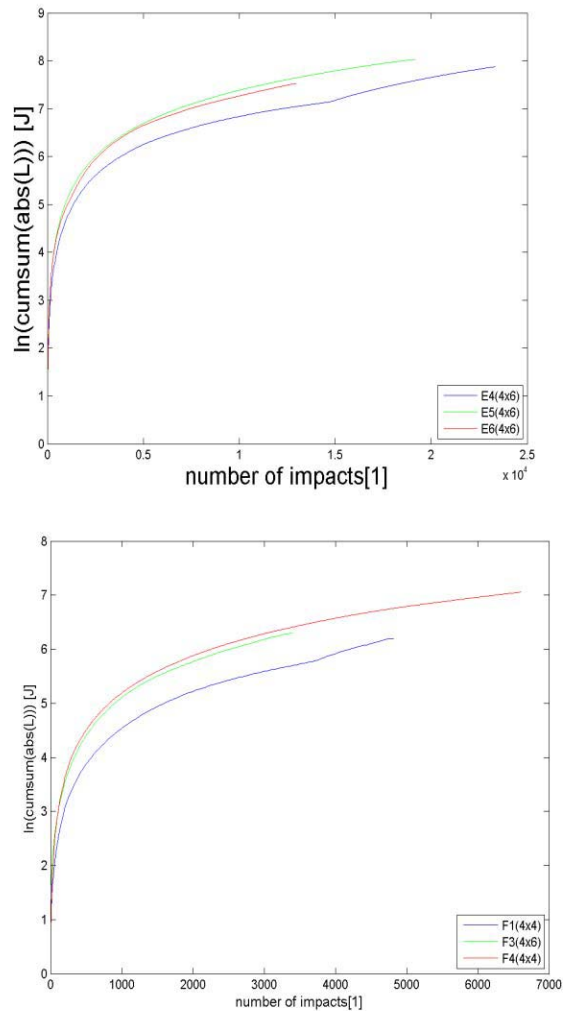


Fig. 9. Comparison of graphs showing the accumulation of forces which cause the structural degradation of steel samples (F1, F3, F4)

By integrating the energy degradation function $N(\Theta)$ (Fig. 6) while accounting for individual impulse powers, the authors determined the work of degradation forces L_d (the work of the rigidity force and the work of structural dissipation forces L_{dys}) as well as the unit work of degradation forces L_{di} and the unit work of structural dissipation forces L_{dysj} .

The energy **degradation capacity** of a material sample equals the total structural degradation work. The table shows energy characteristics of the structural degradation sustained by selected construction steel samples.

Energy calculations suggest that the durability of electrical welds is a function of welding parameters. In the case of laser welding, on the other hand, the fatigue strength parameters of steel E exceed those of steel F durability.

An important measure of fatigue durability is provided by the percentage share of the work of sampling forces (which is a measure of changes in the internal structure of a material) in the total work of degradation forces. Information on the energy values of the amplitude measures of fatigue durability has found its application in construction diagnostics and specifically in the design of machinery components which are reliable in terms of their durability. For the purposes of control diagnostics, use can be made of a methodology for studying the modes of dynamic characteristics which provide a measure of changes in the properties of mechanical structures undergoing technical degradation.

Table 1. Energetic parameters of construction steels durability

Energetic measures	Type of sample						
	5(wel. par.: 221A, 80cm/min)	9(wel. par.: 190A, 65cm/min)	15(wel. par.: 202A, 65cm/min)	E1(wel. laser) (4x6)	E3(wel. laser) (4x6)	E4 (4X6)	F4 (4X4)
L [J]	420	720	683	1580	1657	2634	1158
L _{in} [J]	416	715	678	1564	1646	2613	1155
L _{re} [J]	57	76	71	196	190	334	97
$\frac{L_{re}}{L} [\%]$	13,5	11	10	13	11,5	11,5	8,4
$\frac{L}{S} \left[\frac{J}{mm^2} \right]$	15			66	70	110	
$\frac{F}{S} \left[\frac{N}{mm^2} \right]$	29			38	38	38	44
$\frac{L}{V} \left[\frac{J}{mm^{-1}} \right]$							1,6

5. CONCLUSIONS

- Structural degradation characteristics can be broken down into the phases of nucleation, steady increases in non-elastic deformations, and the brief rapid rise of non-elastic deformations.
- Varying vibration damping, which is a factor in the diffusion of mechanical energy, is a measure of the structural degradation of a mechanical structure. Changes in dynamic rigidities, which manifest themselves with cracking, occur in the final phase of the technical degradation of a mechanical structure. An analysis of such changes facilitates the determination of border load values which trigger the structural degradation (e.g. cracking) of mechanical structure components.
- At the peaks of their dynamic mobilities, samples which reach the final stages of degradation undergo cracking. The fact that characteristic peaks shifted and that mode frequencies in energy characteristics declined (or increased) goes to confirm that the concerned mechanical structure has degraded.

- Similarities in spectrum shapes of real and imaginary parts, dynamic mobility modules and the spectra of loads impacting upon the mechanical systems in question, as well as changes in parameters such as a function of the number **n** of the applied impulses show that structural degradation depends on changes in dynamic properties, i.e. changes in the internal structure of materials leading to structure cracking.
- Changes in the internal structure and structural rigidities which represent modifications of the structure's dynamic resistance, contribute to unstable changes in process characteristics.

REFERENCES

- Akiniva Y., Stanzl-Tschegg S., Meyer H., Wakita M., Tanaka K., *Fatigue strength of spring steel under axial and torsional loading in the very high cycle regime*, International Journal of Fatigue, 30, 12, 2008, 2057-2063.
- Blicharski M., *Deformation and cracking*, ISBN 83-88408-53-4, Publishing AGH, Kraków 2002.
- Cempel C., Tabaszewski M., *Multidimensional Condition Monitoring of Machines in Nonstationary operation*, Mechanical Systems and Signal Processing, 21, 2007, 1233-1241
- Cempel C., *Generalized singular value decomposition in multidimensional condition monitoring of machines - A proposal of comparative diagnostics*, Mechanical Systems and Signal Processing, 23, 2009, pp.701-711
- Cempel C., *Innovative multilevel energy processor in machine condition monitoring*, Proceedings of International Conference on Quality, Reliability, Risk, Maintenance and Safety Engineering, Xi'an China, June 2011.
- Dietrich L., *The process and parameters of damage of structural materials*, IPPT PAN Warszawa 2003.
- Łagoda T., *Energetic models of fatigue life assessment for constructional materials under uniaxial and multiaxial random loads*. Studies and monographs, book 121, Opole University of Technology, Opole 2001.
- Olesiak Zb. S., Engel Zb.W., HUBER, ISBN 83-7204-557-7, *Institute for Sustainable Technologies-National Research Institute* Publishing House of the, Radom 2006.
- Yang L., Fatemi A., *Cumulative Fatigue Damage Mechanisms and Quantifying Parameters: A Literature Review*, J. Testing and Evaluation, 26, 2, 1998, 89-100.
- Kaźmierczak H., *Analysis of dynamic load power distribution in mechanical systems*. Publishing House of Poznań University of Technology, Poznań 2001, Studies 363.
- Kaźmierczak H., Pawłowski T., Kromulski J., *Energetic methods in machine diagnostics*, Diagnostyka, No 1(45)/2008.

- [12] Kaźmierczak H., Kromulski J., Pawłowski T., *Energetic modes in description of mechanical structures degradation, monograph "Selected issues of modal analysis of mechanical structures.* Collective work edited by Tadeusz Uhl, Department of Robotics and Machine Dynamics at University of Science and Technology, Kraków 2008.
- [13] Kaźmierczak H., Pawłowski T., Kromulski J., *Methods of describing structural degradation in constructional materials, Selected problems of modal analysis of mechanical systems,* ISBN 978-83-7204-832-5, Radom 2009.
- [14] Kaźmierczak H., Pawłowski T., *Energetic characteristics in description of structural degradation of constructional materials, Selected problems of modal analysis of mechanical systems,* ISBN 978-83-7204-983-4, Radom 2010.
- [15] Kaźmierczak H., Pawłowski T., Kromulski J., *Energetic modes in description of structural degradation of constructional materials, Diagnostyka, No 1(57)/2011.*
- [16] Martowicz A., Kurowski P., Uhl T., *Problems of determining the location of the measuring sensors for use in experimental modal analysis, Selected problems of modal analysis of mechanical systems,* ISBN 978-83-7789-074-5, Radom 2011.
- [17] Rosiek M., Martowicz A., Uhl T., *Electromechanical impedance based SHM system for aviation applications, Structural Health Monitoring,* Kraków 2012.
- [18] Zhong Zhang, G. Hartwig: *Relation of damping and fatigue damage of unidirectional fibre composites,* International Journal of Fatigue. 24, 2002, p. 713 – 718.
- [19] Żurek Z., H., Kukla D., Kurzydłowski K., J., *Wybrane metody wykrywania degradacji zmęczeniowej w stalach ferromagnetycznych.*



Dr hab.

Henryk KAŹMIERCZAK, prof. nadzw. – absolwent Wydziału Mat. Fiz. Chem. Uniwersytetu im. Adama Mickiewicza w Poznaniu, stopień doktora nauk technicznych uzyskał w 1977r. na Wydziale Budowy Maszyn Politechniki Poznańskiej. Stopień doktora habilitowanego nauk technicznych z dziedziny mechanika uzyskał w 2002r. na Wydziale Budowy Maszyn i Zarządzania Politechniki Poznańskiej. Jest autorem ponad 250 publikacji naukowych. Zajmuje się zagadnieniami z dziedziny dynamiki maszyn, diagnostyki technicznej, identyfikacji własności dynamicznych maszyn, w tym metodami analizy modalnej, energetycznym modelowaniem obciążeń

maszyn oraz zastosowaniami metody analizy rozkładu mocy obciążen dynamicznych do badań procesów degradacji strukturalnej i wyciążenia konstrukcji mechanicznych. Jest autorem energetycznych metod analizy degradacji struktur mechanicznych. Jest członkiem krajowych i zagranicznych towarzystw naukowych.



Dr inż.

Tadeusz PAWŁOWSKI – prof. nadzw., dyrektor Przemysłowego Instytutu Maszyn Rolniczych w Poznaniu. Absolwent Politechniki Poznańskiej, autor lub współautor ponad 100 prac naukowych z zakresu nowoczesnych metod analiz wytrzymałości konstrukcji,

symulacyjnego szacowania obciążen dynamicznych konstrukcji nośnych, analizy funkcjonalnej maszyn i urządzeń, komputerowego wspomagania projektowania (CAD) oraz projektowania napędów hydrostatycznych w maszynach rolniczych. Autor rozpraw pt. „Dynamika cienkościennych konstrukcji nośnych maszyn rolniczych z uwzględnieniem sił uogólnionych III rzędu”, „Studium transportu agregatów rolniczych w ujęciu teorii sterowania i bezpieczeństwa ruchu”.



Mgr. inż.

Łukasz WOJNIŁOWICZ – absolwent Politechniki Poznańskiej, Wydział Maszyn Roboczych i Transportu. Jest zatrudniony w Przemysłowym Instytucie Maszyn Rolniczych na stanowisku konstruktora. Zajmuje się: pomiarami wielkości mechanicznych metodami elektrycznymi, symulacją dynamiki maszyn oraz konstruowaniem postprocesorów w systemach obliczeń wytrzymałościowych.

**Lista recenzentów artykułów opublikowanych
w czasopiśmie Diagnostyka w 2013 roku**

dr hab. inż. Tomasz BARSZCZ, prof. AGH
prof. dr hab. inż. Wojciech BATKO
prof. dr hab. inż. Piotr BIELAWSKI
dr inż. Grzegorz BORUTA
dr inż. Tomasz BURATOWSKI
dr inż. Rafał BURDZIK
prof. dr hab. inż. Adam CHARCHALIS
prof. dr hab. inż. Wojciech CHOLEWA
dr inż. Witold CIOCH
prof. dr hab. inż. Tadeusz DĄBROWSKI
dr hab. inż. Andrzej DOBROWOLSKI
dr hab. inż. Jacek DYBAŁA, prof. PW
dr inż. Tomasz FIGLUS
prof. dr hab. inż. Jerzy GIRTLER
dr hab. inż. Paweł DROŹDZIEL, prof. PL
dr inż. Przemysław DROŻYNER
dr hab. inż. Andrzej GRZĄDZIELA, prof. AMW
dr inż. Adam JABŁOŃSKI
dr hab. inż. Piotr KANIEWSKI
prof. dr hab. inż. Yewhen KCHARCHENKO
dr inż. Grzegorz KLEKOT
dr inż. Łukasz KONIECZNY
dr inż. Tomasz KORBIEL
prof. dr hab. inż. Stanisław KULAS
dr hab. inż. Bogusław ŁAZARZ, prof. PŚ
dr inż. Jędrzej MĄCZAK
dr inż. Krzysztof MENDROK
dr inż. Janusz MIKOŁAJCZYK
prof. dr hab. inż. Stanisław OSOWSKI
dr hab. inż. Michał PAWŁOWSKI
dr hab. inż. Andrzej PIĘTAK, prof. UWM
prof. dr hab. inż. Stanisław RADKOWSKI
prof. Riccardo RUBINI
dr inż. Paweł RZUCIDŁO
dr hab. inż. Jacek STARZYŃSKI
prof. dr hab. inż. Henryk SUPRONOWICZ
dr inż. Krzysztof SZCZUROWSKI
dr inż. Michał ŚMIEJA
prof. dr hab. inż. Tadeusz UHL
dr inż. Jacek URBANEK
prof. Maria Cristina VALIGI
dr inż. Sławomir WIERZBICKI
prof. dr hab. inż. Andrzej WILK
dr inż. Mirosław WITOŚ
dr hab. inż. Grzegorz WOJNAR
dr hab. inż. Radosław ZIMROZ, prof. PWr
prof. dr hab. inż. Bogdan ŻÓŁTOWSKI

Diagnostyka

Obszar zainteresowania czasopisma to:

- ogólna teoria diagnostyki technicznej
- eksperymentalne badania diagnostyczne procesów i obiektów technicznych;
- modele analityczne, symptomowe, symulacyjne obiektów technicznych;
- algorytmy, metody i urządzenia diagnozowania, prognozowania i genezowania stanów obiektów technicznych;
- metody detekcji, lokalizacji i identyfikacji uszkodzeń obiektów technicznych;
- sztuczna inteligencja w diagnostyce: sieci neuronowe, systemy rozmyte, algorytmy genetyczne, systemy ekspertowe;
- diagnostyka energetyczna systemów technicznych;
- diagnostyka systemów mechatronicznych i antropotechnicznych;
- diagnostyka procesów przemysłowych;
- diagnostyczne systemy utrzymania ruchu maszyn;
- ekonomiczne aspekty zastosowania diagnostyki technicznej;
- analiza i przetwarzanie sygnałów.

Wszystkie opublikowane artykuły uzyskały pozytywne recenzje wykonane przez niezależnych recenzentów.

APPLIED STRUCTURAL HEALTH, USAGE AND CONDITION MONITORING

Topics discussed in the journal:

- General theory of the technical diagnostics,
- Experimental diagnostic research of processes, objects and systems,
- Analytical, symptom and simulation models of technical objects,
- Algorithms, methods and devices for diagnosing, prognosis and genesis of condition of technical objects,
- Methods for detection, localization and identification of damages of technical objects,
- Artificial intelligence in diagnostics, neural nets, fuzzy systems, genetic algorithms, expert systems,
- Power energy diagnostics of technical systems,
- Diagnostics of mechatronic and antropotechnic systems,
- Diagnostics of industrial processes,
- Diagnostic systems of machine maintenance,
- Economic aspects of technical diagnostics,
- Analysis and signal processing.

All the published papers were reviewed positively by the independent reviewers.

Redaktorzy działowi:

dr hab. inż. Tomasz BARSZCZ, prof. AGH
dr hab. Andrzej BIELECKI, prof. AGH
prof. dr hab. inż. Wojciech CHOLEWA
prof. dr hab. Wojciech MOCZULSKI
prof. dr hab. inż. Stanisław RADKOWSKI
prof. dr hab. inż. Wiesław TRĄMPCZYŃSKI
prof. dr hab. inż. Tadeusz UHL

Kopia wszystkich artykułów opublikowanych w tym numerze dostępna jest na stronie www.diagnostyka.net.pl

Druk:

Centrum Graficzne „GRYF”, ul. Pieniężnego 13/2, 10-003 Olsztyn, tel. / fax: 89-527-24-30

Oprawa:

Zakład Poligraficzny, UWM Olsztyn, ul. Heweliusza 3, 10-724 Olsztyn
tel. 89-523-45-06, fax: 89-523-47-37

Wszystkie opublikowane w czasopiśmie artykuły uzyskały pozytywne recenzje, wykonane przez niezależnych recenzentów.

Redakcja zastrzega sobie prawo korekty nadesłanych artykułów.

Kolejność umieszczenia prac w czasopiśmie zależy od terminu ich nadsyłania i otrzymania ostatecznej, pozytywnej recenzji.

Wytyczne do publikowania w DIAGNOSTYCE można znaleźć na stronie internetowej:
<http://www.diagnostyka.net.pl>

Redakcja informuje, że istnieje możliwość zamieszczania w DIAGNOSTYCE ogłoszeń i reklam.

Jednocześnie prosimy czytelników o nadsyłanie uwag i propozycji dotyczących formy i treści naszego czasopisma.

Zachęcamy również wszystkich do czynnego udziału w jego kształtowaniu poprzez nadsyłanie własnych opracowań związanych z problematyką diagnostyki technicznej. Zwracamy się z prośbą o nadsyłanie informacji o wydanych własnych pracach nt. diagnostyki technicznej oraz innych pracach wartych przeczytania, dostępnych zarówno w kraju jak i zagranicą.